Critical Currents in YBaCuO Thin Films

Jump to table of contents

Robert Herzog

Churchill College

Cambridge

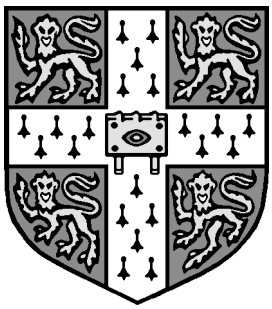

A dissertation submitted for the degree of Doctor of Philosophy at the University of Cambridge

December 1997

To my parents and my sister
who did not see me much during the last years.

Critical Currents in YBaCuO Thin Films

Summary

Nearly ten years ago $YBa_2Cu_3O_{7-\delta}$ (YBCO) was the first superconductor discovered with a transition temperature above the boiling point of liquid nitrogen, the 'magical' limit for high temperature superconductivity. Since then the interest in this ceramic compound has not abated. YBCO is one of the most promising materials for the application of high temperature superconductors (HTS) because it is able to carry a technically useful current density in applied fields at 77 K. Many experiments conducted to investigate the basic properties of the HTS and to further the theoretical understanding of them also used YBCO, because remarkable progress has been achieved in the preparation of bulk samples, single crystals and particularly thin films deposited by a variety of methods.

The aim of the experimental investigation presented in this thesis was to extend the understanding of the critical current density J_c in YBCO thin films. Specifically the dependence of J_c on the direction of an applied field was examined in detail by making use of a purpose-built two-axis goniometer, which allowed the rotation of a sample in any direction relative to a field of up to 8 tesla. Previous models trying to explain the strong anisotropy of J_c are reviewed and compared to the obtained experimental results. It was found that the layered crystal structure, which is responsible for the anisotropy of YBCO and all other cuperate HTS, has a direct influence on the angular dependence of J_c and that a description of the behaviour in terms of a two dimensional model is appropriate, particularly at low temperatures. At a given temperature the parameter with the strongest influence on J_c is the component of the magnetic field parallel to the crystallographic *c*-axis. This is unexpectedly even the case when the current is flowing parallel to the *c*-axis, as measurements on (110) oriented films show. Experiments where this field component is held constant revealed other factors influencing J_c in YBCO films, like the coupling of adjacent 'pancake' vortices and a Lorentz force in *c*-direction. An examination of films which were irradiated by fast heavy ions showed that J_c in this case not only depends on the field direction relative to the crystal axes and relative to the current direction but also relative to the irradiation direction.

Preface

I declare that, except where otherwise stated, this dissertation is the result of my own work and includes nothing which is the outcome of work done in collaboration. No part of this dissertation has been submitted at Cambridge or any other University for a degree or diploma or other qualification.

Robert Herzog
December 1997

Acknowledgements

First and foremost it is my very pleasant duty to thank *Dr Jan E. Evetts* for accepting me as his student and directing and supporting me during – as it turned out – many years. He always seemed to believe in my abilities (even when I had grave doubts) and was thus vital in motivating me to finish the work I had started.

Dr Peter Berghuis has studied subjects similar to the ones discussed in this thesis for many years and was therefore a very valuable source of knowledge, which he generously shared, about everything related to flux lines in superconductors. With his incredible patience and thoroughness *Peter* provided much needed constructive criticism. Thank you, *Peter*, for many hours of interesting discussions, which were often enlivened by your inimitable humour.

Together with *Jan Evetts*, *Drs Mark G. Blamire* and *Rob E. Somekh* were ran a very well rounded and complete set of experimental facilities in the *Device Materials Group* of the *Department of Materials Science*. Many thanks to *Mark* for the cleanroom facilities and to *Rob* for a number of excellent films from the sputtering "labyrinth".

For the production of other excellent films I am indebted to *Drs Gunther Wagner* and *Pjotr Przyslupski*; for inauguration into the cleanroom secrets to *Dr Zoe H. Barber*.

The lively and always cooperative atmosphere in *our lab* was certainly inspired by *Jan*, *Mark*, *Rob* and *Zoe*, but was definitely upheld by *all* diligent PhD students and PostDocs. Many, many thanks to *Bilgin Soylu*, *Christoph Schneider*, *Paul Warburton*, *Nikos Adamopoulos*, *Hilen Amin*, *Dorothy* and *Bartek Glowacki*, *Martin Goodchild*, *Jessica Owens*, *Shu Chen Fan*, *Janet Millner*, *Mazhar Bari* (called *bh*), *Gavin Burnell*, *Ed Tarte*, *Jun Huang*, *Yogesh Soman*, *Wilfred Booij*, *Martin Voss*, *Lucia Capogna*, *Robert Baranowski*, *Tim Jackson*, *Stephen Isaac*, *Daniel Jardine*, *Paul Kosmetatos*, *Ivan Nevirkovets*, *Ikuo Kanno*, *Sergei Kovtonyuk*, *Ahmed Kursumovic*, *Gary Stephens*, *Dolores Vasquez-Navarro*, *Bee-San Teo*, *Dan Watson*, *Pak-Kin Wong*, *Paul Aslin*, *Woo-Young Lee*, *Simon Turner* and *Yong-Yee Lim* for an excellent working environment, help in practical matters and many interesting discussions about all possible topics. With all of you *lab* was really fun.

I should also like to thank the *Department of Materials Science* and the *Interdisciplinary Research Centre in Superconductivity* for the generous provision of their facilities. Many thanks in particular to *Gary Chapman* for machining the components of the goniometer and *Keith Page* for building a precision stepping motor controller.

Churchill College contributed greatly to my wellbeing in Cambridge – I was very much at home in the hostels along *Storey's Way*, particularly in *N^o 64*. Many, many thanks to *Dr Alan Findley* and *Les Pepper*, the soul of the *MCR*, for all the patient support and help which they gave so generously. My thanks also go to all other *Churchillians* and in particular to the members of the *MCR*, a number of whom have become close friends. I remember the many 'chats' we had, which were not necessarily very serious (fortunately), but were always pretty sharp.

Finally I would like to express my gratitude to the *Austrian Ministry of Science and Research*, the *Austrian Chamber of Commerce*, the *Cambridge Overseas Trust*, the *Overseas Research Students Award*, and the *EU Human Capital and Mobility Programme* for financial support.

Contents

List of Symbols

Scalars and the magnitude of vectors are usually shown in italics; vectors and matrices in bold. Subscripts are in italics if they denote a variable or coordinate (F_x for the x component of **F**) and regular if they are an abbreviation for a word, like 'c' for critical in J_c or 'L' for Lorentz in F_L.

a, b, c	dimensions of the orthorhombic unit cell of YBCO
A	vector potential of the magnetic field
B	(applied) magnetic field
B_c	thermodynamic critical field
B_{c1}	lower critical field
B_{c2}	upper critical field
B_z	field component in c-direction
B_Φ	matching field (vortex density = defect density)
B_s	field generated by the current in the sample – self field
c_{11}	compression modulus of flux line lattice
c_{44}	tilt modulus of flux line lattice
c_{66}	shear modulus of flux line lattice
d	distance between CuO_2 layers
D	film thickness, sample dimensions
$\mathbf{e}_{irr}$	unit vector parallel to the irradiation direction
$\mathbf{e}_x$, $\mathbf{e}_y$, $\mathbf{e}_z$	unit vectors parallel to the coordinate axes
F_L	Lorentz force on flux line or Lorentz force density on flux line lattice
F_L^z	Lorentz force in z-direction (corresponds to c-direction in c-axis axis films)
F_L^p	Lorentz force on pancake vortex
F_L^s	Lorentz force on flux line string parallel to the ab-plane
F_p	pinning force on flux line per unit length or pinning force density on FLL
G	Gibbs free-energy density
J_o	depairing current density
J_c	critical current density; usually defined by a voltage criterion
J_{co}	'true' critical current density defined by $U(J_{co}) = 0$
ℓ	mean free path of electrons
M	effective mass of quasiparticles moving in c-direction
m	effective mass of quasiparticles moving within the ab-plane
n_s	density of superconducting electrons

r	variable to describe deviations from the 2D model (Equ. 4.24)
s	variable to describe the influence of F_L^z (Equ. 4.25)
T	temperature
T_c	critical temperature
U	pinning potential
V_{crit}	voltage criterion used to determine J_c
w	displacement of adjacent pancake vortices from the same flux line
α, β	Ginzburg-Landau parameters
Γ	$= 1/\varepsilon > 1$; anisotropy parameter
δ	parameter describing the oxygen content in $YBa_2Cu_3O_{7-\delta}$
ε	$= 1/\Gamma < 1$; anisotropy parameter
ε_ϑ	angle dependent anisotropy parameter
η	viscous drag coefficient
ϑ	angle between film normal and direction of applied magnetic field
ϑ_{irr}	angle between film normal and irradiation direction
κ	$= \lambda/\xi$; Ginzburg-Landau parameter
λ	magnetic penetration depth
λ_{ab}	penetration depth describing the decay length of currents parallel to the *ab*-plane
λ_c	penetration depth describing the decay length of currents parallel to the *c*-axis
μ_o	permeability of vacuum
ξ	Ginzburg Landau coherence length
ξ_{ab}	coherence length parallel to the *ab*-plane
ξ_c	coherence length parallel to the *c*-axis
ρ_n	normal state resistivity
φ	angle between current direction and component of magnetic field parallel to the *ab*-plane
φ_{irr}	angle between current direction and projection of irradiation direction into the *ab*-plane
Φ_o	magnetic flux quantum
ψ	superconducting order parameter
ω_o	characteristic vibration frequency of flux lines

Chapter 1

Introduction

The discovery of the first high temperature superconductors (HTS) by Bednorz and Müller (1986) marked the beginning of a new era, not only in the field of superconductivity but for solid state physics in general. The prospect of new applications and the initially fast climbing record critical temperature (T_c) attracted a large number of scientists who published a vast amount of work. However, although the knowledge about the new materials has increased remarkably over the last years, no complete theoretical picture has yet emerged, particularly because the binding mechanism of electron pairs is still unknown. Considerable progress towards application of the HTS in practical devices has been achieved, but so far only a small number of niche products, such as current leads for cryogenic installations, are on the market.

The practical difficulties associated with the HTS originate from a number of unusual properties and parameter values. The small size of the coherence length ξ in the HTS originates from the high T_c and the low Fermi velocity, which in turn stems from the low free electron density (Tinkham, 1996, p.16). Small coherence lengths imply large upper critical fields B_{c2}. Values up to several thousand tesla at $T = 0$ have been estimated for BiSCCO (Palstra *et al*., 1988a). Since ξ is of the order of a few Å to a few tens of Å, disorder on an atomic scale can have an influence on the superconducting behaviour of a material. Possibly the biggest difficulty in this context proved to be grain boundaries across which the coupling of the superconducting state is weak, and critical current densities (J_c) are severely reduced. On the other hand point defects and columnar defects with dimensions comparable to ξ can be effective pinning centres and large J_c values have been obtained in materials not (or to a lesser extent) affected by the grain boundary problem. From the small ξ also follows that $\kappa = \lambda/\xi$ is large, making the HTS extreme type II superconductors (λ is the magnetic penetration depth).

A consequence of the high critical temperature and the small coherence length is that fluctuation effects play a prominent role in the HTS. In conventional type II superconductors the critical region, where fluctuations are relevant, is limited to a narrow regime

around T_c or $B_{c2}(T)$. In the HTS on the other hand a broadening of the resistive transition to a width of more than 10 K has been observed in strong magnetic fields (Iye *et al.*, 1990; Palstra *et al.*, 1988b) and dissipative mechanisms prevail in a large part of the B-T phase diagram below the $B_{c2}(T)$ line. To separate this regime from the one showing the more conventional behaviour of a pinned, rigid flux line lattice, the irreversibility line was introduced. This was originally defined by the field (at a given temperature) where irreversibility disappears in magnetisation measurements. More recently Zeldov *et al.* (1995) reported the observation of a first order phase transition (a melting) of the flux line lattice with a very small latent heat, which could give the irreversibility line a more precise definition.

Nearly all HTS contain characteristic CuO_2 planes parallel to the crystallographic *ab*-plane where the free charge carriers and hence superconductivity are concentrated. These planes and the non-superconducting layers in between form a layered crystal structure which is the origin of a large anisotropy of electrical and magnetic quantities. In materials like the Bi and Tl compounds, where the coupling between adjacent CuO_2 layers is particularly small, the anisotropy parameter $\Gamma = M/m$ can be as large as 3000 (Farrel *et al.*, 1989; M and m are the effective masses for quasiparticle movement in *c*-direction and parallel to the *ab*-plane respectively). In many cases it is useful to describe these superconductors with a 2 dimensional model. The anisotropy of $YBa_2Cu_3O_{7-\delta}$, the sample material used in this thesis, is not as extreme, but with a Γ of 25 still large (Farrel *et al.*, 1988).

1.1 Subject and aim of this thesis

The anisotropy of the critical current density in $YBa_2Cu_3O_{7-\delta}$ (YBCO) is the central topic of this thesis. J_c in the HTS not only strongly depends on the direction the current is flowing in (parallel or normal to the *c*-axis), but also on the direction of an applied field, both relative to the crystal axes and relative to the current direction. On the basis of experiments with a few elementary configurations a number of models have been developed to explain the observed behaviour (Tachiki and Takahashi, 1989; Kes *et al.*, 1990; Blatter *et al.*, 1992). One main aim of this thesis was a comparison of these models and an experimental evaluation of their validity for the YBCO system. A second

objective was the investigation of new geometrical configurations (combinations of current and magnetic field directions relative to the crystal axes and to each other), which could be realised with a purpose-built goniometer in an 8 T superconducting solenoid and a new film type where a current can be applied in *c*-direction. Most experiments investigating J_c in YBCO films so far only investigated *c*-axis films, in which the crystallographic *c*-axis is normal to the film plane and an applied current is restricted to flowing in the *ab*-plane. A final aim was to study the change of the pinning behaviour caused by artificially introduced columnar defects, which, since they are strongly directed, have a marked influence on the functional dependence of J_c on the direction of an applied field.

The main motivation for this work was the wish for a better understanding of the current carrying capabilities of YBCO in an applied magnetic field, which is of theoretical as well as of practical interest. YBCO is in principle one of the most attractive high temperature superconductors for applications at 77 K, because the irreversibility line is only reached at comparatively large applied fields. In the extremely anisotropic Bismuth compounds on the other hand J_c is strongly reduced with applied fields at this temperature. The main obstacle for the use of YBCO in large scale applications so far is the difficulty of aligning the *ab*-planes of neighbouring grains (texturing) in order to create current paths with no component in *c*-direction, and the grain boundary problem in general. The nature of the dimensionality in YBCO is one of the theoretical questions associated with the dependence of J_c on the direction of an applied field. It was one of the aims of this thesis to identify the regimes where the layered structure of the material has to be explicitly considered to describe the J_c dependence and where the anisotropic but homogeneous Ginzburg-Landau theory is sufficient.

1.2 Overview of the thesis

A brief introduction into the theory of critical currents in type II superconductors, which is largely based on the Ginzburg Landau theory, is presented in chapter 2. A number of additional, HTS specific topics, such as the crystal structure of YBCO, concepts of layered superconductors, and thermal activation effects are discussed as well.

Chapter 3 explains the experimental equipment and procedures used. They can be grouped into the two distinct fields of sample preparation and electrical transport measurements at cryogenic temperatures. The former involved the vapour deposition of contact pads onto the newly sputtered samples, oxygen annealing in an UHV system and the patterning of a test structure with photolithographic methods. The critical temperature T_c of all samples was determined by measuring the transport resistivity as a function of T at several stages in the sample preparation process. Critical current measurements, the main experimental activity for this thesis, were performed in a commercial cryostat with a superconducting solenoid and a variable temperature insert. A purpose-designed and custom-built two-axis goniometer allowed the rotation of a sample in the magnetic field generated by the solenoid in such a way that all possible field directions relative to the sample could be realised. The chapter closes with a description of the electrical circuits and the data acquisition software used for the J_c measurements.

A detailed investigation of critical currents in *c*-axis films is the central part of this thesis and the subject of chapter 4. Firstly previous experiments and their interpretations are reviewed and the models introduced which attempt to explain the J_c dependence on the direction of an applied field. A comparison of the various models with experimental results showed that the 2D model proposed by Kes *et al*. (1990) provides the best description of the data. Because it is based on concepts of layered superconductors, the shape of flux lines and forces acting on them is reviewed in some detail in section 4.4, which concludes with a model of forces on a pancake vortex (a two dimensional vortex) and equilibrium conditions for them. The main result of this simple model is a prediction for the J_c dependence in experiments where the applied field is rotated around the *c*-axis but the angle between field and *c*-axis is kept constant (φ-scans; see Fig. (4.29)). The data obtained in such measurements are in good agreement with the model in a surprisingly large range of temperatures and other parameters. The chapter concludes with an analysis of deviations from the 2D model and the change of J_c following a reduction of the oxygen content of the films.

To enable J_c measurements with the current flowing parallel to the *c*-axis, (110) YBCO films were prepared. In these films the *c*-axis of most grains is aligned with the substrate *c*-axis, which is parallel to the film surface. It is thus possible to pattern current tracks

parallel and normal to the *c*-axis in order to apply currents in the respective directions. The characterisation of (110) films and measurements of their critical current density are presented in chapter 5. When the current is flowing parallel to the *ab*-plane, a symmetry of the angular dependence of J_c is observed which is similar to the one in *c*-axis films, although some characteristic features are missing. This is probably a result of the different microstructure. J_c measurements with the current flowing parallel to the *c*-axis show the surprising result that the angle between applied field and current direction has much less influence on J_c than the angle between field and *c*-axis, in contrast to conventional theories of flux line depinning at J_c.

Some *c*-axis samples were irradiated with fast heavy ions to investigate the change of their pinning behaviour. Since this type of irradiation produces elongated defects parallel to the trajectories of the ions, correlated pinning can be observed when the magnetic field is aligned with the defects. Thus J_c not only depends on the direction of the applied field relative to the crystal axes and the current direction, but also relative to the irradiation direction, as the experiments presented in chapter 6 confirm. The additional defects generally increase J_c, particularly for fields smaller than the matching field B_m applied parallel to the *c*-axis (At B_m the flux line density equals the defect density.).

At the end of this thesis, in chapter 7, the main results of the measurements conducted for this thesis are summarised and the conclusions reviewed, which have been drawn from the experimental evidence. Further studies to clarify some points or to expand the investigation of critical currents in YBCO films into different regimes are suggested.

1.3 References

Bednorz, G. and K.A. Müller, 1986, Z. Phys. **B64**, 189.

Blatter, G., V.B. Geshkenbein and A.I. Larkin, 1992, Phys. Rev. Lett. **68** (6), 875-878.

Farrel, D.E., S. Bonham, J. Foster, Y.C. Chang, P.Z. Liang, K.G. Vandervoort, D.J. Lam and V.G. Kogan, 1989, Phys. Rev. Lett. **63**, 782.

Farrel, D.E., C.M. Williams, S.A. Wolf, N.P. Bansal and V.G. Kogan, 1988, Phys. Rev. Lett. **61**, 2805.

Iye, Y., S. Nakamura, T. Tamegai, T. Terashima, K. Yamamoto and Y. Bando, 1990, Physica C **166**, 62-70.

Kes, P.H., J. Aarts, V.M. Vinokur and C.J. van der Beek, 1990, Phys. Rev. Lett. **64** (9), 1063-1066.

Palstra, T.T.M., B. Batlogg, L.F. Schneemeyer, R.B. van Dover and J.V. Waszczak, 1988a, Phys. Rev. B **38**, 5102.

Palstra, T.T.M., B. Batlogg, R.B. van Dover, L.F. Schneemeyer and J.V. Waszczak, 1988b, Appl. Phys. Lett. **54** (8), 763-765.

Tachiki, M. and S. Takahashi, 1989, Solid State Communications **72** (11), 1083-1086.

Tinkham, M., 1996, *Introduction to Superconductivity*. New York, McGraw-Hill.

Zeldov, E., D. Majer, M. Konczykowski, V.B. Geshkenbein, V.M. Vinokur and H. Shtrikman, 1995, Nature **375**, 373-376.

Chapter 2

Critical Currents in High T_c Superconductors

Ginzburg and Landau (1950) developed a subsequently very successful phenomenological theory of superconductivity by applying general principles of second order phase transitions to the superconducting transition in applied magnetic fields. A few years later Abrikosov (1957) found a solution of the Ginzburg-Landau equations which allowed an applied magnetic field to penetrate type-II superconductors in quantised threads, now called flux lines. High supercurrents in an applied field can only be achieved in type-II materials, where the critical current density is determined by the balance of Lorentz forces and maximal pinning forces on flux lines. Ginzburg and Landau developed their theory several years *before* the microscopic BCS theory explained superconductivity for the first time from first principles[1]. It is ironic that now, with the detailed microscopic mechanisms of the High Temperature Superconductors (HTS) still unknown, the Ginzburg-Landau theory again provides an undisputed phenomenological foundation for the description of the HTS. All interpretations of experiments in this thesis and many of the parameters used are based on the Ginzburg-Landau theory. The theory is therefore briefly sketched further down in its anisotropic form, which the strongly anisotropic HTS require.

Apart from the anisotropy, two other unusual properties of the HTS are pervasive in all descriptions: Firstly the crystal lattice has a layered structure, with the layer spacing comparable to the coherence length normal to the layers in a wide temperature range. This layering has a strong influence on the structure and pinning of flux lines in HTS. Secondly the much higher T_c of the HTS opens up superconducting regimes at significantly higher temperatures than known from conventional superconductors and effects of thermal activation become many orders of magnitude more important than at usual low-T_c temperatures[2].

---

[1] P. G. de Gennes called this achievement of Ginzburg and Landau a "tour de force of physical intuition" in his introductory book to superconductivity (de Gennes, 1966).

[2] "Relaxation processes which would not occur in the age of the universe at 4 K, will occur in a millisecond at 77 K" (Tinkham, 1996, page 332)

These are the main points which are dealt with in this background chapter. In addition a number of other relevant topics will be touched on, like the following explanation of the crystal structure of $YBa_2Cu_3O_{7-\delta}$ (YBCO), the sample material of this thesis.

2.1 Crystal structure of YBCO

Only a few months after the surprising discovery of superconductivity in $(La,Ba)_2CuO_4$ by Bednorz and Müller (1986) with a then record T_c of 35 K, the YBCO system was found to be superconducting at temperatures above 90 K (Wu *et al.*, 1987; Zhao *et al.*, 1987; Hikami *et al.*, 1987). The first samples consisted of a mixture of phases, but gradually it became clear that the $YBa_2Cu_3O_{7-\delta}$ structure shown in Fig. 2.1 with $\delta \approx 0.03$ has the highest T_c of 92 K. This structure is, like that of many HTS, a complex variation of the perovskite structure, which has the general chemical formula ABO_3. The perovskite structure is cubic with one metal (A) at the centre of the unit cell, the other

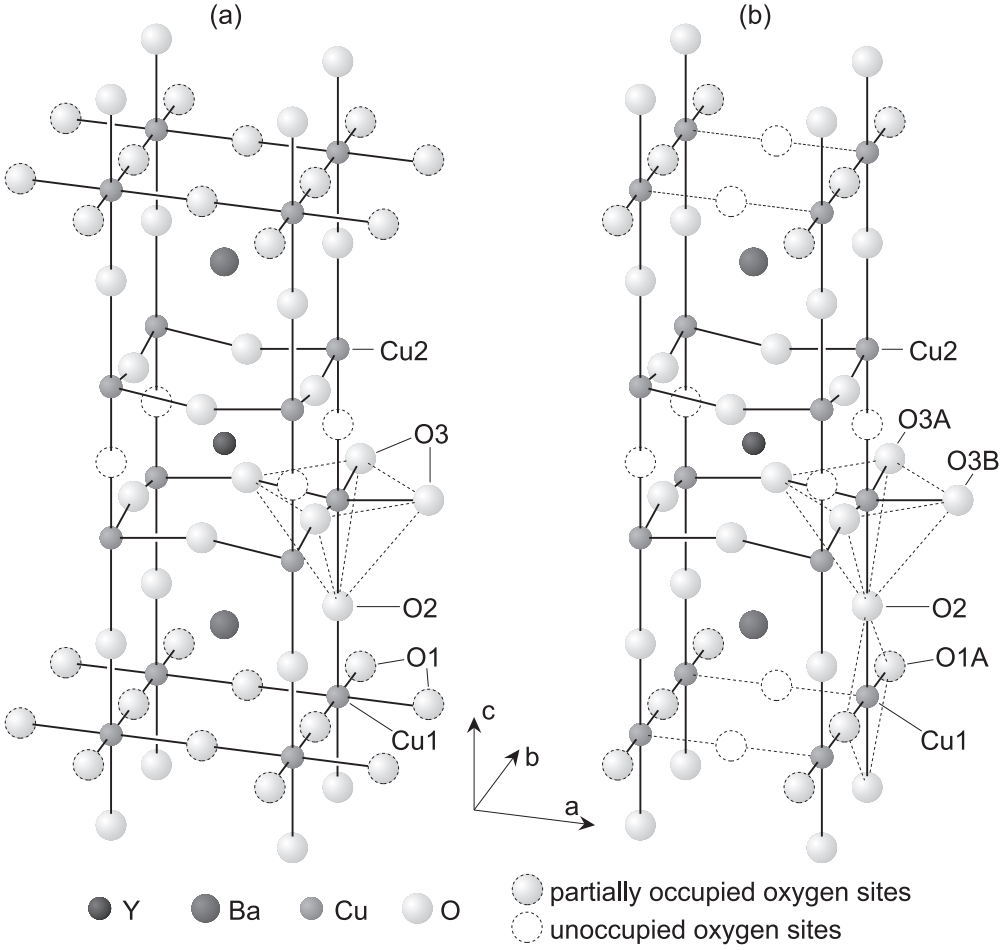

Figure 2.1
The crystal structure of $YBa_2Cu_3O_{7-\delta}$ is tetragonal for $\delta \gtrsim 0.5$ (a) and orthorhombic for $\delta \lesssim 0.5$ (b). Note that less than a quarter of the positions O1 are occupied in the tetragonal structure (a) and only for $\delta = 0$ all positions O1A are occupied in the orthorhombic structure (b).

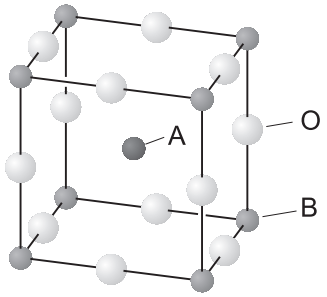

Figure 2.2
The crystal structure of perovskites (ABO_3). $SrTiO_3$, the substrate material of many samples, has this structure. (The mineral perovskite is $CaTiO_3$.)

(B) at the corners and the oxygen occupying the sites at the centre of the cube edges (see Fig. 2.2).

The YBCO unit cell consists of an $YCuO_3$ cube with adjacent $BaCuO_3$ cubes above and below, but with some oxygen sites not occupied. The oxygen sites on the same horizontal plane as the yttrium atom are never occupied, allowing the O3 atoms to slightly move towards the Y. The oxygen sites on the basal plane can have average occupancies between 0 ($\delta = 1$) and 0.5 ($\delta = 0$). Oxygen is comparatively mobile in this plane and nearly full oxygenation ($\delta \approx 0.03$) is crucial to obtain samples with high transition temperatures. The dependence of T_c on δ is shown in Fig. 2.3 (Ossandon *et al.*, 1992). Samples with a low oxygen content ($\delta \gtrsim 0.5$) have a tetragonal structure with the (few) oxygen atoms distributed randomly over all sites in the basal plane. If δ is smaller than 0.5, the oxygen atoms arrange in chains with the copper, resulting in a reduction of symmetry and a transition to the orthorhombic structure (see Fig. 2.1b). Only the O1A sites contain oxygen atoms – the O1B sites are not occupied. The dimensions of the unit cell in the tetragonal case ($\delta \approx 0.5$) are $a = b = 0.387$ nm and $c = 1.172$ nm, in the orthorhombic case ($\delta \approx 0.1$) $a = 0.382$ nm, $b = 0.388$ nm and $c = 1.168$ nm. Using x-ray scattering methods it is possible to measure the slight variations of the c-axis length and a correlation between δ and c has been established.

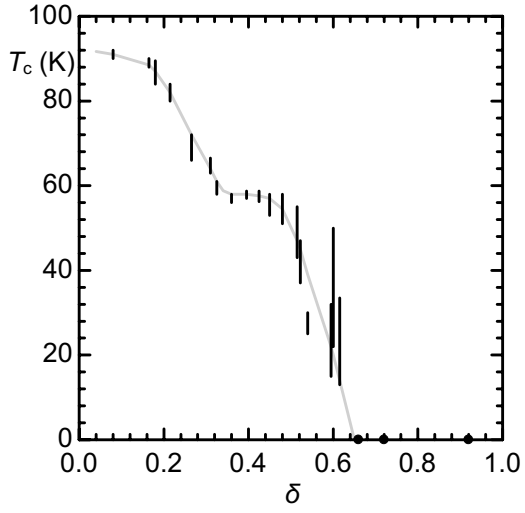

Figure 2.3
Dependence of T_c on δ in $YBa_2Cu_3O_{7-\delta}$.

Orthorhombic YBCO is formed when the tetragonal phase is slowly cooled in a sufficiently concentrated oxygen environment at roughly 680 °C. In most cases this transition creates a large number of different twin domains for reasons of stress release in the material. The spacing of the twin boundaries is in the order of 200 nm, substantially smaller than most sample sizes. Except for samples where the twin bounda-

ries have been deliberately removed, macroscopic measurements will always probe a large number of twin domains, effectively averaging over the *a* and *b* directions. But even in de-twinned samples the anisotropy within the *ab*-plane is small, such that for most purposes it is sufficient to assume uniaxial anisotropy (*ab*-plane versus *c*-axis) for YBCO and other HTS. This anisotropy however can be very large and must always be considered.

Many experiments have shown that the conductivity in the *ab*-plane of the HTS is much higher than along the *c*-axis. Band structure calculations of YBCO revealed that the high *ab*-plane conductivity arises from the two dimensional lattice formed by the Cu2 and O3 atoms. The region formed by the Cu1, O1 and O2 is much less conductive, but acts as a charge reservoir for the two Cu2-O3 planes (CuO_2 planes) per unit cell. In this way the oxygen occupancy at the O1A site ('chain site') influences the carrier density in the CuO_2 planes and thereby the macroscopic electronic properties. The strong co-ordination between the Cu2, O2 and O3 atoms is indicated by the inverted pyramids in Fig. 2.1, the co-ordination between the Cu1, O1A and O2 by the dashed rhombus.

A very important feature of YBCO is that the CuO_2 double layers (formed by the two layers next to the Y^{3+} ions) are nearly isolated from the adjacent double layers in *c*-direction. This near isolation is so strong that it is often useful to describe the electronic structure of YBCO as well conducting CuO_2 double layers, separated by the layers containing the CuO chains. All HTS have a similar layered structure. In some materials (e.g. BiSCCO) the isolation of the characteristic CuO_2 layers is even more pronounced than in YBCO. In YBCO the degree of layering furthermore depends on the oxygenation level (δ), since, as noted above, the amount of oxygen has a strong influence on the electronic structure. An increase of δ (reduction of oxygen) reduces the coupling between adjacent oxygen double layers.

2.2 Basic phenomenological theory

The discovery stimulating the first successful phenomenological descriptions of superconductivity was the observation by Meissner and Ochsenfeld (1933) that magnetic flux is completely expelled from a type-I sample when cooled in an applied magnetic field. This ideal diamagnetism, now called Meissner effect, could not be explained by zero

electrical resistance of the superconductor alone since there is no changing field which could induce shielding currents in this experiment. The Meissner effect rather shows that ideal diamagnetism is a fundamental property of superconductors, just like the zero resistance, and that superconductivity is a true thermodynamic state with a lower energy than the normal state. Starting from these two properties F. and H. London (1935) developed their phenomenological theory using only electrodynamic principles which resulted in the two London equations:

$$\mathbf{E} = \frac{\partial}{\partial t}(\lambda_L^2 \mu_o \mathbf{J}_s) \tag{2.1}$$

$$\mathbf{B} = -\operatorname{curl}(\lambda_L^2 \mu_o \mathbf{J}_s) \tag{2.2}$$

where

$$\lambda_L = \sqrt{\frac{m}{\mu_o n_s e^2}} \tag{2.3}$$

is the London penetration depth, m the effective electron mass, n_s the density of super-electrons and J_s the supercurrent density. Equation (2.1) replaces Ohm's law in a superconductor: An electric field is accelerating the carriers of the supercurrent rather than just maintaining their drift velocity against scattering. Both equations can be derived more profoundly from a quantum mechanical consideration (Evetts, 1992, p 554; Tinkham, 1996, p 5): A theorem of Bloch shows that the net canonical momentum $\mathbf{p} = (m\mathbf{v} + e\mathbf{A})$ equals zero in the ground state with no applied field. If one postulates that the wave function is "rigid" and retains its ground state property $\langle \mathbf{p} \rangle = 0$ even with applied fields, one gets the relation

$$\mathbf{J}_s = n_s e \langle \mathbf{v}_s \rangle = \frac{-n_s e^2 \mathbf{A}}{m} = \frac{-\mathbf{A}}{\mu_o \lambda_L^2}. \tag{2.4}$$

Taking the time derivative of both sides gives Equ. (2.1) and taking the curl leads to Equ. (2.2). The continuity condition for $\mathbf{J}$ ($\operatorname{div} \mathbf{J} = 0$) requires that $\operatorname{div} \mathbf{A} = 0$. This so called London gauge is a boundary condition for all equations of the London theory.

Inserting the fourth Maxwell equation ($\mu_o \mathbf{J} = \operatorname{curl} \mathbf{B}$) into (2.2) gives

$$\mathbf{B} + \lambda_L^2 \operatorname{curl}\operatorname{curl} \mathbf{B} = \mathbf{B} + \lambda_L^2 (\Delta \mathbf{B} + \operatorname{grad}\operatorname{div} \mathbf{B}) = \mathbf{B} + \lambda_L^2 \Delta \mathbf{B} = 0. \tag{2.5}$$

This equation can be solved for the interior of a superconductor. The solution describes the exponential decay of an applied field at the surface on a scale of λ_L – hence the name London penetration depth.

Another method of deriving the London equations uses a thermodynamic approach similar to the Ginzburg-Landau theory below. Three terms contribute to the free energy G of a superconductor within the London model:

$$G = \int d^3r \left(G_s(\mathbf{r}) + \frac{n_s}{2} m \mathbf{v}_s^2(\mathbf{r}) + \frac{B^2(\mathbf{r})}{2\mu_o} \right) \tag{2.6}$$

The first term represents the condensation energy, the middle term the kinetic energy of the screening currents and the last term the energy of the magnetic field. Since $G_s(\mathbf{r})$ is constant throughout a sample within the London model, it can be readily integrated. Expressing $\mathbf{v}_s$ by $\mathbf{J}_s$ and then replacing $\mu_o \mathbf{J}_s$ by curl $\mathbf{B}$ finally gives

$$G = G_s + \frac{1}{2\mu_o} \int d^3r \left(\lambda^2 (\text{curl}\, \mathbf{B}(\mathbf{r}))^2 + \mathbf{B}^2(\mathbf{r}) \right) \tag{2.7}$$

Minimising G with respect to the local field $\mathbf{B}$ leads directly to Equ. (2.5).

2.3 Anisotropic Ginzburg-Landau theory

Concepts from the Ginzburg-Landau theory provide the basis for the interpretation of experiments in this thesis. Ginzburg and Landau (1950) introduced a complex pseudo wavefunction, the order parameter $\psi = |\psi| e^{i\varphi}$, to describe the superconducting condensate, where $|\psi|^2$ is proportional to n_s, the density of superconducting electrons in the London model. Developing the condensation energy in powers of $|\psi|^2$ near T_c, which seemed appropriate for a second order phase transition, they proposed the free energy functional

$$G_s = G_n + \int d^3r \left[\alpha |\psi|^2 + \frac{\beta}{2} |\psi|^4 + \sum_{j=1}^{3} \frac{1}{4m_j} \left| \left(\frac{\hbar}{i} \frac{\partial}{\partial x_j} - 2eA_j \right) \psi \right|^2 + \frac{B^2}{2\mu_o} - \mathbf{HB} \right], \tag{2.8}$$

which is given here in anisotropic form to take the different effective masses for electron movement in different directions into account. α and β are the material specific

GL parameters, m_j the effective masses for electron movement in j-direction, **A** the vector potential, **B** the microscopic magnetic field and **H** the externally applied magnetic field. G_n is the free energy of the normal state. The first two terms in the integral describe the superconducting condensation energy expressed as a series expansion of $|\psi|^2$, the sum is a gauge-invariant expression for the kinetic energy of the superfluid and the last two terms take the magnetic energy of the system into account. $\alpha = \alpha(0)(1 - T/T_c)$ near T_c, where $\alpha(0)$ must be less than zero for a non-zero solution of ψ. β is constant near T_c. (For more details on the GL theory see e.g.: Evetts, 1992, p 575; Tinkham, 1996, p 110; Blatter *et al*., 1994)

The functions $\psi(\mathbf{r})$ and $\mathbf{B}(\mathbf{r})$ yielding the minimum free energy describe the equilibrium state of the system. They can be found by variation of (2.8) with respect to ψ and **A** which gives the two coupled GL differential equations. They need to be solved for given boundary conditions.

$$\alpha\psi + \beta|\psi|^2\psi + \sum_{j=1}^{3}\frac{1}{4m_j}\left(\frac{\hbar}{i}\frac{\partial}{\partial x_j} - 2eA_j\right)^2\psi = 0 \tag{2.9}$$

$$J_j = \frac{1}{\mu_o}\mathrm{curl}_j\,\mathbf{B} = \frac{e\hbar}{2im_j}\left(\psi^*\frac{\partial\psi}{\partial x_j} - \psi\frac{\partial\psi^*}{\partial x_j}\right) - \frac{2e^2}{m_j}\psi^*\psi A_j = \frac{e}{m_j}|\psi|^2\left(\hbar\frac{\partial\varphi}{\partial x_j} - 2eA_j\right) \tag{2.10}$$

Two important length scales closely related to α and β can be introduced and used as the materials constants specifying a particular superconductor. These length scales are the GL coherence length $\xi(T)$ and the penetration depth $\lambda(T)$. The connection between ξ, λ and α, β and their temperature dependence (close to T_c) in the anisotropic case is:

$$\xi_i^2(T) = \frac{\hbar^2}{4m_i|\alpha(T)|} = \frac{\xi_i^2(0)}{1 - T/T_c}, \qquad \lambda_i^2(T) = \frac{\beta m_i}{2\mu_o e^2|\alpha(T)|} = \frac{\lambda_i^2(0)}{1 - T/T_c} \tag{2.11}$$

Replacing α and β in Equ. (2.9) with ξ and λ shows that the latter two determine the scale of spatial variations of the order parameter and the magnetic field respectively. Abrikosov (1957) calculated general solutions of the GL equations, which could be classified in two groups depending on whether $\kappa = \lambda/\xi$ is smaller or larger than $1/\sqrt{2}$. For the former the surface energy between a superconducting and a normal region inside a sample is positive (type-I SC), for the latter it is negative (type-II SC). In type-I

superconductors the surface separating superconducting and normal regions (phases) is minimal in equilibrium. In type-II samples on the other hand the phase penetrated by a magnetic field (normal phase) splits into ever more domains until a quantum limit is reached. This limit is the minimal flux Φ_o, which a normal conducting region has to carry to preserve the coherence of the superconducting order parameter ψ. The flux quantum $\Phi_o = h/2e$ is of fundamental importance to superconductivity (h is Planck's constant, e the elementary charge).

The GL coherence length ξ may be obtained from the BCS coherence length ξ_o, a parameter in the BCS theory describing the extent of a Cooper pair, as follows:

$$\xi \approx \sqrt{\xi_o \ell} \quad \text{with} \quad \xi_o \approx \frac{E_F}{k_B T_c n^{1/3}} \approx \frac{h^2 n^{1/3}}{m k_B T_c} \tag{2.12}$$

where E_F is the Fermi energy, n the free carrier density, and ℓ the mean free path of electrons. In clean LTS ($\ell \gg \xi_o$) typical values result in a ξ of about 1 μm. In technical materials (like NbTi), which are deliberately made dirty to increase B_{c2}, ξ can be as little as 5 nm, but in the HTS small n, small ℓ, large $m \approx 10 m_e$ and a high T_c conspire to severely reduce ξ to the order of 1 nm. This is much smaller than λ, such that $\kappa \gg 1$ and the HTS are therefore strongly type-II.

Another set of parameters describing type-II superconductors sufficiently are the critical fields B_c, B_{c1} and B_{c2}. B_c is defined by the superconducting condensation energy density $g_s - g_n = B_c^2/2\mu_o = -\alpha^2/2\beta$. The last equality can be derived by considering Equ. (2.8) in the absence of a magnetic field and far form any boundaries (homogenous equilibrium case; see Tinkham, 1996, p 113).

In an increasing applied magnetic field B_{c1} (lower critical field) is the value where field starts to penetrate a type-II superconductor in the form of quantised flux lines and B_{c2} (upper critical field) the field where superconductivity is completely suppressed. In the isotropic case B_{c1} and B_{c2} can be calculated from λ and ξ as follows:

$$B_{c1} = \frac{\Phi_o}{4\pi\lambda^2}(\ln\kappa + 0.081) = \frac{B_c}{\sqrt{2}\kappa}(\ln\kappa + 0.081) \qquad B_{c2} = \frac{\Phi_o}{2\pi\xi^2} = \sqrt{2}\kappa B_c \tag{2.13}$$

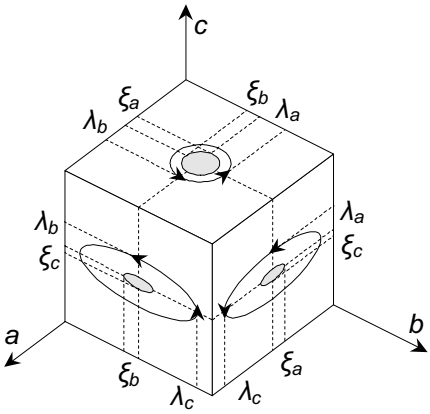

Figure 2.4
Screening currents and cores of flux lines parallel to different crystal axis in anisotropic superconductors.

In the LTS magnetisation measurements and the inverse of these equations are often used to determine λ and ξ. With the HTS the determination of B_{c1} is difficult because the magnetisation rises substantially even above B_{c1} due to strong pinning in most samples. B_{c2} on the other hand is very large and rises sharply with the temperature dropping below T_c (≈ 2 T/K) such that only a small range below T_c is experimentally accessible. Furthermore this regime close to T_c is strongly influenced by thermal fluctuation effects such that an extrapolation to determine B_{c2} at $T = 0$ is difficult.

Since B_{c1} and B_{c2} are closely related to the anisotropic λ and ξ they are strongly anisotropic themselves. It is however easy to get the different axes confused: λ_i describes the screening by *supercurrents* flowing along the *i*th axis, *not* the screening of a *magnetic field* along the *i*th axis (Clem, 1992). Fig. 2.4 schematically shows the cross-section of flux lines parallel to the three crystal axes. The order of the drawn lengths is correct (i.e. $\xi_c < \xi_a \approx \xi_b < \lambda_a \approx \lambda_b < \lambda_c$), but they are not to scale. In YBCO $\xi_a \approx 5\xi_c$, $\lambda_c \approx 5\lambda_a$ and $\lambda_a \approx 100\xi_a$. Since the *ab*-anisotropy in YBCO is only about 1.1 no further distinction between the parameters for the *a*-axis and the *b*-axis is made and $\xi_{ab} = \xi_a = \xi_b$ and $\lambda_{ab} = \lambda_a = \lambda_b$. The anisotropic equivalent to Equ. (2.13) finally are (see also Equ. (2.11))

$$B_{c1}^{c} = \frac{\Phi_0}{2\pi\lambda_{ab}^2}(\ln\kappa_c + 0.081) \qquad B_{c1}^{ab} = \frac{\Phi_0}{2\pi\lambda_{ab}\lambda_c}(\ln\kappa_{ab} + 0.081)\,, \tag{2.14}$$

where the upper indices indicate the field direction, and

$$B_{c2}^{c} = \frac{\Phi_0}{2\pi\xi_{ab}^2} \qquad B_{c2}^{ab} = \frac{\Phi_0}{2\pi\xi_{ab}\xi_c}\,. \tag{2.15}$$

Here the anisotropic GL-parameters κ_i, for fields in *i*-direction, are given by

$$\kappa_c = \frac{\lambda_{ab}}{\xi_{ab}} \qquad \kappa_{ab} = \frac{\lambda_c}{\xi_{ab}} = \sqrt{\frac{\lambda_c}{\xi_c}\frac{\lambda_{ab}}{\xi_{ab}}}\,. \tag{2.16}$$

Using Equ. (2.11) one can directly see how the ratios of λ and ξ are related to the anisotropy parameter ε, defined by the square root of the effective mass ratio m_{ab}/m_c:

$$\varepsilon = \frac{1}{\Gamma} = \sqrt{\frac{m_{ab}}{m_c}} = \sqrt{\frac{m}{M}} = \frac{\lambda_{ab}}{\lambda_c} = \frac{\xi_c}{\xi_{ab}} \tag{2.17}$$

Since m_c is much larger than m_{ab}, ε is considerably smaller than 1 for the HTS and about 1/7 – 1/5 for YBCO. In the literature Γ is often used as the anisotropy parameter, m and M as the effective masses for in plane (m_{ab}) and out of plane (m_c) movement respectively.

With the anisotropic GL-theory it is also possible to calculate all the above parameters for tilted applied fields (Klemm and Clem, 1980; Kogan and Clem, 1987; Clem, 1992). For example B_{c2} varies with ϑ, the angle between applied field and the c-axis, like

$$B_{c2}(\vartheta) = \frac{B_{c2}^{c}}{\varepsilon_\vartheta}, \tag{2.18}$$

where

$$\varepsilon_\vartheta = \sqrt{\cos^2\vartheta + \varepsilon^2 \sin^2\vartheta} \tag{2.19}$$

is the angle dependent anisotropy factor. The parameter ε_ϑ is important for this study since it appears in all expressions describing angular variations of experimental quantities derived from the anisotropic GL-theory.

2.4 Flux lines in type-II superconductors

The concept of flux lines (FL), each carrying a flux quantum Φ_o, became much more generally used soon after the discovery of the Abrikosov solution of the GL equations in the mixed state ($B_{c1} < B < B_{c2}$) and experimental proof of their existence by Essmann and Träuble (1967).

In the centre of each flux line the order parameter goes to zero. The region with suppressed order parameter around this centre is a cylinder with radius ξ. In anisotropic superconductors the circular cross-section is distorted to an ellipse. The core of a tilted flux line is shown schematically in Fig. 2.5 with the dimensions ξ_{ab} parallel to the ab-plane and $\varepsilon_\vartheta\xi_{ab}$ normal to the field direction and normal to the major axis parallel to the ab-plane (i.e. in y'-direction). $\varepsilon_\vartheta\xi_{ab}$ becomes ξ_{ab} for $\vartheta = 0°$ and $\varepsilon\xi_{ab}$, which is just ξ_c,

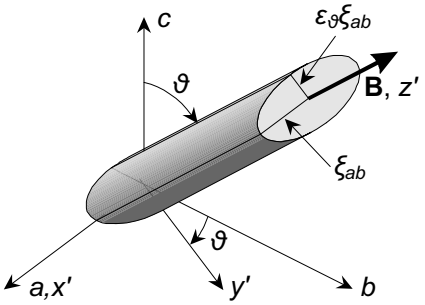

Figure 2.5
Tilted flux line in uniaxially anisotropic superconductor. The dashed co-ordinate system is tilted with the flux line.

for $\vartheta = 90°$. Circular (or elliptical) shielding currents surround each flux line such that the fluxon is exactly Φ_o. The magnetic field has a local maximum at the centre of the flux line and drops to zero on a length λ. Both, the reduction of the order parameter as well as the shielding currents increase the energy of a system, the first due to a reduction of the superconducting condensation energy, the latter due to the kinetic energy of the current carriers and the local magnetic field energy. These effects result in an energy per unit length (self energy) and a line tension to be associated with a flux line.

A vortex exposed to a laminar current flow **J** (e.g. a macroscopic transport current) is subject to a Lorentz force per unit length $\mathbf{f}_L = \Phi_o \mathbf{J} \times \mathbf{n}$, where **n** is a unit vector along the flux line. Averaged over several flux lines this leads to the important relation for the Lorentz force density

$$\mathbf{F}_L = \mathbf{J} \times \mathbf{B} \tag{2.20}$$

This force can be derived by calculating the interaction energy of flux lines (Tinkham, 1996, p 154) or by hydrodynamic considerations and is similar to the Magnus force (Blatter *et al*., 1994, p 1143).

When two flux lines in the interior of a sample come to within a distance λ of each other, their shielding currents and magnetic fields result in a mutual Lorentz force. Since the arrangement is symmetrical this leads to an identical force on both flux lines, which is repulsive for parallel vortices. At applied magnetic fields sufficiently above B_{c1}, where a large number of flux lines penetrate a sample, this mutual repulsion leads to a 2-dimensional lattice, the flux line lattice. Only for a regular lattice the net force on each flux line is zero. In an isotropic superconductor this lattice has a hexagonal symmetry, but in an anisotropic material the symmetry is distorted.

The mutual repulsion together with the line tension of flux lines have been successfully used to develop an elasticity theory of the flux line lattice. The symmetry of the problem reduces the number of independent elastic moduli to only three: the modulus for

isotropic compression c_{11}, the shear modulus c_{66} (both connected with the mutual repulsion of FLs) and the tilt modulus c_{44} (connected with the line tension).

When flux lines move inside a superconductor electric fields are induced in a direction normal to their movement and the magnetic field direction. Averaged over several flux lines Josephson (1965) found the important expression for the electric field

$$\mathbf{E} = \mathbf{B} \times \mathbf{v} \tag{2.21}$$

where **B** is the local magnetic field and **v** the FL velocity, both averaged over several flux lines. Together with the driving current **J** this leads to energy dissipation at a rate $P = \mathbf{E} \cdot \mathbf{J}$, to which two effects are contributing about equally: The first comes from normal electrons which are accelerated by the electric fields generated close to the core of a FL. These electrons are scattered by the crystal lattice and their kinetic energy is dissipated. The second effect comes from a relaxation process of the moving disturbance of the order parameter. Cooper pairs are broken at the front of a moving core but not all the energy can be recovered by the reformation of the pairs at the back of the core. Bardeen and Stephen (1965) developed a simple model for 'flux flow', the continuous movement of flux lines. They assumed a viscous drag coefficient η such that the viscous force per unit length on a vortex line moving with velocity $\mathbf{v}_L$ is $-\eta\mathbf{v}_L$. Considering the dissipative effects mentioned above they calculated

$$\eta = \frac{\Phi_0 B_{c2}}{\rho_n} \tag{2.22}$$

where ρ_n is the normal state resistivity. In the steady flux flow state the net force on flux lines is balanced: $\mathbf{f}_L + (-\eta\mathbf{v}_L) = 0$. Combining this expression with Equs. (2.20), (2.21) and (2.22) results in the simple expression for the flux flow resistivity

$$\rho_f = \frac{E}{J} = \rho_n \frac{B}{B_{c2}}. \tag{2.23}$$

It is smoothly connected to ρ_n at $B = B_{c2}$ which is expected for this second order phase transition.

To prevent flux lines from moving and hence dissipation, it is essential that the Lorentz force on FLs is balanced by other forces. Only then transport supercurrents are possible.

Fortunately such forces are provided by the interaction of flux lines with defects and inhomogeneities in the crystal structure. These forces are called pinning forces and the FL-defect interaction itself pinning. Current densities up to the critical current density J_c are possible, at which point the Lorentz force exceeds the pinning forces and flux lines start to move.

2.5 Flux line pinning

The study of pinning is central (practically equivalent) to the study of critical currents in type-II superconductors. In this section different aspects of pinning in the anisotropic HTS are discussed, namely the interaction of individual defects with one flux line, the statistical methods of adding these pinning forces to an average pinning force density and, finally, a brief overview of the macroscopic effects of pinning.

2.5.1 Elementary pinning forces

Flux lines interact with defects in the underlying crystal lattice in two possible ways: First, a flux line core that passes through a defect with already suppressed order parameter reduces the overall condensation energy less than a core passing the defect. This effect is called core pinning and the resulting pinning force is strongest if $|\psi|$ drops to zero over a length ξ at the edge of the defect. For a large volume pinning force a high density of sharp superconductor-defect interfaces is required, which is usually achieved with defect dimensions of about ξ. The second FL-defect interaction results from a dependence of the shielding current energy and the magnetic energy on the position of the flux line. This is a purely electromagnetic interaction. An example is an isolated vortex, which passes through a defect of size 2λ. Relative to a flux line not interacting with any defects, in this case a smaller shielding current flows around the defect with a much reduced kinetic energy. Similarly the flux quantum is spread over a larger area resulting in a reduced magnetic field and smaller field energy. This second type of pinning is called magnetic or diamagnetic pinning. In the HTS it is much less important than core pinning, because over a wide temperature and field region (B_{c1} is small) the shielding currents of several vortices overlap, such that average current densities are small and the magnetic field nearly uniform.

Conceptually pinning is introduced into the system by taking into account that the para-

meters α, β and m_j in Equ. (2.8) can vary locally. When deriving Equ. (2.8) from the microscopic BCS theory (Campbell and Evetts, 1972; Evetts, 1992, p 164; de Gennes, 1966, p 171) it is possible to relate this local change of the parameters to variations of the fundamental materials parameters T_c and ℓ (the mean free electron path). These two types of core pinning are therefore called δT_c and $\delta\ell$ pinning. In principle the two types can be distinguished by different temperature and field dependencies.

A single flux line can interact with different classes of defects. The most widely studied sources of pinning are point defects, which are smaller than ξ in each dimension. Here the saved condensation energy is simply proportional to the defect volume and the pinning force is the saved energy divided by ξ, the relevant interaction length (This is slightly simplistic, but gives results of the right order of magnitude, if the defects are not too small. Very small defects are proximitised, which means that the order parameter is not significantly reduced at the defect location, although the defect material is not superconducting.) It is important to note that in anisotropic materials this results in pinning forces which depend on the direction of the force, since ξ varies with ϑ. A very simple assessment, assuming a given spherical defect, thus leads to a pinning force proportional to $1/\varepsilon_\vartheta$ in y'-direction, if a FL is tilted by an angle ϑ (see Fig. 2.5). The force in x'-direction on the other hand should be independent of ϑ.

More complex defects acting as pinning centres have larger dimensions in one (line pins) or two dimensions (pinning planes). In HTS line pins can be formed by screw dislocations, pinning planes by stacking faults, twin planes and, importantly, the weakly conducting layers separating CuO_2 double layers. The last effect is often referred to as intrinsic pinning because even a perfect single crystal contains this source of pinning.

In addition to these more or less naturally occurring defects much effort has been made to introduce additional pinning sites, both to improve the understanding of pinning in experiments as well as to improve the critical current density for applications. In bulk samples pinning has been substantially improved by the inclusion of off-stoichiometric second phases (Murakami *et al*., 1989) and in thin films strong changes of the pinning behaviour have been achieved by irradiation with various particles, most notably high energy heavy ions (see chapter 6). The latter introduce linear defects along their nearly ballistic trajectories, which extend laterally over lengths comparable to ξ.

Extended defects exert different pinning forces on flux lines depending on their relative orientation, as well as on the direction of the pinning force. More specifically, a line defect exerts a maximum pinning force in all directions if the flux line is aligned with the defect. The pinning forces can be substantial in this case because the full condensation energy of a flux line can be saved. If the flux lines are not parallel to the line defects, overall pinning is much smaller. A flux line aligned with a pinning plane either experiences a strong pinning force normal to the plane or a small force parallel to the plane, since FL movement in the plane does not affect the condensation energy of the system.

This listing of possible flux line-defect interactions – certainly not complete – shows that there are many different elementary pinning interactions and that it is not possible to find one generally applicable formula for f_p, the basic pinning force. For a given material the main defect structure should first be determined and then the pinning energy estimated. Many parameters must be considered, like the defect morphology, the pinning mechanism, magnetic field orientation and field strength. Reasonable estimates can now be made for the most important pinning centres in the LTS, but the situation is not so clear in the HTS yet.

2.5.2 The summation of pinning forces

So far interactions involving only one defect have been considered. A correct summation of all elementary pinning forces to obtain an effective pinning force density F_p is however essential but not trivial. Labusch (1969) first pointed out that a random force distribution on a perfectly regular and rigid flux line lattice averages to zero. The real FLL is however not rigid but adapts elastically to the random pinning field in such a way as to reduce the total free energy of the system. Thereby the elastic energy of the FLL increases, but this is more than offset by a lowering of the pinning energy.

2.5.2.1 Collective pinning theory

For the case of weak point pins, where the FLL is only slightly and elastically deformed, Larkin and Ovchinnikov (1979) were able to solve the summation problem with their theory of collective pinning. The key observation within this theory is that although local flux line displacements are only small, they can accumulate over longer distances

and thereby destroy the long range order of the FLL. The distances over which the pinning induced accumulated displacements become comparable to the elementary pinning interaction length (~ξ), are L_c and R_c, the longitudinal (parallel to the field) and transversal collective pinning lengths. Within the collective pinning volume $V_c = L_c R_c^2$ the elastic forces dominate, effectively forming a bundle of rigid flux lines, but between neighbouring pinning volumes the pinning motivated shear and tilt distortions are on a relevant scale. L_c, R_c, V_c and the pinning energy can be obtained from the net free-energy change per unit volume induced by pinning:

$$\Delta F = \frac{1}{2} c_{66} \left(\frac{\xi}{R_c} \right)^2 + \frac{1}{2} c_{44} \left(\frac{\xi}{L_c} \right)^2 - f_p \xi \frac{N^{1/2}}{V_c} \tag{2.24}$$

The first two terms in Equ (2.24) describe the increase in elastic energy for shear and tilt distortions respectively whereas the third term reflects the energy reduction gained by accommodating the pinning sites. Here f_p is the elementary pinning force, ξ the relevant interaction length and N the number of pins in the collective pinning volume. The factor $N^{1/2} = (nV_c)^{1/2}$ reflects the fact that the elementary pinning forces only add up in a random walk like manner (n is the pinning centre density). Although this is a rather schematic expression (Tinkham, 1996, p 351), minimising ΔF leads to

$$L_c = \frac{2 c_{44} c_{66} \xi^2}{n f_p^2} \qquad R_c = \frac{\left(2 c_{44} c_{66}^3\right)^{1/2} \xi^2}{n f_p^2} \qquad V_c = \frac{4 c_{44}^2 c_{66}^4 \xi^6}{n^3 f_p^6}, \tag{2.25}$$

confirming the expectation that V_c decreases (and hence the FLL becomes more distorted), if there are more and/or stronger pinning sites and if the elastic moduli decrease. Inserting the result (2.25) into Equ (2.24) gives the magnitude of the net pinning energy per collective pinning volume and for the pinning force density, which is balanced at J_c with the Lorentz force density, one obtains

$$J_c B = F_L = F_p = \frac{n^2 f_p^4}{2 c_{44} c_{66}^2 \xi^3}, \qquad J_c B = \left(\frac{n f_p^2}{V_c} \right)^{1/2}. \tag{2.26}$$

In the range of applicability of the collective pinning theory this result shows that F_p is stronger for softer flux line lattices, because the lattice can better adapt to the randomly distributed pinning centres. If the lattice however becomes very soft (like close to B_{c2} in

LTS or close to the irreversibility line in HTS), then each defect effectively defines its own collective pinning volume ($nV_c \approx 1$) and all elementary defects just add up ($F_p = nf_p$) giving a much stronger F_p than the random walk like summation. This effect is one possible explanation of the 'peak effect' observed in many hard LTS materials, where a pronounced maximum appears in $F_p(B)$ close to B_{c2}.

2.5.2.2 Two dimensional collective pinning

In thin films or in crystals consisting of decoupled layers the longitudinal correlation length L_c is replaced by the film or layer thickness d, if the field is applied normal to the layers. In this case the c_{44} term in Equ (2.24) is omitted and $V_c = R_c^2 d$. F_p and the critical current density are given by

$$J_c B = F_L = F_p = \frac{n f_p^2}{c_{66} \xi d}, \tag{2.27}$$

which shows a weaker dependence on all parameters than Equ (2.26).

An important limitation of the collective pinning theory is that it only takes elastic deformations of the FLL into account although experiments have shown that dislocations and other defects in the FLL are very common. When a model is constructed taking defects in the FLL into account, qualitatively similar results are obtained showing that it is not straight forward to calculate L_c and R_c. The validity of the idea of a collective pinning volume with random walk-like summation of the pinning forces inside, however, remains and the right hand formulation of Equ (2.26) can be used to determine V_c from experiment.

Apart from the pinning by randomly distributed weak pinning centres, for which there is a general consensus on the principal validity of the collective pinning theory, a number of correlated pinning centres are present in the HTS, often dominating the pinning behaviour. Examples of these centres are the extended defects described above (section 2.5.1). Theories for these types of pinning are complicated by the necessity to take the direction of both the magnetic field and the extended defect relative to the crystal axes into account. One fairly successful model, the boson glass model will be described further below (2.6.3) because it is closely linked to the prominent thermal effects in the HTS (see section 2.6).

2.5.3 Macroscopic effects of pinning

Pinning has two main macroscopic manifestations, both desired and technologically important: firstly the magnetisation curve of a type II sample with pinning becomes irreversible and secondly they are able to carry transport supercurrents which do not only flow in a thin surface layer.

These two effects are linked by the Bean critical state model (Bean, 1962), which describes the entering of magnetic flux into a sample. It may be described by considering a zero-field-cooled sample in an increasing applied field. Below H_{c1} the penetration of field into the sample is prevented by shielding currents in a surface layer, similar to type I superconductors. When the applied field exceeds H_{c1}, flux lines nucleate at the surface and start to move to the interior of the sample, but the establishment of the thermodynamic equilibrium configuration is prevented by pinning and a field gradient appears. This field gradient is associated with a current density J. Beans observation was that the flux lines only move if J exceeds J_c, since only then the local pinning force is exceeded by the Lorentz force, and a new field distribution can be realised. This behaviour can be nicely visualised by a sand pile to which sand is added at the top: the base of the sand pile only broadens if the slope of the pile exceeds a critical slope. Then the sand can flow all the way to the base (Campbell and Evetts, 1972). In the superconducting sample the force balance equation

$$|\mathbf{B} \times (\nabla \times \mathbf{H})| = B J_c(B) \tag{2.28}$$

is known as the critical state equation and its solutions determine the distribution of flux, current and magnetisation in a sample. This situation of selforganised criticality clearly shows how the magnetisation of a strong pinning type II sample becomes history dependent and therefore irreversible. For small fields $J_c(B)$ is often assumed constant, but close to B_{c2} (or the irreversibility line in HTS) the field dependence has to be considered. Magnetisation measurements of type II samples have been extensively used to determine J_c using the Bean critical state model although a number of pitfalls have to be carefully considered (surface pinning effects, effects of the sample geometry etc.).

The direct method to determine J_c, namely with an applied transport current, has the advantage of investigating arbitrary field and current configurations, not only with field

and current perpendicular. Generally the relation $-\mathbf{F}_p = \mathbf{F}_L = \mathbf{J}_c \times \mathbf{B}$ still holds, but for $\mathbf{J} \parallel \mathbf{B}$, the so called force free configuration, this expression would lead to an infinite J_c, which is clearly not physical. In reality instabilities lead to spiral deformations of the flux lines and to flux cutting and cross joining effects (Cave and Evetts, 1978; for a nice overview see Evetts, 1992, p 612). The unusual effect of increasing J_c with increasing B in thin PbTl films was observed by Blamire *et al*. (1986).

For applications the knowledge of the full functional dependence of J_c on B and T for a given material is often desirable. It is of course possible to measure $J_c(B)$ for all relevant temperatures, but this can be a lengthy process. For conventional (LTS) hard superconductors, which are used in most engineering applications, Kramer (1973) found a so called 'scaling law', with which it is possible to derive the B dependence of J_c at all temperatures by measuring it at only one T. By starting with a FLL shear model, he showed that most experimental data could be described by the factorised expression $F_p = B_{c2}^m(T)\, f_p(b)$, where all the temperature dependence is contained in the first factor and $f_p(b)$ describes the field dependence ($b = B/B_{c2}$). For A15 materials he found a general expression for $f_p(b)$ close to B_{c2} (i.e. $b \lesssim 1$): $f_p(b) \propto b^{1/2}(1-b)^2$. This equation is often used in plots of $J_c^{1/2}B^{1/4} = F_p^{1/2}B^{-1/4}$ versus B, which are straight lines with negative slope, to determine B_{c2}. In other low T_c materials (NbTi, PbBi) F_p behaves linearly in the vicinity of B_{c2}.

The idea of 'scaling' may be described in the following way: try to find a transformation of the independent and/or dependent variable in parameterised plots such that the curves coincide. In Kramer's original paper (1973), for example, the independent variable B is *rescaled* by dividing with $B_{c2}(T)$, which is dependent on the free parameter T, and the dependent variable F_p is *rescaled* by dividing with F_p^{max}, the peak force in a $F_p(B)$ plot. Often more elaborate transformations than the simple rescaling are used, like the above reformulation of Kramer's plot shows ($F_p^{1/2}B^{-1/4}$ versus B).

The absence of scaling can also give some insight into the flux pinning properties of a material. Geometric matching effects between flux line and defect spacing for example are in contradiction with scaling. Campbell and Evetts (1972) pointed out that thermally activated flux motion should also destroy scaling behaviour. Since thermally activated processes play an important role in the HTS (see below), pinning force scaling models

along Kramer's arguments are not very successful, as described in detail by Niel (1992). This means that it is difficult to relate pinning effects at different temperatures because of thermal activation. It is however possible to relate pinning observations at different fields and orientation of applied field at the *same* temperature or in rather narrow temperature regimes. Many authors have described possible angular scaling models, which are described in detail in chapter 4. These models play a central part in the interpretation of the experimental data in this thesis.

2.6 Thermal activation of flux lines

Even when the pinning force is stronger than the Lorentz force originating from a transport current J, thermal fluctuations can lead to diffusive motion of flux lines in Lorentz force direction. Thus the vortex state under applied currents is thermodynamically only metastable. Anderson and Kim (1962; 1964) developed a theory for flux creep, as they called this phenomenon, to explain the observation of a decaying magnetic moment of a type II sample in the mixed state (Kim *et al*., 1962; Kim *et al*., 1963).

2.6.1 The Anderson-Kim flux creep model

Their essential idea was that flux lines or bundles of flux lines can jump form one pinned configuration to an adjacent one by overcoming the intermediate energy barrier by thermal activation. They assumed an effective jump rate of the usual form $R = \omega_o e^{-U/kT}$ where ω_0 is a characteristic vibration frequency of the flux lines and U the activation energy to overcome. The latter generally depends on B, T and J. Anderson and Kim assumed the form $U = U_0(1 \pm J/J_c)$, which is the simplest possible and corresponds to a sawtooth shaped pinning potential tilted by the applied current (Fig. 2.6a). Here the plus is for flux jumps against the Lorentz force and the minus for jumps in Lorentz force direction, where the activation energy disappears at $J = J_c$. The disappearing of U can be used as a definition for J_c. The rate for jumps in Lorentz force direction minus the rate in opposite direction gives

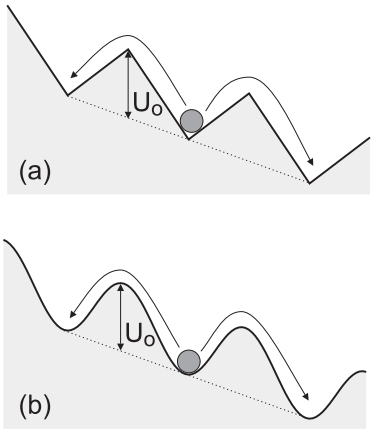

Figure 2.6
Tilted sawtooth (a) and cosine (b) pinning potential with flux line.

the net jump rate

$$R = R^+ - R^- = \omega_0 \exp\frac{-U_0}{kT}\left(\exp\frac{U_0}{kT}\frac{J}{J_c} - \exp\frac{-U_0}{kT}\frac{J}{J_c}\right) = \omega_0 \exp\frac{-U_0}{kT}\sinh\frac{U_0}{kT}\frac{J}{J_c} \quad (2.29)$$

In conventional superconductors U_0/k is of the order of 1000 K, resulting in unmeasurably small creep rates at typical LTS temperatures, except for J very close to J_c. In this case the sinh in Equ. (2.29) can be replaced by exp, simplifying the expression, but it remains highly non linear leading to difficult to solve differential equations for the general case. With the assumption that the Lorentz force is proportional to the remaining flux in a thin-walled magnetised cylinder, it can be shown (Tinkham, 1996, p. 183) that the time dependence of the magnetisation is logarithmic:

$$M(t_2) = M(t_1)\left(1 - \frac{kT}{U}\ln\frac{t_2}{t_1}\right) \quad (2.30)$$

There is the same amount of creep between 1 and 10 seconds as between 1 and 10 days. This unusual time dependence has been observed in many LTS samples in principle, although various adaptations to the original, rather unphysical, sawtooth-shape of the pinning potential have been made, resulting in $U = U_0(1 - J/J_c)^n$. The power n depends on the specific shape of the potential. For a tilted cosine, for example, $n = 3/2$. Different values of n only influence $U(J)$ in the vicinity of J_c, whereas U is always close to U_0 and independent of J for $J \ll J_c$. This reflects the fact that adaptations of models for the LTS are only necessary for J close to J_c, because U is typically *much* larger than kT and flux creep irrelevant for smaller J.

In the HTS U tends to be smaller than in the LTS and involved temperatures an order of magnitude larger because of the higher T_c. This has dramatic consequences for thermal activation effects since they depend exponentially on U/kT. For an activation energy of $U/k = 300$ K and an attempt frequency ω_0 of 10^8 Hz for example, $\omega_0 e^{-U/kT}$ is 2×10^6 Hz at 77 K but only 10^{-23} Hz at 4.2 K (see diamonds in Fig. 2.7). Thus relaxation processes which take 10^{15} years in liquid Helium occur in a microsecond at typical HTS temperatures. Fig. 2.7 shows typical values of activation energies as a function of temperature for Bi-2212 and YBCO. It can be seen that over a large temperature range thermal activation is strongly pronounced.

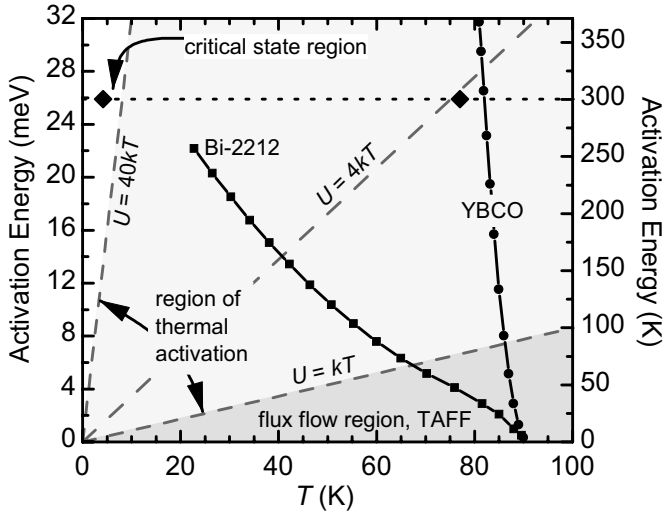

Figure 2.7
Schematic diagram of typical activation energies as a function of T in HTS. For Bi-2212 the activation energies are small even far below T_c, leading to extreme flux creep. But also YBCO with stronger pinning is in a regime of thermal activation in a considerable temperature range below T_c.
(Diagram originally by J.E.Evetts.)

2.6.2 The vortex glass model

Since after a sudden adjustment of current or external field the first few decades of decay can be very short, experimental observations in the HTS are often made at current densities much smaller than J_c, requiring a more careful analysis of the current dependence of U than in the simple Anderson-Kim model. For collective pinning by many weak pinning sites $U \approx U_0(J_c/J)^{\mu}$ with $\mu > 0$ (collective creep in a vortex glass; Feigel'man *et al*., 1989), leading to a divergence of U as J approaches 0. Thus close to $J = 0$ any *linear* resistance disappears in contrast to the Anderson Kim model where there is always a linear resistance, even if it is exponentially small. This sub-linear response evoked the terms 'glassy behaviour' and 'vortex glass'. There are however other models to explain the pinning behaviour in HTS, all in principle predicting different shapes of $U(J)$.

Berghuis *et al*. (1996) analysed the I–V response of YBCO thin films, of the same kind as used for the experiments described in this thesis, in detail and compared the obtained data to $U(J)$ functions predicted by a number of pinning models at 77 K. The function which proved to describe the data best is an interpolation formula between the vortex glass behaviour at low currents and the Anderson-Kim descriptions for $J \lesssim J_c$ (Feigel'man *et al*., 1989; Feigel'man *et al*., 1991; Wen *et al*., 1995):

$$U(J) = \frac{U_c}{\mu}\left(\left(\frac{J_c}{J}\right)^{\mu} - 1\right) \tag{2.31}$$

However, the parameter μ, which should be constant and characteristic of a specific pinning model (collective-creep model, Bose glass model), changes with magnetic field. At low fields where J_c and U_c are field independent the experiments suggest the

existence of a Bose glass phase (see below).

The important effect of giant flux creep on J_c measurements in the HTS is that the first appearance of a voltage with increasing current can be substantially below the true J_c, which is defined by the current density for which $U(J)$ goes to zero. This is fundamentally different to the LTS, where flux creep occurs only very close to J_c and J–E curves have a sharp upturn at J_c making the determination of J_c rather independent of a voltage criterion.

Griessen *et al*. (1994) conducted sensitive torque magnetometer measurements on YBCO thin films and calculated the induced current under the condition of an external field swept with a constant rate. Using a generalised inversion scheme (Schnack *et al*., 1993), they could also find an estimate for the true critical current density J_c, where $U = 0$. Fig. 2.8 shows both current densities as a function of temperature. It can be seen that even at temperatures as low as 20 K there is a factor of two between J_s and J_c in this estimate. At higher temperatures the ratio increases further.

2.6.3 The boson glass model

For the important case that correlated disorder (line defects or pinning planes) dominate the pinning behaviour in a sample instead of random point pins, Fisher *et al*. (1989) and Nelson and Vinokur (1992) developed the so called boson glass model.

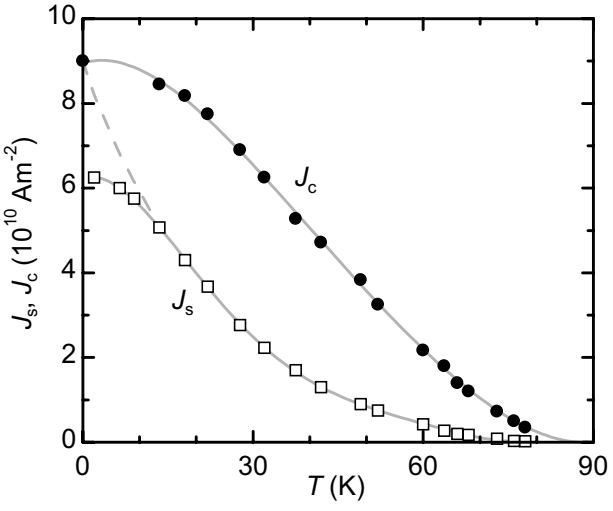

Figure 2.8
Induced current density J_s and true critical current density J_c determined from torque magnetisation measurements. The dashed line indicates the assumed behaviour without the presence of quantum creep.
(Fig. 2 from Griessen *et al*. (1994))

For fields aligned parallel to line defects and smaller than the matching field, where the average vortex spacing equals the line defect spacing, all vortices are localised at a defect. In this case it is possible to formulate a free energy func-

tional of the system with N fluxons where each term depends on the parameter z, the coordinate along the field direction. This free energy functional is *formally* equivivalent to the functional describing N two dimensional bosons in a random static potential if the parameter z is replaced by the time t. With standard quantum mechanical methods it is possible to solve this problem in a tight-binding approximation.

The bose glass model also predicts a current dependence of the pinning potential of the form of Equ. (2.31), but with the definite values of $\mu = 1/3$ at low currents and $\mu = 1$ at higher currents. As a reflection of the orientational character of the pinnig centres, the model also predicts an angular dependence of the irreversibility line.

2.6.4 Thermal activation without pinning

This section so far concentrated on flux creep in systems with strong disorder and hence pinning, appropriate for the thin YBCO films investigated in this thesis. However recent experiments on single crystals, which contain very few pinning centres, seem to indicate that thermal activation can lead to a first order melting of the flux line lattice (Zeldov *et al*., 1995). For a long time there were doubts whether this effect exists. It was difficult to observe because the latent heat involved is extremely small and in samples with pinning the effect is smeared out, since the flux line lattice is already disordered.

Thermal activation effects are prominent in HTS and it is often not easy to take them into account. For this thesis the most important aspect is that current densities close to the onset of dissipation can be substantially smaller than the true critical current density J_c, which is defined by $U(J_c) = 0$.

2.7 The layered structure of HTS

All HTS consist of one or several CuO_2 layers per unit cell, where superconductivity resides, and spacing layers composed of other elements, which are not superconducting (see section 2.1). Close to T_c the coherence length in c-direction ξ_c is longer than the spacing d of the CuO_2 layers and a description of the flux structure using the anisotropic GL-theory is adequate. At lower temperatures, however, ξ_c becomes smaller than d and it is necessary to take the layered structure explicitly into account. This is usually done by applying a model proposed by Lawrence and Doniach (1970) in which the GL free energy is modified to describe a stack of coupled two dimensional superconducting

planes (with the magnetic terms omitted at the moment for simplicity):

$$G = \sum_n \int \alpha|\psi_n|^2 + \frac{1}{2}\beta|\psi_n|^4 + \frac{\hbar^2}{2m_{ab}}\left(\left|\frac{\partial\psi_n}{\partial x}\right|^2 + \left|\frac{\partial\psi_n}{\partial y}\right|^2\right) + \frac{\hbar^2}{2m_c d^2}|\psi_n - \psi_{n-1}|^2 \qquad (2.32)$$

Here the sum runs over the layers and the integral is over the area of each layer. The last term is the finite difference between the order parameters in adjacent layers and corresponds to the z-derivative in a continuous system. It can be seen that Equ. (2.32) reduces to the anisotropic GL-free energy (Equ. (2.8)) if the variation of ψ along the c-axis is smooth enough such that $(\psi_n - \psi_{n-1})/d$ can be replaced by $\partial\psi/\partial z$.

2.7.1 Vortex structure in layered superconductors

In a layered superconductor, the structure of individual vortices as well as that of the vortex lattice can be substantially different from an anisotropic but homogenous material. In the 2D limit it is often appropriate to consider a tilted flux line to be composed of a sequence of pancake vortices parallel to the c-axis and Josephson vortices parallel to the ab-plane (Clem, 1991).

The core of a Josephson vortex is located between two superconducting layers with high density screening currents flowing in the layers and lower density currents crossing between adjacent layers (see Fig. 2.9). These currents extend over distances λ_c and $\lambda_{ab} = \varepsilon\lambda_c$ parallel and normal to the ab-plane respectively, which are the same values as for an Abrikosov vortex in an anisotropic material, showing that the two types of vortices are roughly equivalent on this magnetic length scale. However, within the distances $\Lambda = d/\varepsilon$ (along the ab-plane) and d (along the c-axis) the discreteness of Equ. (2.32) becomes relevant, which results in a changed core structure in comparison to an Abrikosov vortex. One reason for this change is a reduced maximum current density in c-direction $J_J = J_0\xi_c/d$, where J_0 is the depairing current density. The second reason is that the order parameter in the layers adjacent to the Josephson vortex is only weakly suppressed, as can be shown by perturbative methods (Blatter and Geshkenbein, 1993). Thus, in

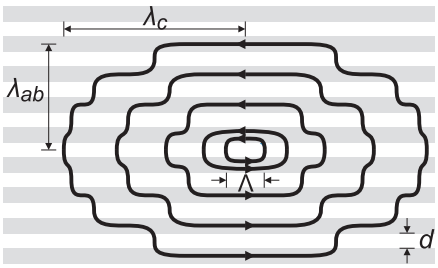

Figure 2.9
Current distribution around a Josephson vortex in a layered superconductor

contrast to the Abrikosov vortex, where large current flow near the core leads to complete suppression of the order parameter, there is only weak suppression in the superconducting layers when a Josephson vortex is present. The different core structure also leads to a slightly different line energy and line tension with different temperature dependencies of the two types of vortices (Blatter *et al*., 1994, p 1281).

Pancake vortices, the second building block of tilted flux lines in layered superconductors, consist of a regular core and screening currents in one layer, with the magnetic field parallel to the *c*-axis. The term was introduced by Clem (1991), who described the magnetic field, current distribution and interaction of pancake vortices in detail. For simplicity Clem studied the case of only magnetically coupled layers (no currents in *c*-direction) and found that a flux line built of a stack of pancake vortices can evaporate into free moving pancakes at a temperature T_e. This effect is closely related to the unbinding of a vortex and an antivortex in the same layer at the Kosterlitz-Thouless (1973) transition temperature T_{KT}. In both cases the interaction energy depends only logarithmically on the distance R between the vortex and its equilibrium position in the stack or the vortex and the antivortex respectively.

If Josephson coupling between layers is taken into account, necessary for YBCO, a vortex-antivortex pair remains bound at all temperatures, since Josephson strings in the adjacent gaps hold them together. It is interesting to look at two particular double-kink configurations (Fig. 2.10). The first (a) is a vortex-antivortex pair connected to a Josephson string. Since a separation of the two pancake vortices does not change the length of the Josephson string, their interaction energy only depends logarithmically on R, as in the case with no Josephson coupling. This configuration represents the nucleus for flux-creep in *c*-direction. The second configuration (b) consists of two vortices in adjacent layers. This is the elementary building block of a tilted flux line. For both configurations the interaction energies have been calculated (Blatter *et al*., 1994, p 1285).

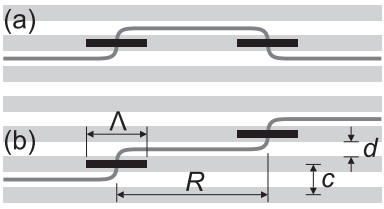

Figure 2.10
Kinked vortex configurations in a layered superconductor. a: Nucleus for flux movement in *c*-direction; b: basic element of a tilted vortex line. The bars indicate the extent of the core of pancake vortices.

Perhaps the most important influence of the layered structure on critical current densities in the HTS is the effect of intrinsic pinning, which describes the high

pinning energies generated by the intrinsic modulation of the order parameter, preventing the movement of Josephson strings in *c*-direction. The development of the ideas associated with intrinsic pinning and experiments supporting these ideas are described in detail in chapter 4.

2.8 References

Abrikosov, A.A., 1957, Zh. Eksp. Teor. Fiz. **32**, 1442.

Anderson, P.W., 1962, Phys. Rev. B **9** (7), 309-311.

Anderson, P.W. and Y.B. Kim, 1964, Reviews of ModernPhysics **January**, 39-43.

Bardeen, J. and M.J. Stephen, 1965, Phys. Rev. **140** (4A), A1197-A1207.

Bean, C.P., 1962, Phys. Rev. Lett. **8**, 250-3.

Bednorz, G. and K.A. Müller, 1986, Z. Phys. **B64**, 189.

Berghuis, P., R. Herzog, R.E. Somekh, J.E. Evetts, R.A. Doyle, F. Baudenbacher and A.M. Campbell, 1996, Physica C **256**, 13-32.

Blamire, M.G. and J.E. Evetts, 1986, Physical Review B **33** (7), 5131-5133.

Blatter, G., M.V. Feigel'man, V.B. Geshkenbein, A.I. Larkin and V.M. Vinokur, 1994, Reviews of Modern Physics **66** (4), 1125-1388.

Blatter, G. and V.B. Geshkenbein, 1993, Phys. Rev. B **47**, 2725.

Campbell, A.M. and J.E. Evetts, 1972, *Critical Currents in Superconductors*. London, Taylor & Francis Ltd.

Cave, J.R. and J.E. Evetts, 1978, Philos. Mag. **B 37**, 111-118.

Clem, J.R., 1991, Phys. Rev. B **43** (10), 7837-7846.

Clem, J.R., 1992, Superconductor Science & Technology **5**, S33-40.

de Gennes, P.G., 1966, *Superconductivity in Metals and Alloys*. New York, W. A. Benjamin.

Essmann, U. and H. Träuble, 1967, Phys. Lett. **A 24**, 526.

Evetts, J.E., Ed. (1992). *Concise encyclopedia of magnetic and superconducting materials.* Advances in materials science and engineering. Oxford, Pergamon Press.

Feigel'man, M.V., V.G. Geshkenbein, A.I. Larkin and V.M. Vinokur, 1989, Phys. Rev. Lett. **63**, 2303.

Feigel'man, M.V., V.G. Geshkenbein and V.M. Vinokur, 1991, Phys. Rev. B **43**, 6263.

Fisher, M.P.A., P.B. Weichman, G. Grinstein and D.S. Fisher, 1989, Phys. Rev. B **40**, 546.

Ginzburg, V.L. and L.D. Landau, 1950, Zh. Eksp. Teor. Fiz. **20**, 1064.

Griessen, R., Wen Hai-hu, A.J.J. van Dalen, B. Dam, J. Rector and H.G. Schnack, 1994, Phys. Rev. Lett. **72** (12), 1910-1913.

Hikami, S., T. Hirai and S. Kagoshima, 1987, Jpn. J. Appl. Phys **26**, L314.

Josephson, B.D., 1965, Physics Letters **16** (3), 242-243.

Kim, Y.B., C.F. Hempstead and A.R. Strnad, 1962, Physical Review B **9** (7), 306-309.

Kim, Y.B., C.F. Hempstead and A.R. Strnad, 1963, Physical Review **131** (6), 2486-2495.

Klemm, R.A. and J.R. Clem, 1980, Phys. Rev. B **21** (5), 1868-1875.

Kogan, V.L. and J.R. Clem, 1987, Jpn. J. Appl. Phys. **26** (Suppl 26-3), 1159.

Kosterlitz, J.M. and D.J. Thouless, 1973, Journal of Physics C **6**, 1181-1203.

Kramer, E.J., 1973, J. Appl. Phys. **44** (3), 1360-1370.

Labusch, R., 1969, Cryst. Lattice Defects **1**, 1–16.

Larkin, A.I. and Y.N. Ovchinnikov, 1979, J. Low Temp. Phys. **34**, 409-28.

Lawrence, W.E. and S. Doniach, 1970, 12th Int. Conf. on Low Temperature Physics, Kyoto, Keigaku, Tokyo 1970.

London, F. and H. London, 1935, Proc. Roy. Soc. **A149**, 71.

Meissner, W. and R. Ochsenfeld, 1933, Naturwissenschaften **21**, 787.

Murakami, M., M. Morita, K. Doe and K. Myamoto, 1989, Jpn. J. Appl. Phys. **28**, 1189.

Nelson, D.R. and V.M. Vinokur, 1992, Phys. Rev. Lett. **68**, 2398.

Niel, L., 1992, Cryogenics **32** (11), 975-978.

Ossandon, J.G., J.R. Thompson, J.K. Christen, B.C. Sales, H.R. Kerchner, J.O. Thompson, Y.R. Sun and J.E. Tkaczyk, 1992, Phys. Rev. B **45**, 12534.

Schnack, H.G., R. Griessen, J.G. Lensink and W. Hai-Hu, 1993, Phys. Rev. B **48** (17), 13178-13181.

Tinkham, M., 1996, *Introduction to Superconductivity*. New York, McGraw-Hill.

Wen, H.-H., H.G. Schnack, R. Griessen, B. Dam and J. Rector, 1995, Physica C **241**, 353-374.

Wu, M.K., J.R. Ashburn, C.T. Torng, P.H. Hor, R.L. Meng, L. Gao, Z.J. Huang, Y.Q. Wang and C.W. Chu, 1987, Phys. Rev. Lett. **58**, 908.

Zeldov, E., D. Majer, M. Konczykowski, V.B. Geshkenbein, V.M. Vinokur and H. Shtrikman, 1995, Nature **375**, 373-376.

Zhao, Z.X., L.Q. Chen, Q.S. Yang, Y.H. Huang, G.H. Chen, R.M. Tang, G.R. Liu, C.G. Cui, L. Chen, L.H. Wang, S.Q. Guo, S.L. Li and J.Q. Bi, 1987, Kexue Tongbao **32**, 661.

Chapter 3

Experimental Foundations

In this chapter a general description of the sample preparation and of the instrumentation used for the experiments in this thesis is presented. Thin films of YBCO were deposited in our research group, characterised by x-ray diffraction methods and AFM or STM. Subsequently a pattern was etched into the films to obtain test tracks with a well defined geometry, which is necessary for reproducible transport measurements. For these experiments a special probe was designed and crafted to enable the rotation of the thin film samples to any orientation relative to a magnetic field in a variable temperature insert of a liquid helium cryostat. Fields of up to 8 T can be applied in this system and the temperature accurately controlled in the large range between 3 and 300 K.

3.1 Sample preparation and characterisation

3.1.1 Deposition parameters and the microstructure of YBCO films.

Although the substrate temperature for YBCO deposition is high in comparison to metal and semiconductor sputtering (70 – 80 % of the melting temperature of YBCO), film deposition from the vapour phase is generally a non-equilibrium process where the kinetics of nucleation plays an important role. In addition to the elements from the target, the presence of an oxygen atmosphere has a strong influence on the kinetic environment: active oxygen can considerably support the formation of the correct phases.

The standard theories of single-crystal thin-film growth use a classification of growth modes which is based on the relative surface energies of the substrate and the deposit. There are three growth types: layer-by-layer growth, capillary growth where islands nucleate, grow and coalesce and an intermediate mechanism in which film growth starts layer-by-layer and then becomes island like. For YBCO there are a number of distinct deposition regimes with increasing temperature and oxygen partial pressure.

In a low pressure oxygen environment the depositing metals have a high mobility at a rather low temperature (630 – 700 °C). In this environment layer-by-layer growth has been observed (Terashima *et al*., 1990), although misfit dislocations start to appear at a

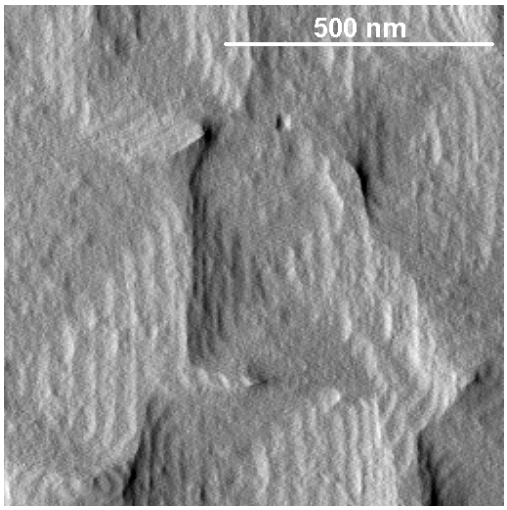

Figure 3.1
AFM image of a *c*-axis YBCO film with typical growth spirals.

critical thickness h_c, which depends on the substrate used. For the 1.2 % mismatch of $SrTiO_3$ (at 700 °C) h_c is about 10 nm. Because the diffusion rates are low in this temperature range, cation disorder is possible, particularly in films with wrong stoichiometry.

At slightly higher temperatures (but less than 740 °C) and increased oxygen pressure, island growth dominates on slightly mismatched substrates, but on vicinally cut $SrTiO_3$ and on the very well matched $NdGaO_3$ layer-by-layer growth is still observed (Miyazawa *et al*., 1992).

With even higher oxygen pressures the substrate temperature has to be increased to 740 – 760 °C because the metals arrive in an oxidised state at the substrate and are therefore less mobile. A characteristic feature of films grown in this regime are screw dislocations and growth spirals (see Fig. 3.1), which may have their origin in the underlying misfit dislocations threading through to the film surface. Screw dislocation growth is a characteristic growth mechanism for solids forming from the melt, which makes it not too surprising that they appear at this high temperature close to the melting point. The occurrence of outgrowths is also more likely at this elevated temperature since the metals are highly mobile on the film surface.

The substrate should ideally have the same lattice constant and the same thermal contraction as the film material to enable good epitaxial growth. It should be chemically stable and not react with the film, be cheap and available in large sizes. For microwave applications a low loss and low dielectric constant at high frequencies are desired.

$SrTiO_3$, the material used for many samples in this thesis, proved to be a reliable substrate for consistently producing high quality films, because it does not react with YBCO and its lattice constant is only about 1.2 % too large at 700 °C. Films deposited on $SrTiO_4$ between 750 – 830 °C grow with the *c*-axis normal to the surface (*c*-axis films), but at a 100 °C lower temperature the films grow mainly with the *a*-axis normal

to the surface (*a*-axis films). It is believed that the reason for this effect is the smaller size of the first nucleation centres for *a*-axis films. Since the quality of films is better at the higher deposition temperature used for *c*-axis film growth, a self template process was introduced. Here the first few unit cell layers are deposited at the lower temperature to seed the *a*-axis orientation, but then the temperature is increased by about 100 °C, where the film continues to grow as *a*-axis film because of the perfect epitaxy on the template layer. It is also possible to use $PrBa_2Cu_3O_{7-\delta}$ for the template layer to obtain an YBCO film of high quality over its entire thickness (Inam *et al*., 1991). The orientation of the *c*-axis within the plane of *a*-axis films is not uniquely defined since domains nucleate randomly with one of the possible two orthogonal orientations. Films with a well defined in plane *c*-axis orientation are often grown as (110) films on (110) $SrTiO_3$ substrates (see chapter 5).

Other materials on which YBCO films have been deposited with some success are MgO and yttrium stabilised zirconia (YSZ). The best lattice match at 700 °C can be found with the gallates $LaGaO_3$ (+0.4%), $NdGaO_3$ (−0.27%) and $PrGaO_3$ (−0.02%), but they are unfortunately expensive and only available in small sizes. Another approach has been the use of buffer layers to deposit YBCO on substrates like Al_2O_3, Si or GaAs which are desirable for their price, their microwave properties or their potential to integrate superconducting with semiconducting devices.

YBCO films with various orientations can now be produced with good epitaxy and consistently high quality. The typical mosaic spread in x-ray diffraction analysis of *c*-axis films is about 0.17° (see Fig 3.2). Extensive morphological studies (e.g. by Baudenbacher *et al*., 1991) show that very smooth films can be obtained if the stoichiometry and the epitaxy are exact. If the composition is slightly off stoichiometric various morphological features appear. For instance, if films are copper poor they tend to have a pitted surface, while if copper rich, precipitate particles are seen. Outgrowths with *a*-axis orientation often have an

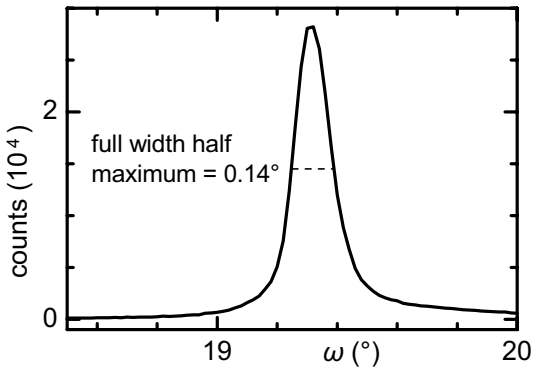

Figure 3.2
X-ray diffraction scan of a standard *c*-axis film (rocking curve). The mosaic spread of this peak is 0.14°. (Data courtesy L. Mechin)

elongated shape, because growth of crystallites within the *ab*-plane is much faster than in *c*-direction.

3.1.2 Film deposition by sputtering

All films measured for this thesis were deposited in our research group using a high pressure DC-sputtering technique (Poppe *et al*., 1988; Przyslupski *et al*., 1993; Somekh and Barber, 1992; Somekh, 1990). With this sputtering method substrates are placed approximately 12 mm from the fully stoichiometric target and heated to 700 – 800 °C, necessary for achieving adequate mobility of the depositing atoms. To prevent fast oxygen ions resputtering the already deposited film, the process is performed in a comparatively high pressure (~300 Pa) atmosphere of very pure oxygen (99.995%), which reduces the mean free path of the sputtered atoms to 0.1 – 0.2 mm. Under these conditions each atom experiences about 100 collisions before arriving at the substrate, which slow down the fast oxygen ions considerably ('thermalisation'), such that they do not have enough kinetic energy for resputtering any more. Another reason to use high pressure oxygen is the need to have oxidised metal atoms arriving at the substrate in order to grow high quality oxide films. With a target voltage between 200 and 250 V and a total power of ~40 W the deposition rate is approximately 1.5 nm/min. After the deposition of the film the oxygen pressure is increased to 100 kPa (ambient pressure) and the samples are annealed for about 10 minutes at 400 °C to achieve full oxygen stoichiometry in the films (i.e. $\delta \approx 0$ in $YBa_2Cu_3O_{7-\delta}$). This method is called an in-situ process because deposition and oxygenation of the films is conducted in the same system. It avoids sample contamination and does not need a re-crystallisation step at high temperature since the deposition directly generates the desired crystal structure (only the oxygenation at comparatively low temperatures is required). The thickness of the films used in this thesis lies between 170 and 220 nm. It was measured on each film with a needle profilometer and used to calculated J_c in the track.

3.1.3 Additional oxygen treatment

During the sputter deposition process described above the YBCO films are exposed to an oxygen atmosphere at 400 °C to achieve optimal stoichiometry with δ close to 0. However, oxygen was removed from some films by a heat treatment in vacuum to

investigate the influence of different degrees of oxygenation on the critical current. J_c of one or several tracks per sample (see patterning below) was measured before and after this deoxygenation procedure, which simply consisted of heating the films to 400 °C for 10 – 25 minutes in the same vacuum system the films were deposited in. The oxygen pressure in the system was lower than 0.3 Pa. Initial attempts to reduce the oxygen content of films in a small vacuum system and under argon flow destroyed the film because the environment was not clean enough. Only the ultra high vacuum systems used for deposition left the films intact, seen by nearly achieving the properties (T_c, J_c) of the original film after an additional re-oxygenation step. Re-oxygenation was again conducted in the same vacuum system by heating the films to 400 °C for 10 – 25 minutes in 100 kPa of pure oxygen.

3.1.4 Patterning of current tracks

In order to measure the critical current of thin films reliably, the geometry of the sample has to be accurately defined. This is usually done by etching a 4-point measurement track into the film using photolithographic methods. Because the critical current densities can be very high, the track is often made only a few tens of μm wide and as long as practically possible to improve the resolution of electric fields along the track. Another requirement for reliable experiments is the conduction of high currents (~1 A) into and out of the film with as little heat generation as possible, implying careful design of contacts to reduce their resistance. This section describes the steps followed to obtain fully patterned films ready for J_c measurements.

3.1.4.1 Evaporation of metal contacts

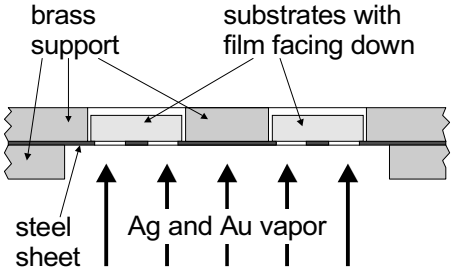

Figure 3.3
Mask used for evaporating metal contact pads onto new films. Holes are spark eroded through the steel sheet.

After film deposition, the first step in the patterning process is the evaporation of silver and gold contact pads onto the film. This is done in a commercial (Edwards) electron-beam evaporator through a special mask with spark-eroded holes (see Fig. 3.3). First a layer of silver is deposited and on top of it a thin gold layer. Initial tests to optimise this procedure showed that the samples should be

exposed to the metal plume and the hot electron target for as short a time as possible (~30 s) to avoid excessive heating and a change of oxygen content in this vacuum environment. For optimal contacts it is necessary to allow the silver to diffuse into the YBCO. This is achieved by heating the samples in pure oxygen to 400 °C for 20 minutes in the deposition system (similar to section 3.1.3). The reason for using an additional gold layer is that silver tends to form small droplets on the film during this diffusion step, whereas the forming Ag-Au alloy forms a smooth layer which is strongly bonded to the YBCO film.

3.1.4.2 Patterning

In the well equipped clean-room operated by our research group, 30 µm wide tracks were etched into the YBCO films to enable reliable 4-point electrical measurements. Up to four independent tracks could be placed on each 3 × 12 mm^2 substrate (see section 3.1.4.3 below).

Processing starts with the application of a droplet of photosensitive resist (Hoechst Microposit) to the sample, which is evenly spread to a thin layer by centrifugal forces using a spinner. The resist is hardened by putting the samples on a hot plate at 90 °C for about ten minutes. Subsequently the image of the pattern with the tracks (see Fig. 3.4) is projected onto the film with ultraviolet light in a commercial high resolution projector

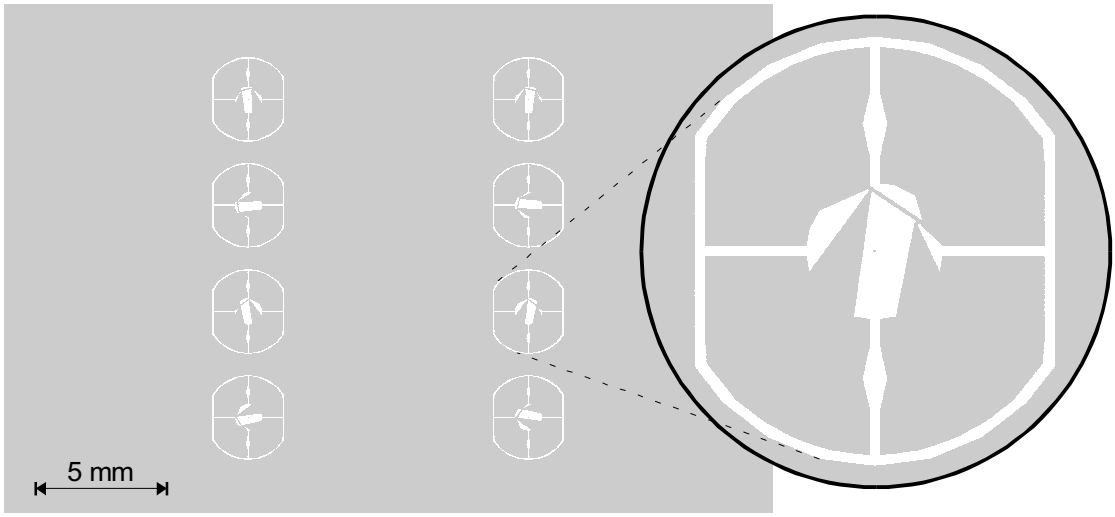

Figure 3.4
Mask for patterning current tracks in any direction in the film plane. The magnification clearly shows the 30 × 500 µm track running from top left to bottom right. The two upper areas are used as current contacts, whereas the two areas at the bottom are connected to voltage tabs.

(Canon). The resist reacts where it is exposed to the light and dissolves at these locations during the following dip into a developer solution. After visual inspection with a microscope the samples are ready for etching. If the pattern in the resist does not align satisfactorily with the contact pads or if the UV exposure was not correct, it is possible to remove the resist at this stage and start again.

In a 60 second dip in a nearly saturated solution of EDTA (Ethylene-diamene-tetraacetic acid) the pattern is transferred from the resist to the YBCO film. Initial trials with other etchants (strongly diluted phosphoric, nitric and hydrochloric acids) proved not practical, EDTA on the other hand is now widely used to etch YBCO (Shokoohi *et al*., 1989). It is nevertheless important to start with clean films, ideally very soon after deposition, to obtain sharp edges and no under-etch. A short rinse of the samples in acetone after etching removes the photo-resist and the sample is ready for electrical testing.

3.1.4.3 Mask layout

To enable the fabrication of current tracks in any direction within the film plane and to make maximal use of the 12×3 mm sample area, a special mask was designed (Fig. 3.4). Before patterning it is necessary to mark the desired direction on the film, preferably in an area between the contact pads where no track will be located. Under the microscope of the mask projector it is then always possible to align the mark and one of the eight patterns shown in such a way that the current track is parallel to the mark and the adjacent larger areas fit onto a set of gold-silver contact pads. Since each track has to be exposed separately, it is easy to swap the particular pattern and generate tracks with different orientations on the *same* film, as shown in Fig. 3.5. Here the two tracks on the left are aligned with the *b*-axis of an *a*-axis film, whereas the two other tracks are

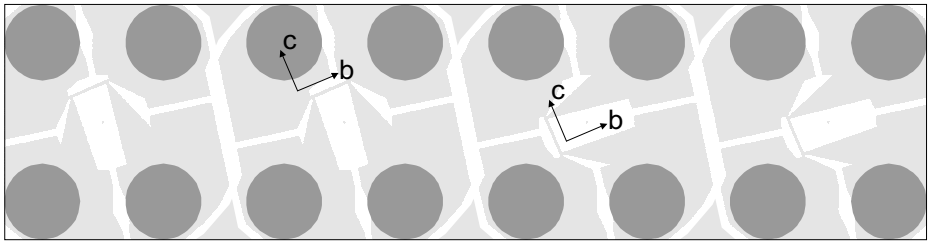

Figure 3.5
Fully patterned sample with four tracks patterned parallel to the crystal axes indicated by the arrows. The evaporated silver-gold contacts are shown by dark grey circles and the etched YBCO film by the light grey areas. Note how each track and its contact pads is insulated from the neighbours.

aligned with the *c*-axis. It can be seen how the full 360° are covered: Each individual pattern can be aligned with a set of contact pads and without interfering with neighbouring tracks within a range of ±14° from the straight direction. Since the track directions are offset by 22.5° from one pattern to the next, there is always a pattern available for any desired direction.

The design of this mask proved to be successful, although a lot of patience is required to operate the mask projector. A number of tracks have been etched into (110)-films in the described way, where the misalignment was less than 2°. When a 30 × 500 µm track is patterned parallel to the *ab*-planes, this accuracy is sufficient to ensure that at least some planes run from one end of the track to the other and not off at the side. A photograph of a patterned film is shown on colour plate 2 below.

3.1.4.4 Sample mounting

Spring loaded pins ('pogo pins') are used in many test and measurement applications for establishing a number of electrical contacts simultaneously in a reliable and quick way. In a cryogenic environment additional precautions have to be taken, because the small point contacts can open during cooling. To avoid this problem and to enlarge the cross section of the contact for larger currents (up to 1 A), indium disks are placed between the pins and the evaporated silver-gold contact area (see Fig 3.6). The fairly high pressure at the spherically shaped tip of the pin deforms the soft indium at room temperature establishing interfaces with large areas and low resistances between the Ag-Au contact pad and the indium as well as the indium and the pin. The sequence of layers and components shown in Fig. 3.6 provided a reliable method for conducting currents of up to 1 A into the YBCO films without any noticeable effect of heating in the contact resistances.

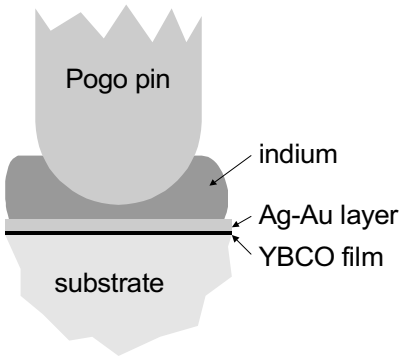

Figure 3.6
Pogo pin contact with indium disk.

3.1.5 Heavy ion irradiation

A small number of samples were irradiated with 2.6 GeV ^{197}Au ions at the Gesellschaft für Schwerionenforschung in Darmstadt. The irradiation time of several minutes was

chosen to obtain a fluence of $1.5 \cdot 10^{11}$ ions·cm^{-2}. This corresponds to a matching field B_Φ, where the flux line density equals the columnar defect density, of 3 T. To enable the irradiation at angles different from the normal to the film surface, a small copper carrier was machined as shown in Fig. 3.7. The substrates were simply glued onto the carrier with silver paste for good thermal coupling. Results of measurements on irradiated films are presented in chapter 6.

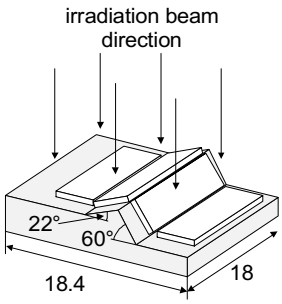

Figure 3.7
Sample carrier for heavy ion irradiation.

3.2 T_c measurement apparatus

For quickly measuring the critical temperature of up to four tracks on a 12 × 3 mm^2 substrate an existing probe was adapted and connected to a computer controlled data-acquisition system. Electrical contact to the Ag-Au pads on patterned films is established by 16 pogo pins (Fig. 3.8). With an external set of switches it is possible to transmit a constant current (~10 μA) through all tracks and monitor the track voltages with a scanning voltmeter. The sample is cooled by slowly lowering the probe into the cold gas above liquid helium in a standard He transport dewar. During cool-down the sample voltages and the thermometer readings are continuously transferred to the computer where the data is displayed and stored.

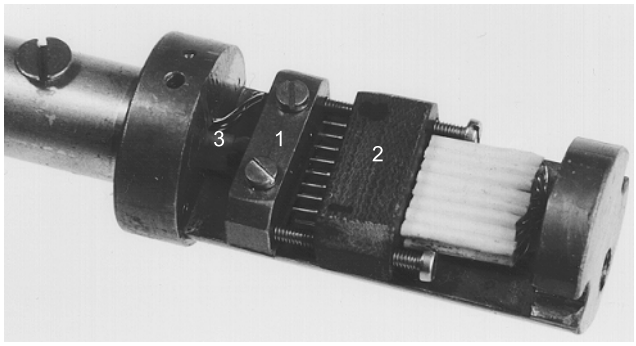

Figure 3.8
Sample mount of T_c probe. 1 – sample carrier with small hole for platinum T sensor, 2 – pogo pin carrier, 3 – connecting wires for T sensor. Due to their proximity T sensor and sample are thermally well coupled, which is necessary for accurate temperature readings.

Apart from fully patterned tracks it is also possible to measure T_c of unpatterned films with a particular combination of switch settings. In this case a current is applied using the outermost pins in the double row and the adjacent pins are used as voltage taps.

3.3 J_c measurement apparatus

The main aim of the experimental work for this PhD project was the investigation of the dependence of J_c in YBCO films on the angle of an applied magnetic field. Since the

number of independent parameters is large (two angles and the magnitude of the field plus temperature) and each covers a wide range, it was clear from the beginning that an automated measurement system with in situ rotation of the sample in the field would be necessary. Fortunately a second hand but unused and new cryostat with an 8 T superconducting solenoid and a variable temperature insert (VTI) could be acquired during the first month of this work at an advantageous price. To the author the 50 mm bore of the VTI appeared large in comparison to systems he had previously worked with, which prompted the contemplation of a two-axis goniometer rather than one with only one axis of rotation. Eventually this enhanced goniometer was built and integrated into a complete computer controlled data-acquisition system together with a number of commercial and custom built electronic instruments.

3.3.1 Two-axis goniometer

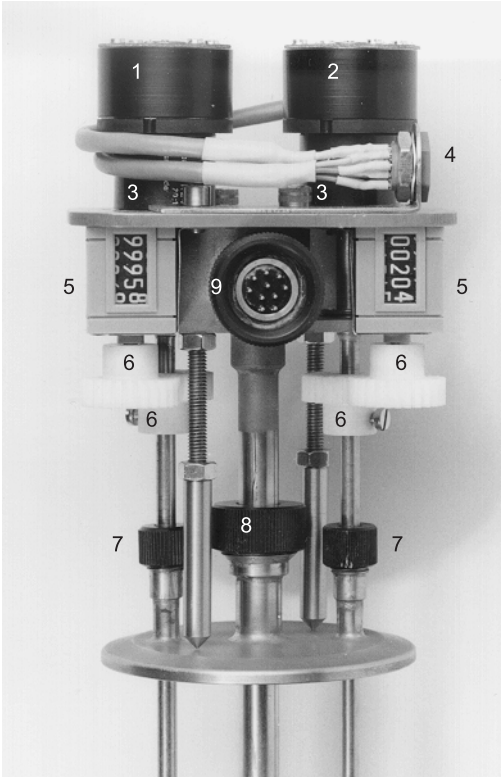

Figure 3.9
Top part of goniometer. 1 – stepper motor for ϑ rotation, 2 – motor for ϑ and φ rotation, 3 – 20:1 gear boxes, 4 – connector for stepper motor wires, 5 – mechanical counters, 6 – PTFE gears driving counters from drive shafts, 7 – O-ring sealed feedthroughs for the two drive shafts, 8 feed through for support tube, 9 – connector for *T* sensor and heater wires.

The goniometer consists of two functional units connected by stainless steel tubes (Herzog and Evetts, 1994). The top part (Fig. 3.9), operating outside the cryostat at room temperature, contains two stepper motors, sealed electrical connectors and vacuum feedthroughs for the steel tubes. To enhance the angular resolution and increase the force provided by the stepper motors, they are attached to small gearboxes with a reduction ratio of 20:1. The gearboxes drive the shafts 1 and 2 for ϑ and φ rotation. Both shafts pass through little flanges with O-rings, which seal the helium atmosphere in the VTI (see below). For unambiguous determination of the current angular positions of the goniometer the shafts rotate two mechanical counters via pairs of PTFE gears. One of the two O-ring sealed 10-pole connectors provides the connections for a

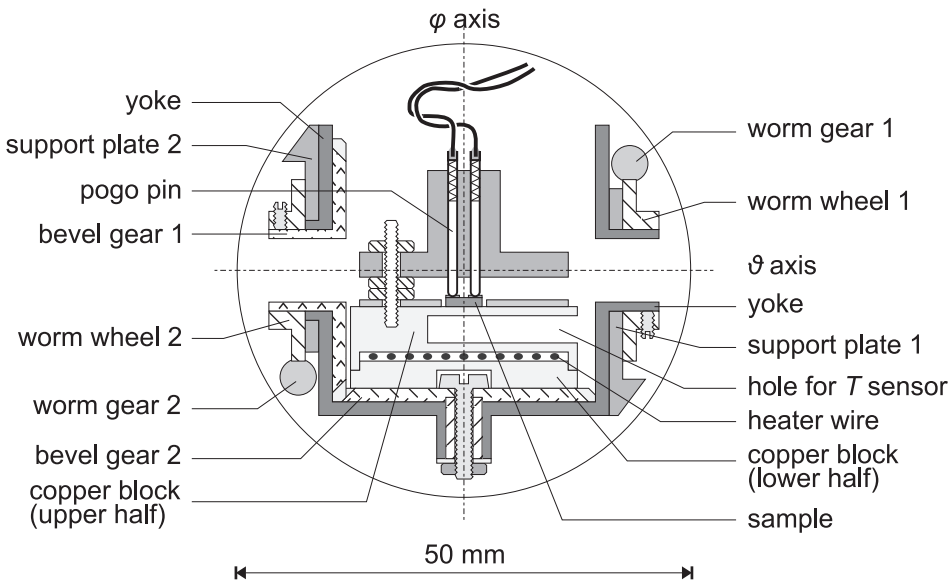

Figure 3.10
Cross section of two-axis goniometer with the yoke at the position $\vartheta = 0°$.

thermometer and heater wire, the other for the sample voltage and current. To reduce possible thermal voltages to a minimum solder joints at the backside of the connectors were made with a special low thermal, cadmium containing solder. In addition to providing a mechanical backbone the central support tube is used as a duct for all instrumentation wires.

The bottom part, which is lowered into the VTI to the centre of the solenoid at cryogenic temperatures, provides the temperature controlled rotating stage on which the samples are mounted (see colour plate 1). The function of the various gears can perhaps best be seen in Fig. 3.10. Worm gear 1, driven by shaft 1, engages with worm wheel 1, which is rigidly connected to the yoke. This sequence of gears is responsible for rotation around the ϑ axis. On the other side worm wheel 2 is connected to bevel gear 1, which engages with bevel gear 2 rotating the copper block (stage) with the sample around the φ axis. For a φ rotation at fixed angle ϑ it is only necessary to rotate drive shaft 2. For a ϑ rotation with constant φ on the other hand both drive shafts have to be rotated by the same amount but in opposite directions. Only then bevel gears 1 and 2 remain fixed relative to the yoke. The synchronous rotation of the two drive shafts is enabled by appropriate control of the two stepper motors. Most components are made of brass to ensure even thermal contraction. Only the worm wheels are of stainless steel on recommendation of the manufacturer who custom cut all gears to the required dimensions.

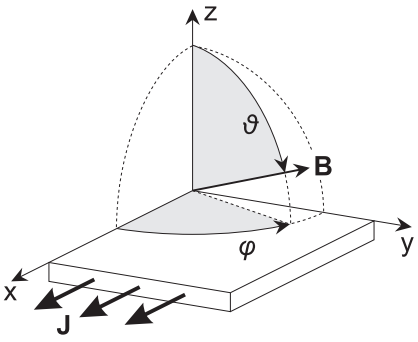

Figure 3.11
Definition of ϑ and φ relative to the current track. The angle between film normal and **B** is ϑ, the angle between the current direction and the projection of **B** into the film plane is φ.

Thin sleeves of PTFE line the slide bearings of all moving parts to reduce friction (These are not drawn in Fig. 3.10, but visible for the bearings of the worm gear in colour plate 1.) The precision of angular positioning in an angular scan is about 0.02°.

The 25 mm diameter copper cylinder on which the sample rests, consists of two parts glued together by Stycast resin. A twisted NiCr heater wire is embedded in the Stycast and a drilled hole in the copper block slightly closer to the sample provides the space for a carbon-glass temperature sensor. This sensor is used as input for a temperature control loop, which adjusts the electrical power in the heater wire. The proximity and good thermal coupling of the temperature sensor, heater wire and sample results in very stable temperatures during operation. Fluctuations are usually smaller than 0.02 K.

The sample is held in place by eight pogo pins, of which four also provide the electrical contact to the patterned track (see 3.1.4.4 above). This method allows quick and easy sample mounting and provides reliable electrical contacts. A small problem encountered during many hours of operation was an entangling of the thin copper leads to the pogo pins, the temperature sensor and the heater wire due to the rotation of the stage. It is however possible to choose a scan sequence for angles which virtually eliminates entangling. Replacement of 0.3 mm diameter single conductor wires with stranded wires of the same cross section avoided the occasional braking of these thicker wires.

3.3.2 Goniometer alignment errors

In *c*-axis films J_c can change very rapidly with ϑ if B is nearly within the *ab*-plane. In this regime even small misalignment angles of the instrument can have a strong effect on the measured J_c values. To compensate for these errors it is necessary to scan the field in a band region close to the *ab*-plane (e.g. $88° \le \vartheta \le 92°$, $0° \le \varphi \le 360°$), analyse the data to determine the three error parameters and finally correct the data.

The geometry for this case is illustrated in Fig. 3.13 in the coordinate system of the film. If the rotation axis ω of the field is not exactly parallel to the film normal (= *c*-axis in *c*-

axis films), then ϑ becomes φ dependent. The spherical coordinates ϑ_ω and φ_ω of the rotation axis ω are the two parameters describing this effect. If the magnetic field in the apparatus is not exactly normal to ω, ϑ is not 90° in the node line (the line in the ab-plane which is exactly normal to ω) and a uniform offset in ϑ can be observed. The deviation δ, defined by $90° - \vartheta$, can be calculated using spherical trigonometry and with the assumption that ϑ_ω and δ are only small angles. A standard transformation of spherical coordinates between the film system (c-axis is pole, no dash) and the system with ω as pole (dashed system [']) results in the following formula for ϑ:

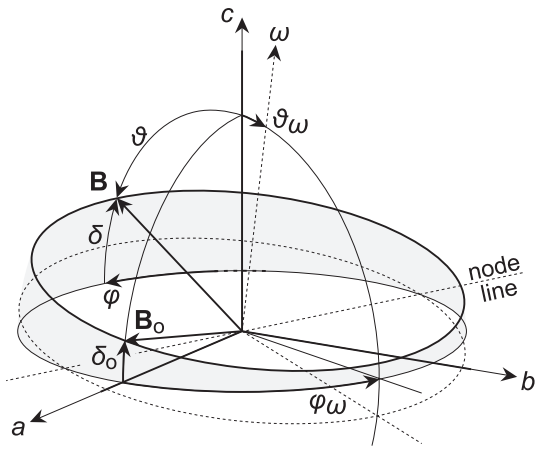

Figure 3.13
Path on the unit sphere (bold circle) **B** follows during a rotation around the axis ω, which is not perfectly parallel to the c-axis. Furthermore **B** might not be exactly normal to ω. A possible set of error parameters are ϑ_ω, φ_ω and δ_0.

$$\cos\vartheta = \cos\vartheta_\omega\cos\vartheta' - \sin\vartheta_\omega\sin\vartheta'\cos(\varphi' - \varphi_\omega) \tag{3.1}$$

With the simplifications $\cos\vartheta \approx \delta$, $\cos\vartheta' \approx \delta'$, $\cos\vartheta_\omega \approx 1$, $\sin\vartheta' \approx 1$ and $\sin\vartheta_\omega \approx \vartheta_\omega$ this reduces to

$$\delta \approx \delta' - \vartheta_\omega\cos(\varphi' - \varphi_\omega). \tag{3.2}$$

This is simply a harmonic in φ' with amplitude ϑ_ω, phase φ_ω and offset δ', which is the

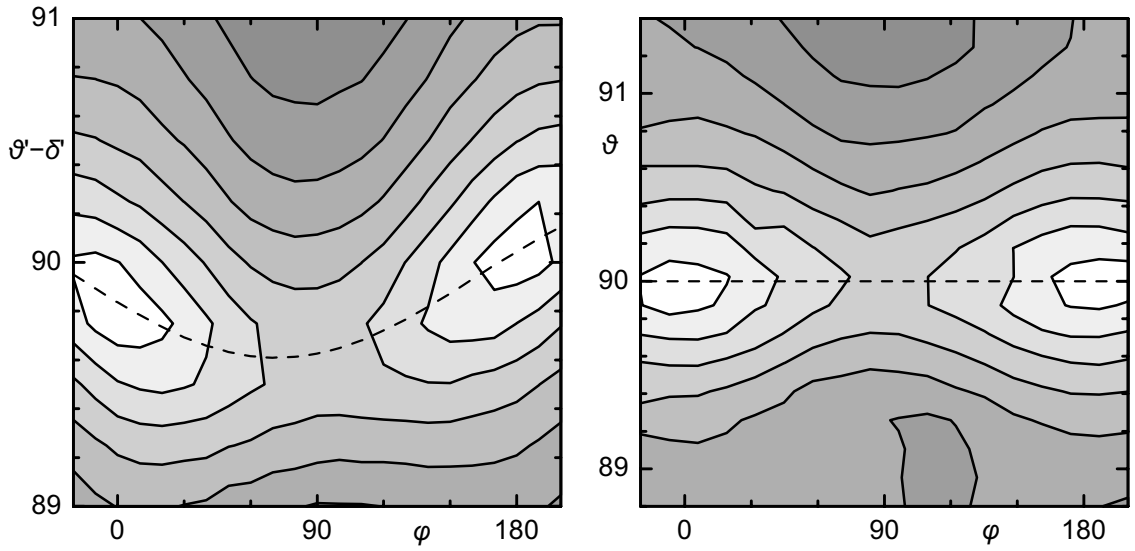

Figure 3.12
Contour plots of J_c as a function of field orientation. The left plot shows the data uncorrected for instrument errors, on the right they are corrected. In both cases the 'ridge' is shown as a dashed line. This is the location where **B** is exactly parallel to the ab-plane.

deviation at the node line. Alternatively to δ', the deviation δ_0 at $\varphi = 0°$ can be used:

$$\delta \approx \delta_0 + \vartheta_\omega \cos(\varphi_\omega) - \vartheta_\omega \cos(\varphi' - \varphi_\omega) \tag{3.3}$$

Finally φ' can be replaced by φ because the differences are only of second order in δ and ϑ_ω. Fig. 3.12 shows an uncorrected and a corrected contour plot of J_c with **B** in the vicinity of the *ab*-plane (note the scale for ϑ). The parameters in this example are $\vartheta_\omega = 0.33°$, $\varphi_\omega = 71.7°$ and $\delta_0 = 0.17°$. The lighter the colour in the plots the higher is J_c. The two maxima (the lightest patches) occur for force free configuration where **B** is parallel to the current in the film.

3.3.3 Cryostat and temperature control

The cryostat for the 8 T magnet from Oxford Instruments follows a design often used for NMR magnets which is slightly unusual for housing superconducting laboratory solenoids. The main advantage of this layout is the very good thermal insulation of the helium vessel and consequently an exceptionally long helium holding time of about a week during normal operation. Together with the installed variable temperature insert (VTI) this cryostat can be described as a 'toroidal onion': The innermost torus is the 8 T

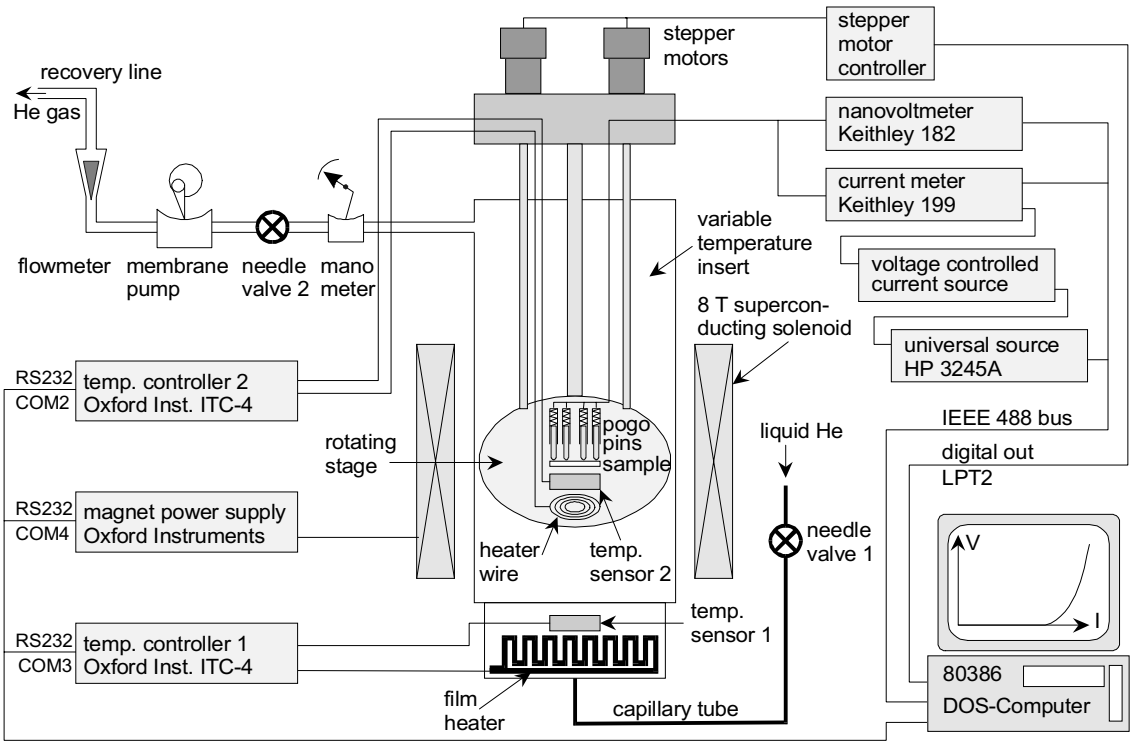

Figure 3.14
Block diagram of J_c measurement apparatus.

solenoid with a cold vertical bore of 70 mm. It is attached to and surrounded by the next torus, the helium vessel, which is suspended at only three points, of which two are the necks for the current leads, instrumentation wires and the helium transfer tube. The helium vessel is wrapped in superinsulating mylar foil and surrounded by the torus formed by a radiation shield and the attached liquid nitrogen tank. After more superinsulation eventually the outermost torus, the external vacuum vessel and the VTI, is reached.

From the main helium bath a capillary tube is routed to the bottom of the VTI via needle valve 1 (see Fig. 3.14) to enable the cooling of the space inside the VTI. Helium is sucked into the VTI by an external membrane pump attached to the warm top end of the VTI via needle valve 2 and a manometer. The two needle valves allow the control of the helium flow rate and the pressure in the VTI. For this arrangement to work it is essential that there is no gas leak at the top of any sample carrier (probe) inserted into the VTI. Probes are clamped to the VTI with standard KF 50 flanges. To create higher temperatures in the sample space a film heater is attached to the bottom copper block of the VTI, the power of which can be regulated by temperature controller 1. This controller monitors the output of temperature sensor 1, which is also attached to the bottom of the VTI.

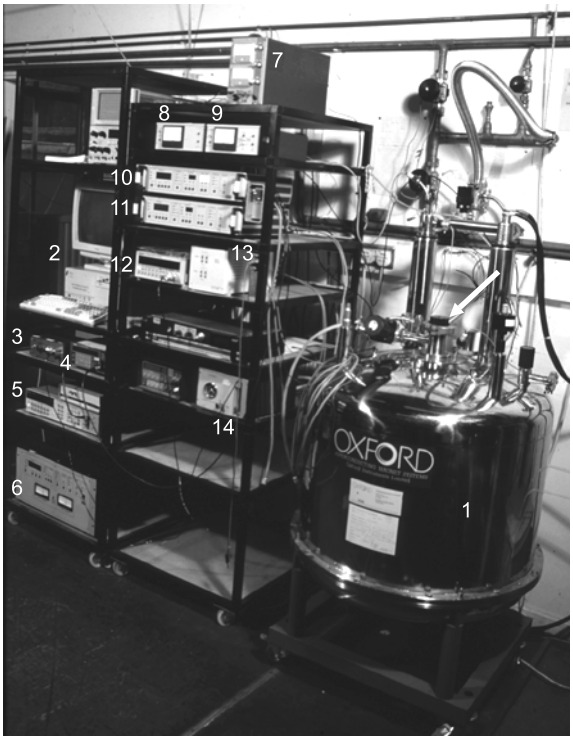

Figure 3.15
Cryostat and measurement equipment. 1 – helium cryostat, 2 – 386 PC, 3 – voltage controlled current source, 4 – Keithley 199 DMM, 5 – HP universal source, 6 – magnet power supply, 7 – power supply for unblocking needle valve 1, 8 – He level meter, 9 – LN_2 level meter, 10 – *T* controller 2, 11 – *T* controller 1, 12 – nanovoltmeter, 13 – stepper motor controller, 14 – He pressure gage, flow meter and needle valve 2. The arrow points to the flange at the top end of the VTI.

After some experimentation with the helium flow rate and various settings on the two temperature controllers the following operating procedure was adopted: Controller 1 is used to monitor the temperature of the helium entering the VTI. Its heater output is set to zero. Needle valve 1 is completely opened

ensuring atmospheric pressure in the VTI and valve 2 opened just enough to keep the bottom of the VTI at 4.2 K. Stability of the desired sample temperature is entirely achieved by controller 2 together with the sensor and the heater wire on the rotating stage. For stable control at temperatures below 20 K the helium flow rate has to be increased slightly. After inserting the goniometer into the VTI it takes about 1 hour to achieve stable conditions for experiments below 80 K. The only repeating problem encountered during the experiments was a blocking of needle valve 1, probably by solid air or nitrogen. With some patience the capillary usually could be cleared by powering an attached heater wire.

3.3.4 Electrical measurements

For critical current measurements the sample temperature is adjusted as described above and the magnetic field ramped to the desired value, where the solenoid is switched into persistent mode. Magnet operation is controlled by sending commands from the computer to a dedicated power supply via a serial link (RS232; see Fig. 3.14). The angles are set by sending TTL pulses form the PC's parallel port to the stepper motor controller, which was custom built by the electronics section of the Materials Science Department. It is a so called microstep controller where each input pulse only generates a phase advance of one tenth of 2π, which has the advantage of smooth motor operation and even torque in addition to the finer angular resolution. Considering the particular winding of the motors used and all the gear ratios involved 2166 $^2/_3$ pulses are necessary to change ϑ or φ by one degree. The angular resolution of the goniometer is therefore certainly not limited by the quantisation of the stepper motor control, but rather by mechanical precision.

Two different methods were used to determine the critical current I_c of a track. With the first method a complete *IV*-curve is recorded for each angle by the computer using the instruments shown in the top right corner of Fig. 3.14. Here the HP universal source generates a linear voltage ramp which is converted to a linear current ramp by the voltage controlled current source. This current is conducted through the sample. The HP source generates the voltage ramp by internally executing a Basic program previously downloaded and launched from the computer. This allows the computer to exclusively monitor the readings of the Keithley 182 nanovoltmeter and the Keithley 199 multi-

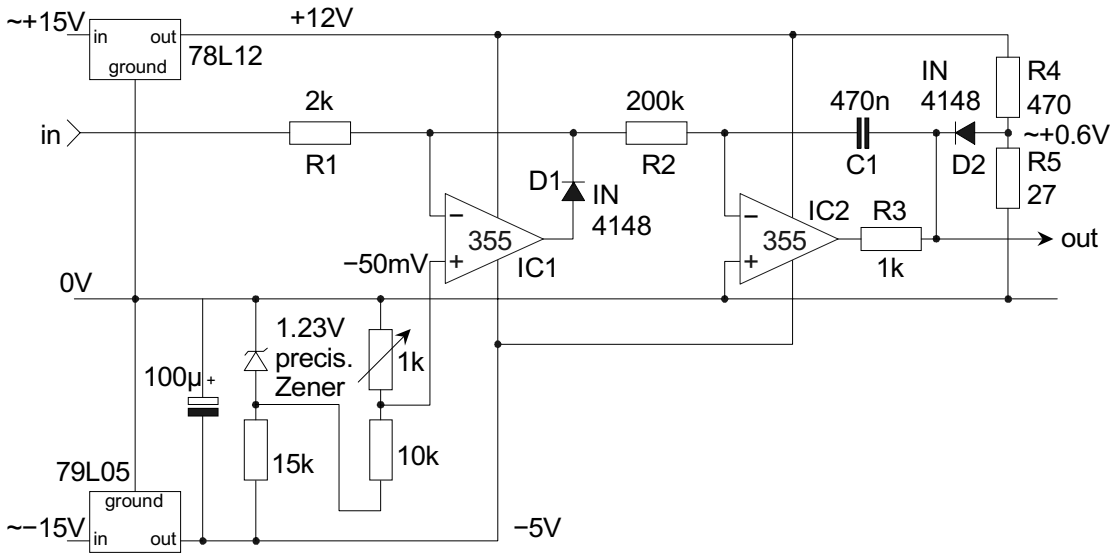

Figure 3.16
Circuit diagram of inverting integrator used as current controller. IC1, D1 and the network supplying the −50 mV form an active clamp (Horowitz and Hill, 1980, p 120), which let only signals pass which are larger than −50 mV and thereby limit the rate of increasing sample current. IC2, C1 and R2 are the inverting integrator and D2, R4 and R5 prevent the output from dropping below about−0.1 V.

meter, which is used as a current meter. Each *IV*-curve is saved to disk and the critical current determined by using a voltage criterion in the range of 2 µV.

Since each current ramp to I_c lasts between 30 and 45 seconds, a scan of many angles can take a rather long time. For this reason a second method was developed where a semi-analogue feedback loop keeps the applied sample current always at a value where the sample voltage is a constant preset value (pseudo constant voltage operation). In this loop the Keithley nanovoltmeter is used as a sensitive voltage preamplifier with some additional programmability. It is set to generate an output voltage proportional to the sample voltage minus the desired criterion voltage ($V_{out} \propto V_{sample} - V_{criterion}$). This signal is routed to a little circuit (Fig. 3.16) which essentially functions as an inverting integrator (A few additional components limit output range and the positive slope of the output voltage to protect the sample.). The output of the custom integrator controls the sample current via the voltage controlled current source. In idle mode the nanovoltmeter output is programmed to supply a comparatively high positive voltage, which drives the integrator down resulting in zero current. At the beginning of a measurement the nanovoltmeter is reprogrammed according to the above formula and a negative output results which lets the integrator generate an increasing ramp. When the sample voltage reaches the criterion voltage the nanovoltmeter output equals zero and the integrator

holds the reached value. If the sample voltage rises for some reason the integrator reduces the sample current until it reaches again the criterion voltage. This loop is only semi-analogue because the nanovoltmeter generates the output voltage from the digitally processed readings about ten times per second, which is fast enough for this application.

Now the sample can be rotated to different angles with the feedback loop permanently engaged. Changes in I_c are automatically followed, measured by the Keithley 199 current meter and transferred to the computer. In this way a reading at one angle takes between 5 and 10 seconds. This time is needed to rotate the sample and wait until all mechanical vibrations of the wires in the goniometer have ceased. These vibrations generate high induced voltage noise because of the presence of the strong magnetic field.

3.3.5 Data acquisition software.

Nearly all instruments of the J_c measurement system are connected to and controllable by a standard PC (see Fig. 3.14). To coordinate the operation of all these components a number of programs and program modules were written with the specialised data-acquisition software Asyst, which runs under DOS.

Three program modules enable the communication with the two temperature controllers and the magnet power supply via RS232 serial links. All three instruments were manufactured by Oxford Instruments and therefore follow a similar communications protocol. Higher level programs simply call these modules and hand over the desired temperature or field. When this value is physically reached and stable conditions established control returns to the calling routine. Additional commands for querying the status and readings of the instruments are provided as well.

The stepper motor controller, which can not communicate using any standard protocol since it has no built in microprocessor, is steered by toggling the eight data lines of the parallel port. For each motor the state of one line determines the rotation direction, another the current level through the motor windings (standby and full current) and a third line is used to send the pulses for advancing the motor. During program writing careful tests were conducted to send these pulses with the correct frequency and without any glitches, particularly during acceleration and deceleration. Eventually correct timing

and smooth motor rotation could be achieved. The angles of the goniometer are now adjusted simply by handing the desired values of ϑ and φ to the stepper motor module, which returns control when the angles are reached.

The Keithley meters and the HP universal source are attached to an IEEE 488 bus with the computer as system controller. Asyst supports all common IEEE 488 commands, but it was nevertheless necessary to write routines adapted to the instrument specific command strings sent over the bus. Some of these commands allow the transfer of meter readings to the computer, others set instrument specific parameters or query the instrument status. The most complex instrument is the HP universal source, which can internally execute Basic programs of considerable complexity to generate a wide variety of wave forms and output signals. As described above a little program is used to generate a linear ramp, the start and end of which is triggered by commands from the computer.

These program modules were integrated into two main programs, one for each of the two operation modes. Upon launching they first query the user for a number of parameters like data filenames, range of operation and execution speed. Next all instruments are initialised and their correct status verified, an array of ϑ-φ pairs for the angles to scan read from disk and the user prompted to start the main measurement loop.

When recording full *IV*-curves the main loop begins by setting ϑ and φ, followed by starting the current ramp. During the ramp the program continuously transfers the readings from the two Keithley meters and immediately displays each data point on the monitor enabling a real time supervision of the measurement. When the sample voltage reaches a set threshold value the current is turned off, J_c calculated and the obtained data saved to a disk file on the PC. This ends one cycle and the next starts by setting ϑ and φ to another pair of values.

With the method employing the feedback loop, the main loop only consists of setting the angles, waiting for a preset time to allow the settling of the circuit to a stationary condition and reading the current from the Keithley 199 meter. On the computer monitor J_c is displayed as a function of either ϑ or φ as soon as a new data point is available and eventually the complete scan saved to a disk file.

For data analysis a small routine was written to parameterise measured *IV*-curves for easier and more accurate determination of J_c. However the main analysis was performed manually with the spreadsheat and plot program Origin.

3.4 Concluding remarks

The availability of expertise and equipment for all steps necessary for the described experiments – film deposition, further film treatments, patterning and electrical measurements – within our research group or the department proved to be very valuable and instructive. It allowed constant discussion and improvement of individual processes and the easy adaptation of subsequent steps.

3.5 References

Baudenbacher, F., K. Hirata, P. Berberich, H. Kinder and W. Assman, 1991, Smooth YBCO films on MgO with good superconducting properties. *High Temperature Superconductor Thin Films* L. Correra, Ed., Amsterdam, North-Holland, 365-70.

Herzog, R. and J.E. Evetts, 1994, Review of Scientific Instruments **65**, 3574.

Horowitz, P. and W. Hill, 1980, *The art of electronics*. Cambridge, Cambridge University Press.

Inam, A., R. Ramesh, C.T. Rogers, B. Wilkens, K. Remschnig, D. Hart and J. Barner, 1991, IEEE Trans. Magn. **27**, 1603-6.

Miyazawa, S., M. Sasaura and M. Mukaida, 1992, Evidence of two-dimensional epitaxial growth of YBCO thin films on lattice--matched $NdGaO_3$ substrates. *High Temperature Superconductor Thin Films* . L. Correra, Ed. . Amsterdam, North-Holland, 741-746.

Poppe, U., J. Schubert, R.R. Arons, W. Evers, C.H. Freiburg, W. Reichert, K. Schmidt, S. W. and K. Urban, 1988, Solid State Commun. **66**, 661.

Przyslupski, P., R. Herzog, A.J. Pauza, R.E. Somekh and J.E. Evetts, 1993, IEEE Trans. Appl. Supercon. **3**, 1283.

Shokoohi, F.K., L.M. Schiavone, C.T. Rogers, A. Inam, X.D. Wu, L. Nazar and T. Venkatesan, 1989, Appl. Phys. Lett. **55**, 2661.

Somekh, R.E., 1990, The Sputter Deposition of Superconducting Ceramics. *Physics and Materials Science of HTS (Nato ASI Series, Series E: Applied Science)*. R. Kossowsky, S. Methfessel and D. Wohlleben, Eds. Dordrecht/Boston/London, Kluwer Academic Publishers. **181**, 327-348.

Somekh, R.E. and Z.H. Barber, 1992, The Deposition of Ceramic Superconductors. *Physics and Materials Science of HTS II* . R. Kossowsky, S. Methfessel and D. Wohlleben, Eds. Dordrecht/Boston/London, Kluwer Academic Publishers, 443-469.

Terashima, T., Y. Bando, K. Ijima, K. Yamamoto, K. Hirata, K. Hayashi, K. Kamigaki and H. Terauchi, 1990, Phys. Rev. Lett. **65**, 2684-2687.

Chapter 4

Critical Currents in *c*-axis YBCO Films

Soon after the discovery of superconductivity at 90 K in YBCO and the determination of the superconducting phase, the quest for practical applications led to questions concerning the current carrying capacity of the new material, particularly at elevated temperatures (~77 K). First assessments using measurements on polycrystalline bulk samples were rather disappointing, because, as it turned out, grain boundaries severely limited supercurrents. A very exciting development was that highly oriented thin films exhibited large critical current densities (Chaudhari *et al*., 1987) showing the potential of the new materials. Thus high quality HTS thin films, and particularly $YBa_2Cu_3O_{7-\delta}$ films with *c*-axis orientation, became the sample material of choice for many studies of the fundamental properties of the new superconductors. Now HTS thin films are also used in active and passive devices and their virtues are investigated in this context.

This chapter presents critical current measurements on *c*-axis YBCO films with an emphasis on the dependence of J_c on the direction of a constant applied magnetic field at several fixed temperatures. At the beginning (section 4.1) experimental studies of the J_c anisotropy and the interpretation of the obtained data reported by other researchers are reviewed. Two models for the angular dependence of J_c are found. One is based on the anisotropic GL theory of a homogeneous material whereas the other starts from a model of a layered superconductor proposed by Lawrence and Doniach (1970). As a prerequisite to finding which model is more applicable to the experimental data of this thesis, J_c is studied as a function of B applied parallel to the *c*-axis in section 4.2. Angular experiments presented in section 4.3 show that the 2D model based on a layered superconductor clearly describes the data better, particularly at low temperatures. The key parameter of this model is B_z, the field component parallel to the *c*-axis.

In section 4.4 concepts of flux lines in layered superconductors are studied. In addition a model of a pancake vortex at a pinning site is developed in section 4.4.3, which shows how a Lorentz force component in *c*-direction (F_L^z) can influence J_c. The main result of the model is an expression for the φ-dependence of J_c at constant ϑ, which is compared

to experiments in section 4.5. Section 4.6 returns to $J_c(\vartheta)$ by looking into the details of deviations from the 2D model which can be large for higher temperatures. It is found that the coupling of pancakes of the same flux line has a characteristic influence on the deviations. The associated parameter is w, the average (horizontal) distance between neighbouring pancakes. Finally, in section 4.7, measurements on deoxygenated films show that YBCO becomes even more 2D like when the coupling between layers is reduced.

The new configurations accessible by the 2-axis goniometer allowed a series of J_c measurements on *c*-axis films, which resulted in the determination of three key properties influencing J_c: the pancake density (B_z), a Lorentz force component in *c*-direction (F_L^z) and the coupling of pancakes of one flux line (w).

4.1 Previous experiments and their interpretations

4.1.1 Introduction

Initial estimates for J_c in HTS were obtained using magnetisation measurements on bulk samples and single crystals (Dinger *et al*., 1987; Yeshurun *et al*., 1989). These experiments revealed that J_c can be very high ($\sim 5 \times 10^{10}$ Am^{-2}) for currents flowing in the *ab*-plane and that it is much smaller for currents in *c*-direction. A large number of magnetisation experiments on YBCO and other HTS has since revealed a rich structure of the phase diagram of the flux-line lattice and interesting thermal and time dependent effects. Unfortunately the complex vortex structure, the strong anisotropy and geometrical effects (demagnetisation effects) as well as the *a priori* need for a model describing the penetration of magnetic field into a sample (critical state model) make the extraction of J_c values from magnetisation measurements difficult. Experiments measuring J_c and other transport properties directly are therefore necessary to obtain data unaffected by these constraints and free from ambiguous interpretations. With transport measurements it is also possible to apply currents and fields in independent directions relative to the crystal axes.

Since bulk samples are generally polycrystalline and the crystal axes of the grains not aligned, transport measurements on these samples are unable to probe the intrinsic

material properties. Critical current densities and resistivities are usually determined by the intergrain behaviour. Transport measurements on single crystals are difficult to conduct because of the tiny sizes of available crystals. It is an achievement to attach 4 fine wires somewhere on a crystal to enable a measurement, but a precise geometry of the test track is virtually impossible to obtain. Thin films on the other hand do not suffer from these restrictions. They can be deposited epitaxially on a number of substrates in a clearly defined crystal orientation. Conventional photolithographic methods allow the fabrication of test patterns with accurately defined dimensions, usually in the micrometer range, to enable experiments with moderate currents ($\lesssim$1 A) even at very high current densities.

4.1.2 Resistive transition

The first transport property of YBCO determined directly was the electrical resistivity as a function of temperature – the resistive transition. In practically all laboratories where HTS samples are produced their resistances are recorded from room temperature downwards to obtain an indication of the sample quality and to determine T_c. A sample is often regarded as 'good' when T_c (defined by $R(T_c) = 0$) is above 90 K, the transition sharp and $R(T = 300\ \mathrm{K})/R(T = 100\ \mathrm{K})$ close to 3.

More systematic studies of the resistive transition in magnetic fields applied at various directions were performed by Palstra *et al*. (1988) and Iye *et al*. (1988) on single crystals and by Iye et. al (1990) on thin films. The interesting feature discovered is a substantial broadening of the resistive transition with increasing field. Furthermore this broadening is much more pronounced for fields applied parallel to the *c*-axis (~12 K at 5 T for $\rho = 0$ [Palstra]) than for fields parallel to the *ab*-plane (~4 K at 5 T). From the linear traces of the resistivity data in Arrhenius plots ($\ln R$ versus $1/T$) the authors conclude that the origin of the effect must be thermal activation. Iye finds, from more detailed angular measurements, the variation of B_{c2} with ϑ near T_c well described by Equ. (2.18), which is derived from the anisotropic GL-theory. Other experiments confirmed that the anisotropy of the basic phenomenological superconducting parameters (λ, ξ, B_{c1} and B_{c2}) are well described by the anisotropic GL-theory (see section 2.3). The slopes of $B_{c2}(T)$ near T_c are 10.5 T/K and 1.9 T/K for $B \parallel ab$ and $B \parallel c$ respectively (Welp *et al*., 1989).

4.1.3 Order parameter modulation and intrinsic pinning

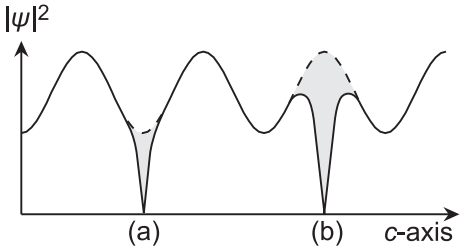

Figure 4.1
Spatial variation of superconducting order parameter along the *c*-axis without vortices (dashed line) and with two vortices present at positions (a) and (b) (solid line). (Tachiki and Takahashi, 1989b)

The extremely steep slopes confirmed the very high values of B_{c2} previously obtained from magnetisation measurements. The high B_{c2} values implied short coherence lengths ξ_i, particularly ξ_c ($\xi_c = \varepsilon\xi_{ab}$, $\varepsilon < 1$, see Equ. 2.15). In YBCO $\xi_{ab} \approx 1.1$ nm and $\xi_c \approx 0.2$ nm at $T = 0$. ξ_c is smaller than the spacing of the CuO_2 double layers (≈ 0.8 nm) except for temperatures close to T_c. As the electrical conduction in the cuprates is mostly concentrated in the CuO_2 layers and ξ_c is so short, Tachiki and Takahashi (1989b) considered a variation of the order parameter in the *c*-direction with a periodicity of the lattice constant *c*. They further argued that this modulation of the order parameter generates a periodic potential for Abrikosov vortices parallel to the *ab*-plane: if the core of the flux line is located in between two CuO_2 double layers, where the order parameter is already reduced (Fig. 4.1a), the loss of condensation energy is smaller than when the flux line core is placed in a CuO_2 double layer (Fig. 4.1b). The gradient of this potential generates a pinning force on the flux

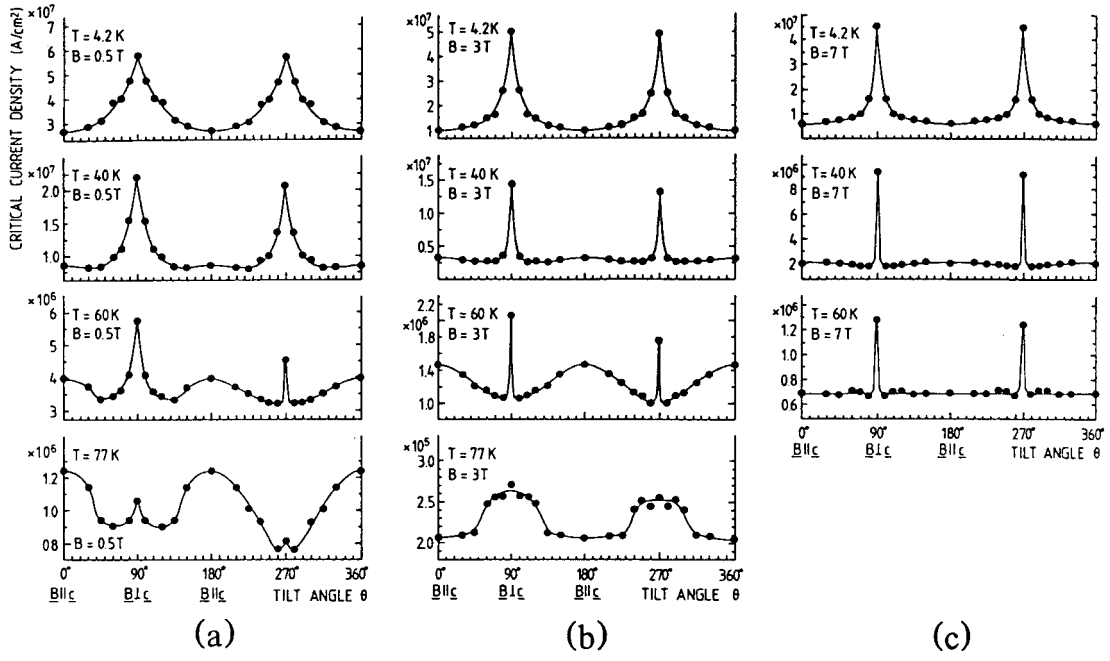

Figure 4.2
$J_c(\vartheta, \varphi = 0)$ as published by Roas *et al.* (1990). "J_c at different T as a function of ϑ."

lines, which Tachiki and Takahashi named intrinsic pinning force, because the effect is intrinsic to the crystal structure. Even a faultless single crystal would pin flux lines in this way. Intrinsic pinning depends strongly on the ratio of ξ_c to c. Tachiki and Takahashi calculated a maximum pinning force for $\xi_c/c \approx 0.3$ and a rapid decrease for larger values. Above $\xi_c/c \approx 1$ the effect becomes negligible because the strength of the modulation decreases and because each flux line core contains several CuO_2 double layers where gradients of opposite sign add up to only small effective forces. The volume pinning force derived from intrinsic pinning can be large because all flux lines are pinned coherently along their whole length if they are parallel to the *ab*-plane.

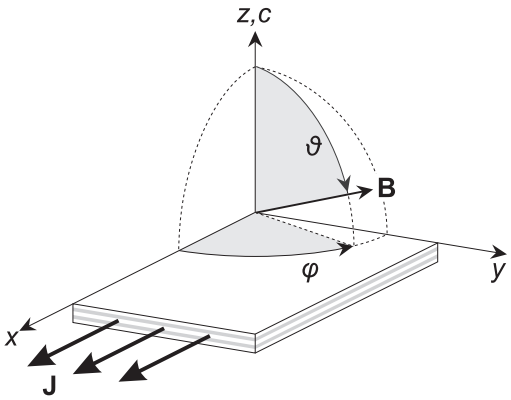

Figure 4.3
The angles ϑ and φ in experiments on *c*-axis films (*c*-axis normal to the film surface). (*x*, *y*, *z*) and (ϑ, φ) are defined by the film plane and the current direction.

The idea of intrinsic pinning gained importance when Roas *et al*. (1990, see Fig. 4.2) for the first time measured the dependence of J_c in YBCO thin films on the magnitude and direction of an applied magnetic field. They found strong maxima of J_c at all fields and temperatures when the field was parallel to the *ab*-plane. At low fields and temperatures the variation with ϑ (see Fig. 4.3; $\varphi = 90°$ for all their experiments) is smooth, but at high fields and temperatures the maxima at $\vartheta = 90°$ become very sharp: in the range of a few degrees J_c varies by a factor of two and more. This feature is now often referred to as 'intrinsic pinning peak'. In addition to these peaks Roas *et al*. observed maxima at $\vartheta = 0°$, which they attributed to enhanced pinning by twin planes present in their films.

4.1.4 Tachiki and Takahashi model

Encouraged by these experimental results Tachiki and Takahashi (1989a) developed a model (T&T model) to explain the ϑ dependence of J_c, by assuming that tilted flux lines ($0° < \vartheta < 90°$) have a step like shape in the HTS (Fig. 4.4). In their model different pinning forces act on flux line segments parallel to the *c*-axis and segments parallel to the *ab*-plane. The former are strongly pinned by the intrinsic pinning effect, whereas Tachiki and Takahashi assume pinning by twin planes, grain boundaries or other planar

imperfections for the vortex segments crossing the CuO_2 layers, which are often called 'pancake vortices' after Clem (1991; 1992; 1993). For the latter type of pinning F_p^y, the volume pinning force in *y*-direction, is proportional to $1/a$ and hence to $B_z^{1/2} = (B\cos\vartheta)^{1/2}$, with a the average spacing of the pancakes. J_c is proportional to $F_p^y/\cos\vartheta$ using a simple Lorentz force argument in the *ab*-plane and the final result of the analysis by Tachiki and Takahashi for J_c is:

$$J_c(\vartheta) = \text{smaller of} \left[\begin{array}{c} J_c(90°), \\ \dfrac{J_c(0°)}{\sqrt{\cos\vartheta}} \end{array} \right] \tag{4.1}$$

The angle (close to $\vartheta = 90°$) at which J_c crosses from one solution to the other is called the 'lock-in angle' because, within the model, flux lines align completely with the *ab*-plane for applied field directions between this angle and 90°. In this regime J_c becomes independent of ϑ. Further refinements of these ideas can be found in (Tachiki *et al*., 1991).

Subsequently several authors measured $J_c(\vartheta)$ in YBCO films and used Equ. (4.1) to analyse their data. Christen *et al*. (1990; 1991) find "overall agreement with the T&T model being only qualitative, but it appears to be best at low temperatures and in high magnetic fields." Nishizaki *et al*. (1991b; 1991a) find good agreement with their thin film data at 77 K below 1 T. The data of Aomine *et al*. (1993) fits well at 45 K and 7 T, but not at lower temperatures. Kuwasawa *et al*. (1990) report good agreement for several temperatures at 5 T. Walkenhorst *et al*. (1991) argue that "the angular dependence of the depinning field is generated by a superposition of two independent motions of the flux lines: one parallel and one perpendicular to the CuO_2 planes." Their data can be well explained by the T&T model at low temperatures.

All these experiments show that J_c is much larger for $B \parallel ab$ than for $B \parallel c$ and the T&T model (Equ. 4.1) has some success in describing the angular variation in detail in a region around $\vartheta = 0°$, the width of which is not consistent throughout the publications reviewed. The lock in angle with a plateau of J_c in the vicinity of

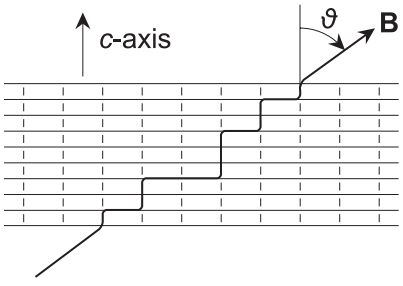

Figure 4.4
A flux line crossing a HTS at a tilted angle according to Tachiki and Takahashi.

$\vartheta = 90°$, an important feature of the model, was never observed in thin films. All measurements conducted with sufficient angular resolution show a rounded peak, possibly a cusp, but no flat maximum. This could be a result of demagnetisation effects in square shaped samples (Bugoslavsky *et al*., 1997).

Direct and convincing evidence for intrinsic pinning has been obtained by magnetisation measurements on clean, nearly defect-free and untwinned YBCO single crystals (Oussena *et al*., 1994). For magnetic fields applied parallel to the *ab*-plane (deviations have to be smaller than 1°) several maxima appear in the magnetisation curve. The periodicity is such that each successive maximum represents a state of the flux line lattice where the lattice spacing in *c*-direction is commensurate with the layer spacing of the crystal. It is thus possible to use the crystal structure as a ruler for the flux line lattice and to determine the anisotropy parameter ε accurately. The authors report a $\Gamma = 1/\varepsilon = \sqrt{M/m}$ of 5.6 ± 0.1.

4.1.5 Layered superconductors and the 2D model

Precise angular measurements on *c*-axis oriented BiSCCO films by Iye *et al*. (1989) revealed that the resistivity near T_c does not depend on φ for $\vartheta = 90°$ (i.e. B is rotated in the *ab*-plane; see Fig. 4.3). This is surprising since the flux flow resistivity in conventional superconductors is known to depend on the Lorentz force acting on the flux lines, which in this geometry is proportional to $\sin\varphi$. Kes *et al*. (1990) first explained this unusual behaviour by modelling the HTS as stacks of superconducting and non superconducting layers for which Lawrence and Doniach (1970) had developed a theoretical description (see section 2.7). The theory is applicable for the HTS not too close to T_c because ξ_c is then smaller than the spacing of the CuO_2 double layers (For YBCO T has to be smaller than about $0.8\,T_c$ (Tinkham, 1996, p 325).). The order parameter between the layers is strongly suppressed leading to reduced coupling between layers. A field applied parallel to the planes does not penetrate the sample in the form of Abrikosov vortices but like Josephson vortices (or Josephson strings), which change the order parameter much less and hence have a lower line energy. Since screening is weak, both B_{c1} and the magnetisation are extremely small for fields parallel *ab* ($<10^{-5}$ T at $T = 0$ K) and macroscopically the material appears 'magnetically transparent'. This finally leads to the important result that in highly anisotropic, layered

superconductors many properties should only depend on the field component normal to the *ab*-plane which in the geometry of Fig. 4.3 is $B_z = B\cos\vartheta$. For the in-plane critical current density the following scaling rule is expected to apply:

$$J_c(B, \vartheta, \varphi) = J_c(B_z, 0, 0) = J_c(B\cos\vartheta, 0, 0) \tag{4.2}$$

This relation implies that it is only necessary to measure the dependence of J_c on the field parallel to the *c*-axis ($\vartheta = 0$, φ undefined) in order to calculate the dependence for all ϑ and φ. Because of the weak coupling between superconducting sheets, layered superconductors behave more like a stack of very thin, 2-dimensional planes (where $\xi_c \approx d$, the spacing of the planes) than like 3-dimensional bulk samples ($d \ll \xi \ll D$; D is of the order of the sample size). In the limit of weak coupling the model of layered superconductors is therefore often referred to as 2D model.

Although Kes *et al*. assumed that the 2D model should only be applicable to extremely anisotropic superconductors such as BiSCCO with $\xi_c \ll d$, several researchers used the idea to interpret their experiments on YBCO samples, where Josephson coupling between the layers is not negligible. Aomine *et al*. (1993) compare the T&T model and the 2D model to their data and find reasonable agreement for the former at 45 K and for the latter at 20 K. Extensive measurements were conducted by a group in Vienna (Schalk *et al*., 1992b; Schalk *et al*., 1993; Schalk *et al*., 1992a; Samadi Hosseinali *et al*., 1994), showing that high quality samples are well described by Equ. (4.2) at low temperatures, particularly at high magnetic fields. They observed slight deviations for ϑ close to 90°, where the zero field J_c value predicted by the model proved too high. Important evidence for the validity of the 2D model was also contributed by a group in Darmstadt (Adrian *et al*., 1993; Jakob *et al*., 1993; Schmitt *et al*., 1992; Schmitt *et al*., 1993) with experiments on pure YBCO films, YBCO/$PrBa_2Cu_3O_{7-\delta}$ superlattices, doped $YBa_2(Cu_{1-x}Zn_x)_3O_{7-\delta}$ and BiSCCO films. For YBCO they again find good agreement with (4.2) at low temperatures. Additionally, when rotating B in the plane containing the *c*-axis and J (ϑ-scans with $\varphi = 0°$), the 2D-scaling is still working at intermediate temperatures ($T \approx T_c/2$). A BiSCCO film and a YBCO/PrBCO superlattice film (10 unit cells YBCO : 1 unit cell PrBCO) show excellent scaling behaviour at all temperatures. Li *et al*. (1992) conducted J_c measurements on a set of YBCO/(Pr_xY_{1-x})BCO superlattice films with, by varying x, fine-tuned transition temperatures T_{cPr} of the

(Pr_xY_{1-x})BCO layers. Depending on T and T_{cPr} the YBCO layers were thus coupled or not and for the non-coupled cases J_c followed Equ. (4.2) accurately.

Looking only at J_c measurements the T&T-model and the 2D-model are similar: In both cases J_c is determined by the depinning of the pancake vortices. Tachiki and Takahashi assume that pancakes are pinned by extended defects, which leads to the $J_c \propto (\cos\vartheta)^{-1/2}$ prediction, whereas Kes arrive at the scaling rule Equ. (4.2) without any particular pinning model for the pancakes. The behaviour is simply determined experimentally and used as input in Equ. (4.2). In this empirical sense the 2D-model proposed by Kes is a generalisation of the T&T-model. The main difference, namely the assumption of strongly pinned Abrikosov vortices in a modulated order parameter on one hand and more or less decoupled CuO_2 planes with Josephson strings on the other hand, can not be resolved by angular J_c measurements as long as J_c is determined by the depinning of pancakes (Jakob *et al*., 1993).

4.1.6 Anisotropic Ginzburg-Landau theory

For the models describing the ϑ dependence of J_c proposed by Tachiki and Takahashi (Equ. (4.1)) and Kes *et al*. (Equ. (4.2)) the intrinsic layering of the HTS is essential. Blatter *et al*. (1992; 1994) however pointed out that a superconductor having the same anisotropy as the HTS but no layered structure would also have J_c maxima for $B \parallel ab$ and minima for $B \parallel c$. They adopt a scaling approach to obtain solutions of the anisotropic Ginzburg-Landau equation (Equ. (2.8)) from the well known solutions of the isotropic case. This avoids the laborious task of recalculating all results from Equ. (2.8) directly. The mathematical trick employed is a transformation (a rescaling) of lengths in z-direction and the vector potential such that the effective mass tensor becomes a multiple of the unity tensor (this applies to the HTS with uniaxial anisotropy). The coordinates in the anisotropic system (without ~) are transformed by

$$x = \tilde{x}, \quad y = \tilde{y}, \quad z = \varepsilon\,\tilde{z}, \tag{4.3}$$

and the vector potential and the magnetic field by

$$A_x = \tilde{A}_x, \quad A_y = \tilde{A}_y, \quad A_z = \tilde{A}_z/\varepsilon \quad \text{and} \quad B_x = \tilde{B}_x/\varepsilon, \quad B_y = \tilde{B}_y/\varepsilon, \quad B_z = \tilde{B}_z. \tag{4.4}$$

In the transformed GL equation the gradient term of ψ is isotropic. However, the aniso-

tropy has been shifted to the originally isotropic terms of the magnetic field energy. In general it is not possible to isotropise all terms in Equ. (2.8) simultaneously. When fluctuations of the magnetic field only occur at much larger scales than the natural length scales of the problem considered, the field can be regarded as uniform and easily be calculated. For instance in problems of vortex pinning and vortex interaction the natural length scales are ξ and a, the vortex spacing. In strongly type II materials at applied fields much larger than B_{c1}, ξ and a are much smaller than λ, the scale on which B varies. In this case B is nearly equal to the external field. On the length scales of the problem it is uniform and only determines the flux line spacing a. The order parameter ψ is obtained by solving the isotropised GL equation – or simply by adapting the well known solutions to the boundary conditions at hand (e.g. uniform field in particular direction).

Assuming the validity of the mean field approach (i.e. uniform B), the transformation above maps an isotropic superconductor to the anisotropic original. The mapped isotropic system has the properties of the *ab*-plane of the anisotropic material in all directions. By conducting measurements on the real sample it is therefore possible to determine the characteristics of the isotropic system if *only* properties of the *ab*-plane are probed. For critical current measurements on *c*-axis films this is the case if an applied field is normal to the film since the externally applied current as well as the shielding currents only flow in the *ab*-plane in this case. Transforming the obtained result back to the anisotropic material a prediction of the behaviour for all angles of an applied field is obtained.

The procedure of measuring *ab*-plane properties of the anisotropic sample and using the above transformation in order to obtain predictions for the behaviour of the system at arbitrary directions of applied field can be summarised in the following scaling rule, which is the main result in the paper of Blatter *et al*. (1992):

$$Q(B, \vartheta) = s_Q Q(\varepsilon_\vartheta B, 0) \tag{4.5}$$

with

$$\varepsilon_\vartheta = \sqrt{\cos^2 \vartheta + \varepsilon^2 \sin^2 \vartheta} \tag{2.19}$$

Q stands here for an observable quantity and s_Q is the associated scaling factor. Typical factors are $s_V = s_E = \varepsilon$ for volumes and pinning energies and $s_B = s_H = 1/\varepsilon_\vartheta$ for magnetic fields. For the in plane critical current density J_c^{ab}, s_{J_c} should be 1 (for $\varphi = 90°$), so that

the scaling rule for J_c in *c*-axis films derived purely from the anisotropic Ginzburg-Landau theory is

$$J_c(B, \vartheta) = J_c(\varepsilon_\vartheta B, 0). \tag{4.6}$$

In a formally similar way to the 2D-model of Kes this result allows the deduction of the J_c behaviour for all angles of applied field from $J_c(B \parallel c)$ measurements.

Ravi Kumar *et al*. (1994) used Equ. (4.5) to analyse their measurements of torque hysteresis loops on YBCO films and obtain excellent scaling with $1/\varepsilon = 3.4 \pm 0.3$, which is somewhat small, but confirms that YBCO is not 'transparent' to fields applied parallel to the *ab*-plane. Schalk *et al*. find their $J_c(\vartheta)$ data to be better described by Equ. (4.5) than by the 2D model (Equ. (4.2)), particularly for ϑ values close to 90°.

4.1.7 Emerging questions

One clear question emerging from the models reviewed in the previous sections concerns the relative importance for J_c in YBCO films of the anisotropy of the fundamental superconducting parameters (λ, ξ, B_{c1} and B_{c2}) on one hand and the intrinsic layering on the other. Both, the anisotropy as well as the modulation of the order parameter in *c*-direction, have their origin in the layered crystal structure, but it is not entirely clear that the layering has a direct influence on J_c, as Blatter *et al*. (1992) have pointed out.

Measurements of J_c as a function of ϑ (see sections 4.3 and 4.5) strongly indicate that the layering has a direct influence on J_c and that the concept of intrinsic pinning has some validity. The results, at least at low temperatures, can not be explained with the anisotropic GL theory alone. More details about the nature of the anisotropy and of flux lines and their pinning in YBCO are presented in sections 4.3 to 4.8.

4.1.8 Additional phenomena

The majority of researchers investigating transport properties in YBCO films with magnetic fields applied at various angles, interpreted their data along the lines of at least one of the models outlined above, which have the common feature of comparing data obtained at different values of external parameters (angles, field). The interpretations of the experiments presented in this thesis will follow this scaling approach. Some investigators tried to extend Kramer's (1973) scaling models, which compare J_c measurements

at different temperatures and are so successful in conventional superconductors, to the HTS, but a review by Niel (1992) shows that this is generally not possible because of the effects of thermal activation (Flux creep, TAFF, FLL melting etc. – see section 2.6), which are prominent in the HTS. This is confirmed experimentally by Christen *et al*. (1991).

The following section describes how the effects of thermal activation were approached in the interpretation of the experimental results in this thesis. Two additional topics of relevance for J_c in *c*-axis films are surface pinning and the anisotropy within the *ab*-plane. They are briefly described in 4.1.8.2 and 4.1.8.3.

4.1.8.1 Effects of thermal activation

In conventional superconductors J_c is usually determined by the current density that generates a chosen electric field in the sample. Typical voltage criterions are in the range of a few μVcm^{-1}. Since thermal activation in the LTS only occurs close to $B_{c2}(T)$, the obtained J_c is close to the theoretical J_{co}, for which the pinning potential $U(J)$ becomes 0. This is reflected in a steep voltage rise in the vicinity of J_c, making the value of J_c fairly independent of the exact voltage criterion applied. However, because of thermal activation (see section 2.6) this situation is very different in the HTS. At higher temperatures ($\gtrsim 30$ K) the onset of detectable voltages can be at current densities substantially below J_{co} from where the voltage only rises gradually with J. In this situation it is useful to record complete *IV*-curves to obtain a maximum of information.

For configurations with $\varphi = 90°$ (B always normal to J) Schalk et. al (1994) interpreted *IV*-curves of YBCO films in terms of the simple Anderson-Kim model (Anderson, 1962; Kim *et al*., 1963; Anderson and Kim, 1964) and obtained an unexpected increase of the pinning potential U with temperature. Berghuis *et al*. (1996a) used accurate *IV*-measurements with $B \parallel c$ for a detailed comparison of models describing thermal activation effects in HTS. They showed that the boson glass model (see section 2.6.3) reproduces the data best and that the Anderson-Kim model is not adequate in the HTS because it does not take the divergence of U for small current densities into account.

The emphasis of the experiments reported in this thesis is on the effects of the orientation of an applied field on J_c. Since this study required the sampling of J_c at many

parameter points (ϑ, φ and B), the recording and evaluation of IV-curves at each of these points was not feasible. Instead a fixed voltage criterion between 20 and 40 μVcm^{-1} was used and J_c data obtained in this way compared with J_c values measured at *different* parameter values yet the *same* temperature. Here J_c is not simply and directly related to J_{co}, but it characterises a certain level of activation of the flux lines in YBCO, which should be similar for different ϑ, φ and B at a fixed temperature.

J_c was mostly measured with the continuous current method (see section 3.3.4), which allowed an acquisition rate of one data point every 5 to 10 seconds in the system described in section 3.3. Only at temperatures above 60 K and when J_c was small, full IV-curves were recorded, because the feedback loop did not work reliably under these conditions.

After commissioning the J_c measurement system a number of samples were used to find viable operating conditions. When testing different methods to send current through the fine test track (~200 nm × 30 μm × 500 μm) it unfortunately happened several times that the track was destroyed. More disturbing was a subtle error in the self-made feedback circuit (Fig. 3.16), which destroyed several samples after they had already been measured at a large number of parameters. It took thus a while to iron out all hardware and software errors and to achieve sustainable experimental conditions. Even then there was always the fear of a power cut.

At the same time colleagues in our research group perfected the sputtering process for thin film deposition, which yielded samples with better and better quality. Eventually the spread in the results from different samples became smaller and a coherent picture of the flux line behaviour in *c*-axis films emerged.

4.1.8.2 Surface pinning.

When the strong ϑ dependence of the in plane J_c was first reported by Roas *et al*. (1990) it was not clear if the whole effect, or a part of it, was attributable to geometric effects and surface pinning, since the sharp J_c maxima appear at $\vartheta = 90°$ where B is not only parallel to the *ab*-plane but also parallel to the film surface (see Fig. 4.3) Christen *et al*. (1991) however observed that J_c is nearly independent of the film thickness over a range from 37 nm to 380 nm for several high quality films. To further elucidate this issue J_c

measurements were conducted on films deposited on vicinal substrates, the surface of which is polished at a slight angle to a main crystallographic plane (see Fig. 4.5) (Christen *et al.*, 1991; Lowndes *et al.*, 1995; Berghuis *et al.*, 1996b). With substrates on which the films still grow epitaxially under this condition ($SrTiO_3$) the J_c maximum clearly shifted to the ϑ value where B is parallel to the *ab*-plane and not where B is parallel to the film surface (see Fig. 4.6). However, at high temperatures and low magnetic fields Berghuis *et al.* (1996b) observe an influence of surface pinning in YBCO films. The regime where surface pinning effects are significant is $B < 1$ T at 77 K and $B < 0.25$ T for $T > 50$ K. Outside this regime the strong dependence of J_c on ϑ in the HTS is therefore now firmly established as a bulk effect.

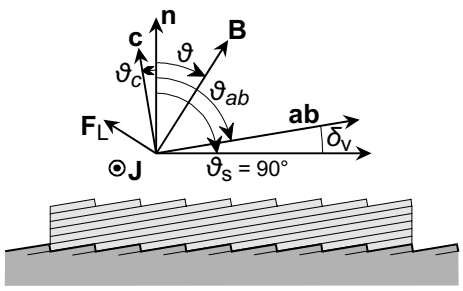

Figure 4.5
The layered structure of YBCO on a vicinally cut $SrTiO_3$ substrate: definition of angles. (δ_v = vicinal angle)

4.1.8.3 Anisotropy within the ab-plane

$YBa_2Cu_3O_{7-\delta}$ is not isotropic within the *ab*-plane as described in section 2.1, but this anisotropy is weak (1.11 (1.15, Dolan *et al.*, 1989) and thin films are usually twinned. The direction within the *ab*-plane in which the current flows does therefore not influence transport measurements as has been shown experimentally by Roas *et al.* (1990) who patterned several test tracks in different directions on one film.

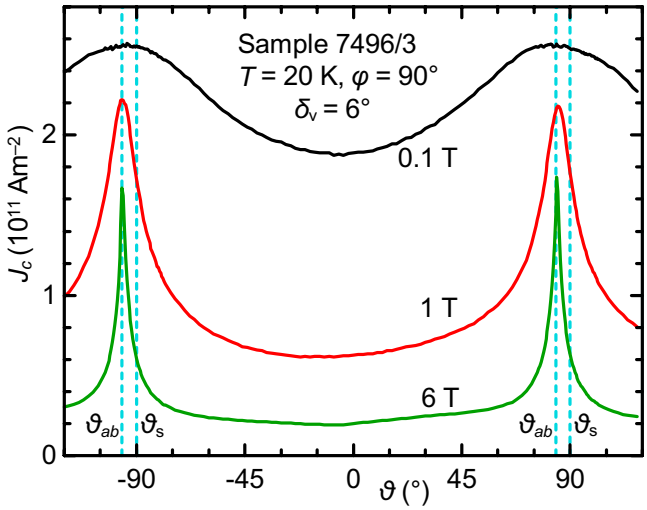

Figure 4.6
$J_c(\vartheta)$ of a vicinal sample ($\delta_v = 6°$). The maxima are clearly at $\vartheta = \vartheta_{ab}$ ($\pm 90° - \delta_v$) and not at $\vartheta = \vartheta_s$ ($\pm 90°$). The dashed lines mark these special configurations. Note that the peaks are symmetrical in respect to ϑ_{ab}. (Data courtesy Peter Berghuis.)

4.2 J_c for fields parallel to the c-axis

In the 2D-model of layered superconductors as well as in the scaling approach of the anisotropic GL-theory, both discussed in section 4.1, J_c as a function of $B \parallel c$ is used to predict the J_c behaviour at other angles of applied field. To evaluate the validity of these models, $J_c(B)$ was measured in this configuration ($\vartheta = 0°$, see Fig. 4.3) on a number of samples at different temperatures.

4.2.1 Field dependence of J_c

In Figs. 4.7 and 4.8 critical current measurements of two typical samples are shown as a function of B. The main features at all temperatures are a rapid decrease of J_c with increasing B at low fields and a rounded maximum at 0 T. The detailed functional behaviour varies slightly from sample to sample, but approximately obeys an inverse power law with an exponent between 0.45 and 0.7. For sample 5861/1 J_c is roughly proportional to $B^{-1/2}$ over a wide range of fields for all temperatures. This can be seen by the data plots being parallel to the dashed lines, which are drawn proportional to $B^{-1/2}$, in the logarithmic plot Fig. 4.9. At the lowest fields the increase of J_c with decreasing B levels off and a J_c plateau can be seen in the double logarithmic plots Figs. 4.9 and 4.10.

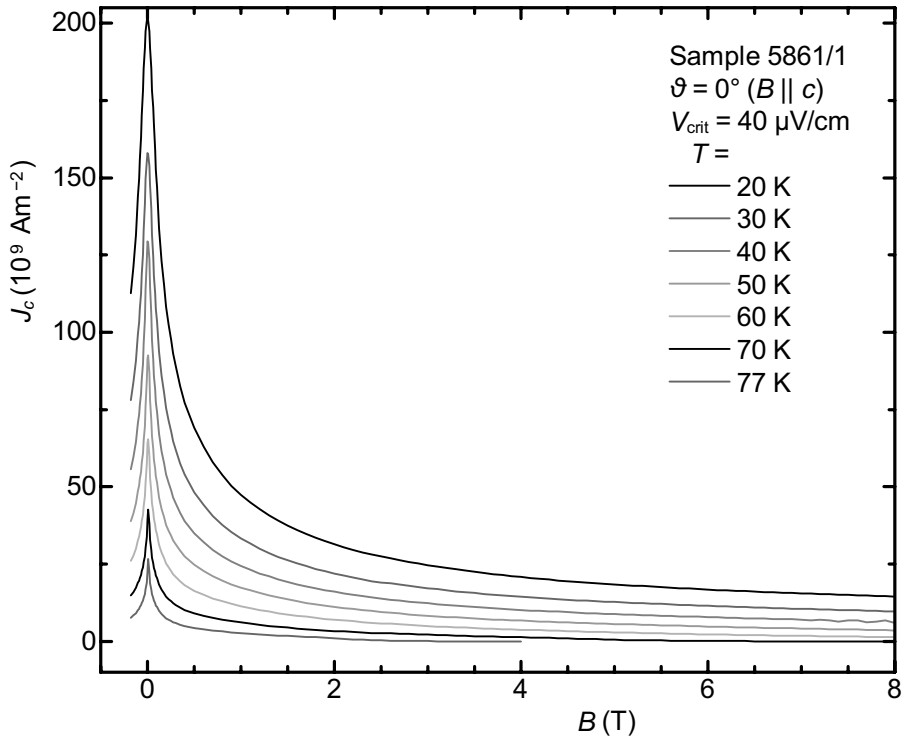

Figure 4.7
$J_c(B)$ of sample 5861/1 for temperatures from 20 K to 77 K. The field is applied parallel to the *c*-axis.

The deviation from a power law behaviour at small fields is possibly caused by self-field effects, which are discussed in section 4.2.2. J_c goes to zero when the applied field approaches the irreversibility line, which can be clearly seen for the data at 60, 70 and 77 K in Fig. 4.10. The observed current densities of the order of 10^{11} Am^{-2} are high but not unusual in YBCO thin films (Douwes *et al*., 1993; Mannhart *et al*., 1992; Pan, 1993).

The inverse square root behaviour has been observed by Brongersma (1996), who studied possible pinning models in detail and concluded that only the models with extended pinning centres parallel to the flux lines predict the observed behaviour (see section 2.5.1 and e.g. Blatter *et al*., 1994, IX STRONG PINNING). The collective pinning model for weak point defects predicts J_c to be proportional to B^{-1} in the single vortex limit, $\propto \exp(-B^{2/3})$ in the small bundle region and $\propto B^{-3}$ in the large bundle limit (Blatter *et al*., 1994, p 1207). In a flux line shear model, proposed for the HTS by Wördenweber (1992), where vortices move in a weak pinning percolation path, J_c is independent of B.

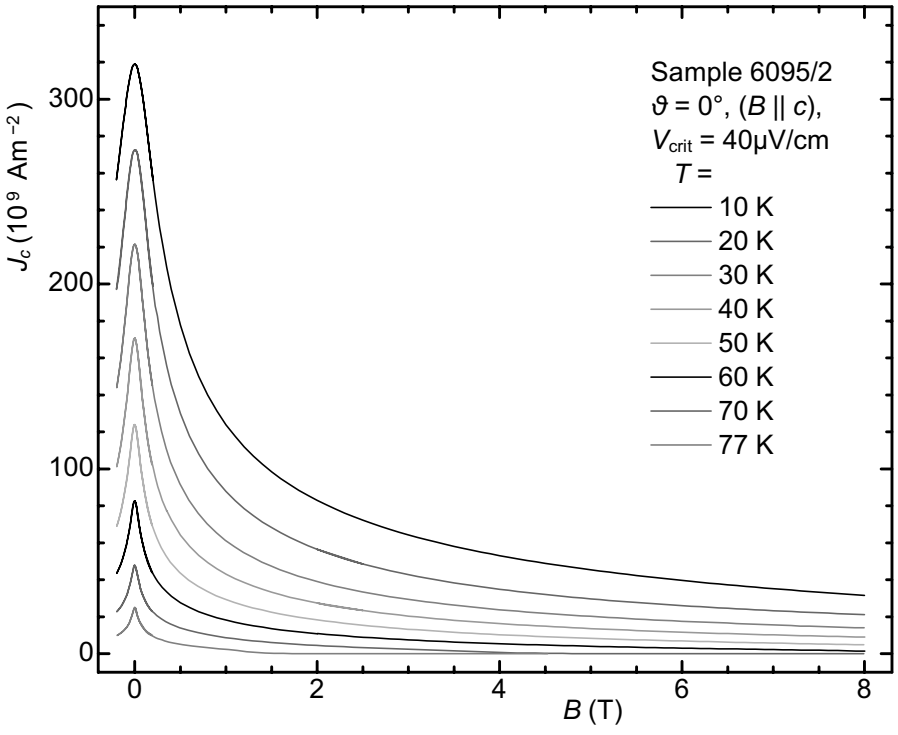

Figure 4.8
J_c (B) of sample 6095/2 for temperatures from 10 to 77 K. The field is applied parallel to the *c*-axis.

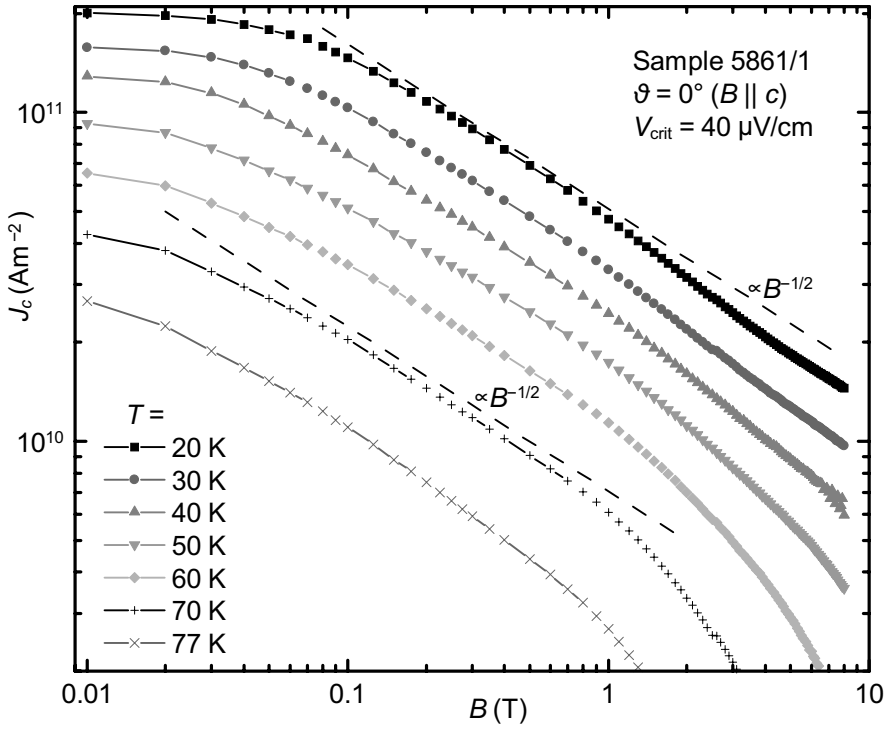

Figure 4.9
$J_c(B)$ of sample 5861/1 for temperatures from 20 K to 77 K. Same data as in Fig. 4.7 but plotted with logarithmically scaled axes.

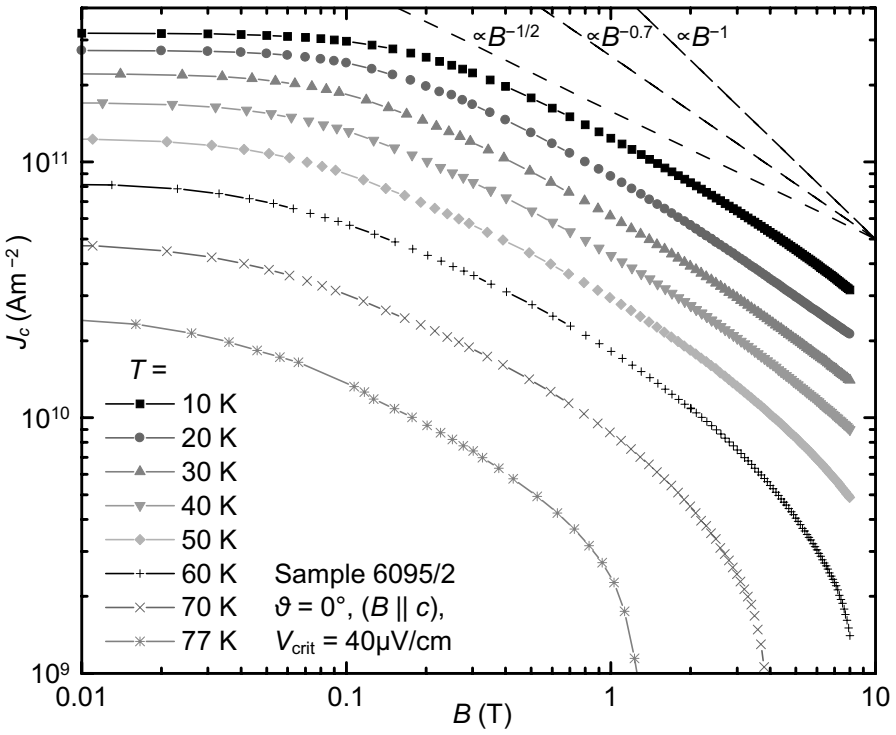

Figure 4.10
$J_c(B)$ of sample 6095/2 for temperatures from 10 K to 77 K. Same data as in Fig. 4.8 but plotted with logarithmically scaled axes.

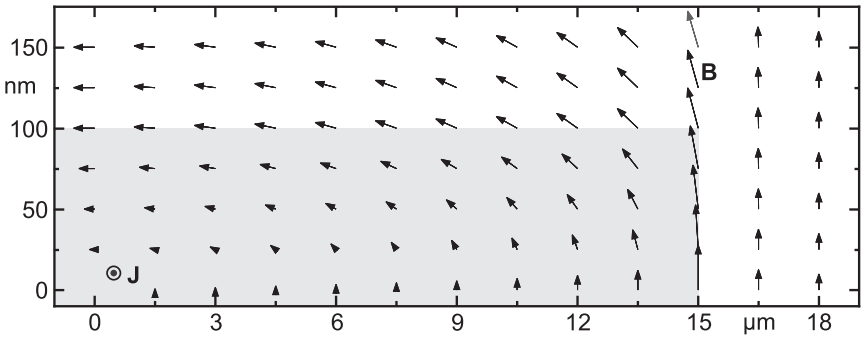

Figure 4.11
Magnetic field generated by current flowing in thin film (out of the drawing plane). The grey area marks a quarter cross-section of a 30 μm × 200 nm film. The strongest field occurs at the edge of the film, for y = 15 μm.

The observed $B^{-1/2}$ behaviour indicates that strong pinning is present in sputtered YBCO films, which is in agreement with the observed microstructure (see Fig. 3.1). It is interesting to note that in the derivation of their intrinsic pinning model Tachiki and Takahashi (1989a) also assumed that flux lines parallel c are pinned by extended defects, which led to the $J_c \propto (\cos \vartheta)^{-1/2}$ prediction (see section 4.1.4).

4.2.2 Self-field effects

Brongersma (1996) argues that the reason for the field independence of J_c at low fields could be the near optimal pinning of every flux line up to a matching field B_Φ above which excess flux lines have to be pinned by weaker pinning centres. His view is supported by the fact that the flux line density at the matching field he observes is close to the density of grains in his samples. This explanation, however, predicts a temperature independent B_Φ, contrary to the data plotted in Fig. 4.9. To consider the influence of the field generated by the high current densities themselves (self-field effect) the field distribution around a thin film was calculated assuming the local validity of the $B^{-1/2}$ behaviour even at very

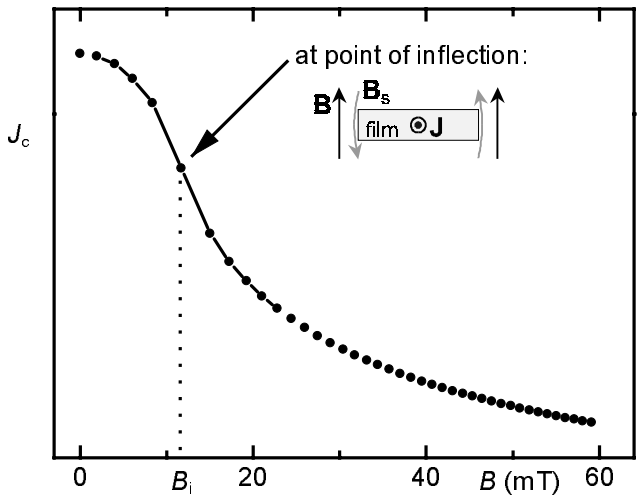

Figure 4.12
Schematic of $J_c(B)$ at low fields. When the self-field B_s (grey arrows) is equal to the applied field B (black arrows) the curvature of $J_c(B)$ changes. (Units are approximate.)

small values of B (Fig 4.11). Numerical simulations with a computer program led to the result that the point of inflection in the $J_c(B)$ curve occurs at an applied field B_i equal to the self-field at the edge of the thin film sample (see Fig. 4.12). B_i roughly marks the transition from the flat $J_c(B)$ behaviour at low fields ($\lesssim 0.1$ T) to the $B^{-1/2}$ dependence at higher fields. With increasing temperatures the critical current densities decrease and the self-field becomes smaller, leading to a reduced B_i, as observed and plotted in Figs. 4.8 to 4.9. Further calculations showed that, even if $J_c(B)$ is proportional to $B^{-\alpha}$ with other exponents α than 1/2, the point of inflection still occurs where the self-field is equal to the applied field.

4.2.3 Temperature dependence of J_c

Plots of J_c as a function of temperature ($B \parallel c$, Fig. 4.13) show a distinctly different behaviour for small fields than for strong fields. At small fields J_c decreases more or less linearly with T over the whole temperature range. At higher fields the straight lines in the logarithmic plot Fig. 4.14 suggest an exponential dependence at lower temperatures. An interpretation of this behaviour is difficult because many parameters change

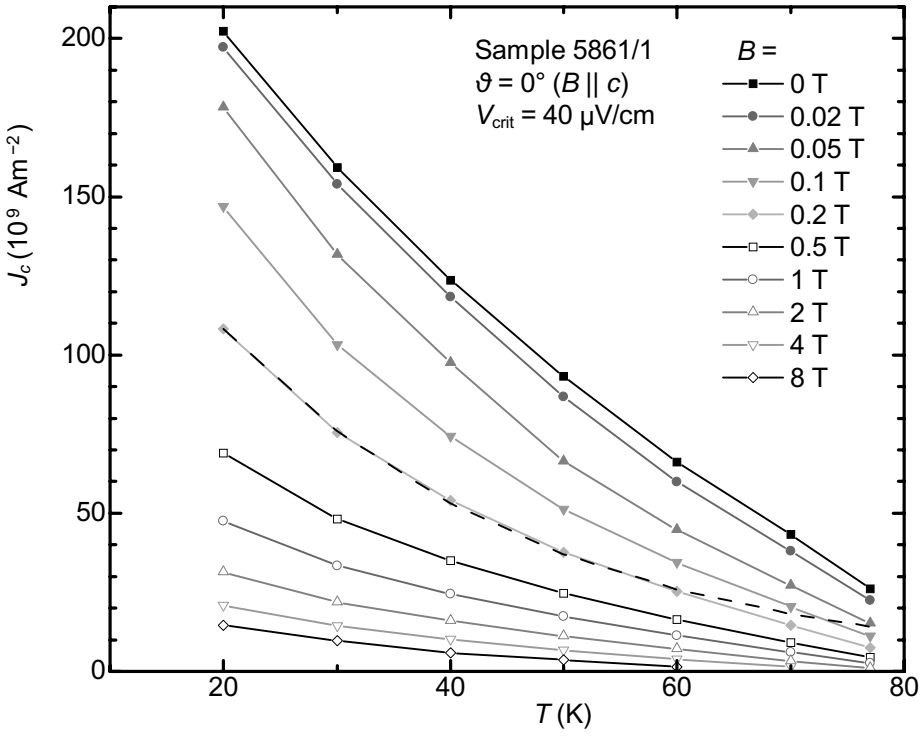

Figure 4.13
J_c of sample 5861/1 plotted as a function of temperature for several applied fields $B \parallel c$. The dashed line is an exponential fit to the 0.2 T curve.

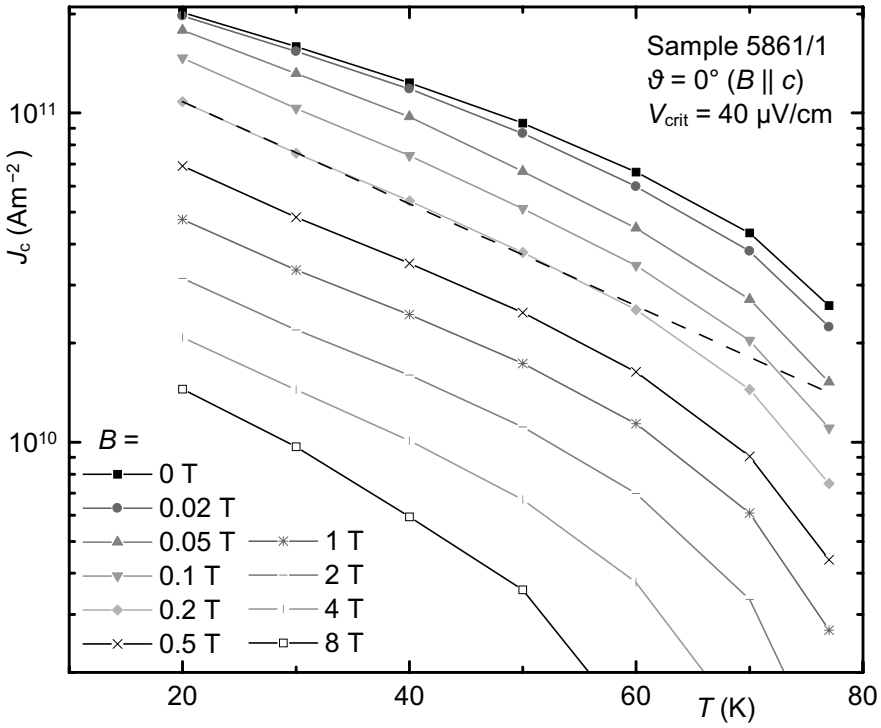

Figure 4.14
J_c as a function of T. Logarithmic plot of data in Fig. 4.13. The dashed line is an exponential fit to the 0.2 T curve.

with temperature and thermal activation has a further influence on the J_c plotted here, which was obtained by applying a voltage criterion. No further evaluation of the temperature dependence was attempted; the plots are shown here for completeness and to give an impression of the observed data.

4.3 ϑ-dependence of J_c – main features

To determine which of the models introduced at the beginning of this chapter describes the dependence of J_c on ϑ best, a large number of angular measurements were conducted on several *c*-axis films at temperatures ranging from 10 to 77 K and applied magnetic fields up to 8 T. The magnetic field was mostly rotated in the two main symmetry planes $\varphi = 90°$ and $\varphi = 0°$ (i.e. *yz*- and *xz*-planes; see Fig. 4.15) to restrict the many possible combinations of parameter values T, B and φ.

A careful analysis shows that the anisotropic GL theory is not sufficient to explain the obtained data. The 2D-model proposed by Kes (see section 4.1.5), on the other hand, describes the measured angular data accurately at low temperatures although deviations from the model increase at higher temperatures. This section compares the predictions

of the two main models for the ϑ-dependence of J_c, with the important result that the layering of YBCO has a direct influence on J_c. In section 4.4 the structure of flux lines in layered superconductors is therefore investigated in detail. A closer look at the ϑ-dependence of J_c and deviations from the 2D model follow in section 4.6.

4.3.1 General features

The geometries for ϑ scans with $\varphi = 90°$ and 0° are shown in Fig. 4.15. In the first case (Fig. 4.15a) the field remains normal to the current direction for all ϑ and the magnitude of the macroscopic Lorentz force is therefore angle-independent. The force components F_L^c and F_L^{ab} however do change with ϑ. In the second case (Fig. 4.15b) the field is rotated from parallel to the *c*-axis into the direction the current is flowing, where the macroscopic Lorentz force is 0. This case, $B \parallel J$, is often called the 'force free configuration'. The Lorentz force densities for the two configurations are

$$\varphi = 90°: \quad \mathbf{F}_L = \mathbf{J} \times \mathbf{B} = JB(\sin\vartheta\, \mathbf{e}_z - \cos\vartheta\, \mathbf{e}_y) = \mathbf{F}_L^c + \mathbf{F}_L^{ab} = \mathbf{J} \times B_y\, \mathbf{e}_y + \mathbf{J} \times B_z\, \mathbf{e}_z \qquad (4.5)$$

$$\varphi = 0°: \qquad \mathbf{F}_L = \mathbf{J} \times \mathbf{B} = -JB\cos\vartheta\, \mathbf{e}_y = \mathbf{F}_L^{ab} = \mathbf{J} \times B_z\, \mathbf{e}_z \qquad (4.6)$$

where $\mathbf{e}_y$ and $\mathbf{e}_z$ are unit vectors in *y* and *z* direction. The last equality in each line shows that B_y, the field component in *y*-direction, causes F_L^c, the force component parallel *c*, and B_z causes F_L^{ab}. Since the flux line structure in both configurations is exactly the same for any given angle ϑ, a comparison of the two cases directly reveals the influence of the Lorentz force F_L^c on J_c. More details about the influence of F_L^c can be found with experiments where φ is changed continuously at constant ϑ. Such measurements are presented in section 4.5.

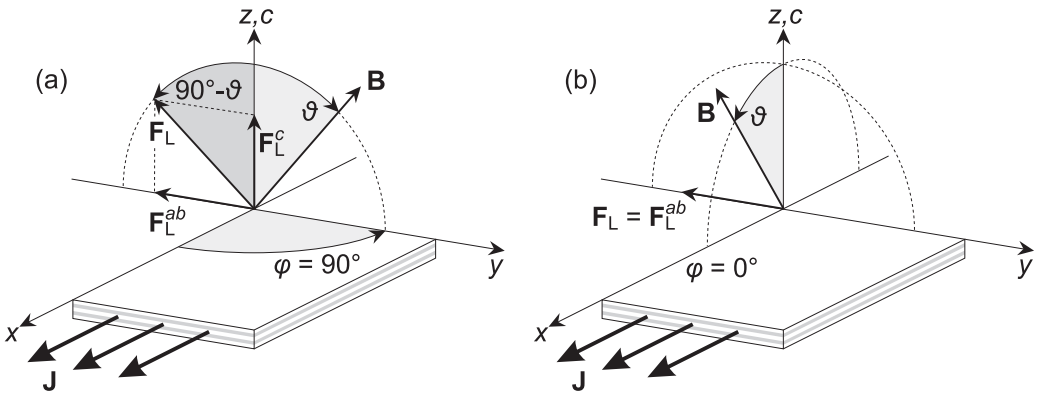

Figure 4.15
Geometry for ϑ-scans in the main symmetry planes. (a) $\varphi = 90°$ and (b) $\varphi = 0°$

Typical $J_c(\vartheta)$ measurements of a sample at 20 K are shown in Fig. 4.16 for both configurations with the characteristic feature of maxima at $\vartheta = 90°$, which are steep for higher fields. Whereas J_c drops by a factor of 15 from 0 to 8 Tesla at $\vartheta = 0°$ it nearly stays constant at $\vartheta = 90°$. In Fig. 4.17 the data is replotted as a function of B_y and B_z to visualise the full B dependence for $\varphi = 90°$. It is apparent that J_c changes much more with B_z (which corresponds to F_L^{ab}) than with B_y (F_L^c) although the magnitude of the total Lorentz force is constant for any given B. The striking difference clearly suggests that, in a first approximation, J_c is independent of B_y, which is predicted by the 2D model presented in section 4.1.5. A more detailed comparison of the two relevant models and the data follows in the next section.

4.3.2 2D model versus anisotropic GL-theory

Although equations (4.2) and (4.6) were derived with different assumptions, it is interesting to note that (4.6) reduces to (4.2) when $\varepsilon = 0$. Since ε is a constant in the anisotropic GL theory (~1/5 for YBCO) it strictly is not possible to make it variable. However, the following equations are used to interpolate between the 2D model and the

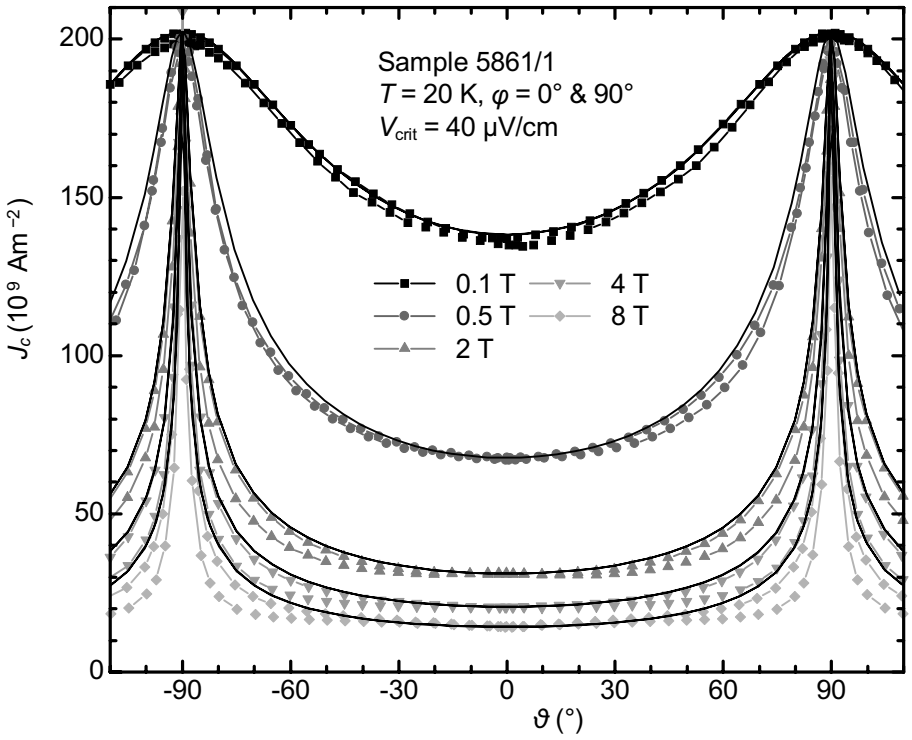

Figure 4.16
$J_c(\vartheta)$ of sample 5861/1 for applied fields from 0.1 T to 8 T for $\varphi = 0°$ and $\varphi = 90°$ at 20 K. The smaller J_c values for each field are for $\varphi = 90°$, the larger ones for $\varphi = 0°$. The solid lines are calculated using Equ. (4.2).

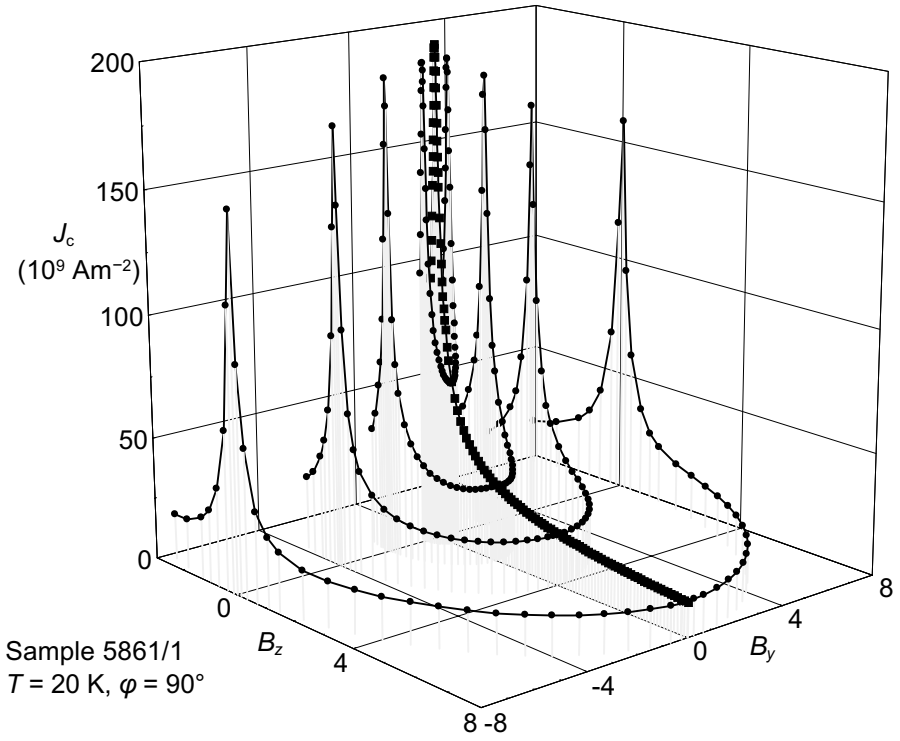

Figure 4.17
Angular J_c measurements at different fields (0.5, 2, 4 & 8 T) plotted as a function of B_y (parallel to the *ab*-plane) and B_z (parallel to the *c*-axis). In addition a measurement of $J_c(B, \vartheta = 0°) = J_c(B_z, B_y = 0)$ is shown (small squares).

anisotropic GL-theory in an attempt to determine which model better describes the ϑ dependence of J_c.

$$J_c(B, \vartheta) = J_c(\varepsilon'_\vartheta B, 0) \tag{4.7}$$

with

$$\varepsilon'_\vartheta = \sqrt{\cos^2 \vartheta + \varepsilon'^2 \sin^2 \vartheta} \tag{4.8}$$

where ε' varies between 0, corresponding to the 2D model, and ε for the anisotropic GL-theory as proposed by the scaling rule of Blatter et. al. (see section 4.1.6). Equation (4.7) predicts that J_c values measured at the field $\varepsilon'_\vartheta B$ applied in *c*-direction should also be observable for a field B applied at the angle ϑ.

Fig. 4.18 shows on the right a part of the B_yB_z-plane to illustrate the situation. The solid lines are lines of constant J_c, the shape of which has been calculated according to the two models. In the 2D model (Fig. 4.18b, $\varepsilon' = 0$) these lines are straight and parallel to the B_y axis, showing that J_c is independent of B_y. For all ε' values larger than 0 (c) the lines are ellipses with an aspect ratio of the major axes of 1:ε'. A ϑ-scan at constant B (dashed line) crosses the constant J_c lines. To evaluate the models, *two* J_c values on a line are compared. One is simply the J_c measured directly with the field B applied at the

angle ϑ (see arrows for example). The other is obtained when applying the (smaller) field $\varepsilon'_\vartheta B$ parallel to the B_z-axis (= *c*-axis). This corresponds to the points in Fig. 4.18 where the constant J_c lines intersect the B_z-axis. A plot of a measurement with $B \parallel c$ is shown on the left (Fig. 4.18a) from which the J_c of each line can be obtained.

The main difference between the J_c predictions of the two models occurs at $\vartheta = 90°$. $J_c(B, \vartheta = 90°)$ should be the zero field J_c for any B in the 2D model ($\varepsilon' = 0$), whereas the anisotropic GL theory ($\varepsilon' > 0$) predicts the same J_c value as the one obtained when the field $\varepsilon' B$ is applied parallel to the *c*-axis (compare bold contour in Fig. 4.18c). These two J_c values can be considerably different because J_c drops rapidly with small fields applied parallel to *c* (see plot in Fig. 4.18a). Both models show similar behaviour in the vicinity of $\vartheta = 0°$.

The symbols in Fig. 4.19 show $J_c(\vartheta)$ measurements at 20 K and 2 T for both $\varphi = 0°$ and $\varphi = 90°$. The solid and dashed lines were calculated with Equ. (4.7) and several values of ε' from $J_c(B \parallel c)$ measurements. It can be clearly seen that the curve for $\varepsilon' = 0$ describes the data for $\varphi = 0°$ accurately, but for $\varphi = 90°$ deviations occur in the range $50° \lesssim \vartheta \lesssim 85°$. Values of ε' larger than 0 do not result in a better description of the data, because J_c at $\vartheta = 90°$ is nearly as large as the zero field value. This strongly indicates that the 2D model is the more appropriate model to describe the ϑ dependence of J_c in *c*-axis YBCO films.

Although deviations from the 2D model are larger at higher temperatures (see section 4.6), the shapes of the data plots never resemble the predictions of the anisotropic GL-theory, nor do any other values of ε' improve the fit. This result clearly shows that the

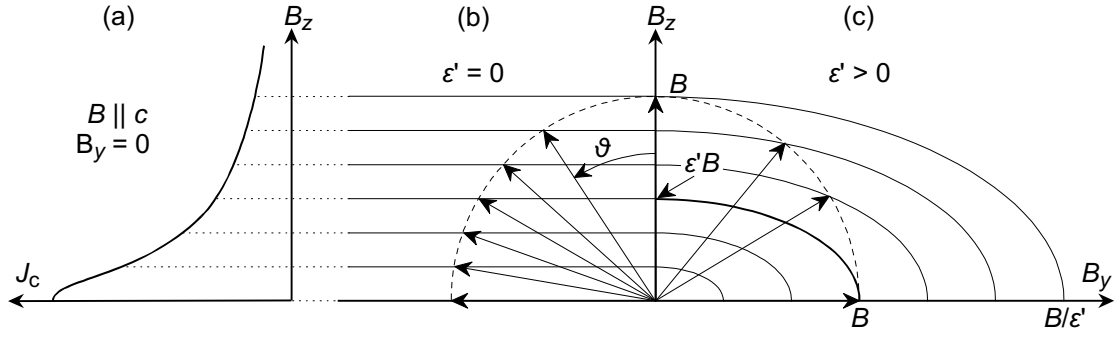

Figure 4.18
Schematic diagram of $J_c(B_z)$ (a) and a contour plot of J_c in the B_yB_z-plane (b,c) to illustrate the expected scaling according to the 2D model (b) and the anisotropic GL theory (c). The J_c values at the contour lines can, for example, be measured with $B \parallel c$ (a). The dashed semicircle shows a ϑ scan at constant field *B*.

intrinsic layering of YBCO not only generates the anisotropy of this material, but that it also has a direct and strong influence on the pinning of flux lines, as Tachiki and Takahashi and others expected. The 2D model is therefore subsequently used as a guideline in evaluating angular measurements of J_c.

Since the 2D model based on a layered structure succeeds to explain the observed $J_c(\vartheta)$ dependence, particularly at low temperatures, a detailed analysis of the flux line structure in layered superconductors is required to understand critical currents in YBCO. It follows in the next section. A closer look at the ϑ dependence of J_c continues in section 4.6.

4.4 Flux lines in layered superconductors

The concepts of flux lines in a stack of more or less coupled superconducting layers were developed by many researchers after it became clear that the newly discovered HTS have a layered crystal structure and ξ_c can be comparable to the layer spacing. The Lawrence Doniach theory is nearly always used as a starting point (see section 2.7). In layered superconductors flux lines are not straight but step shaped if ξ_c is small enough.

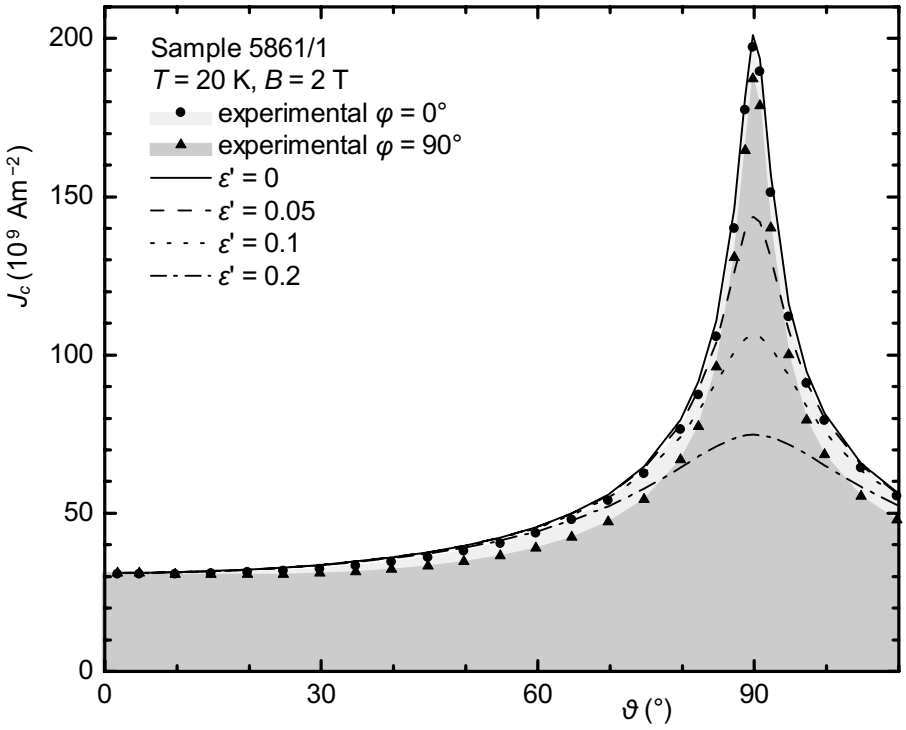

Figure 4.19
Comparison of $J_c(\vartheta)$ of sample 5861/1 at 20 K, 2 T, $\varphi = 0°$ and 90° with the 2D model ($\varepsilon' = 0$) and the anisotropic GL model for a range of ε' values.

The two distinct parts of the step are pancake vortices and vortex strings parallel to the *ab*-plane.

4.4.1 Pancakes and strings

Fig. 4.20 shows schematic drawings of flux lines penetrating a layered superconductor. At the left (Fig. 4.20a) the field is applied normal to the current direction ($\varphi = 90°$) and on the right $\varphi = 0°$. The two configurations correspond to the experimental geometries of Fig. 4.15. Depending on the ratio ξ_c/c the flux line strings parallel to the *ab*-plane are either more or less three dimensional Abrikosov vortices in the intrinsic pinning potential (see section 4.1.4) or Josephson vortices with little effect on the order parameter in the layers (section 4.1.5).

The discreteness of the layering has an important effect on the way a single flux line and the ensemble of all flux lines change when B or a field component (B_z or B_{ab}) are increased. Since the length of a pancake vortex is always c, the unit cell length in c-direction, the average string length w is directly connected to ϑ by $w = c \tan\vartheta$ (see Fig. 4.21). The pancake density (number of pancakes per unit area of a CuO_2 plane or number per unit volume) is determined by the field component B_z. As seen in the previous section, it is the parameter with the strongest influence on J_c. The string density is proportional to B_{ab} and the ratio of B_{ab}:B_z fixes the average string length: $w = c\, B_{ab}/B_z$.

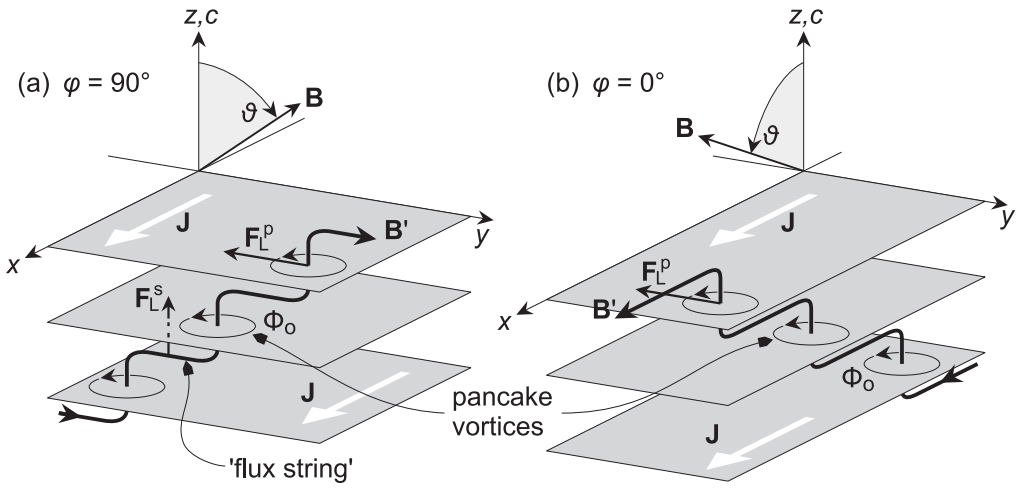

Figure 4.20
Details of flux lines penetrating layered superconductors. A vortex line can be regarded as a sequence of pancake vortices interconnected by Abrikosov vortices or Josephson strings, depending on the operating regime. Lorentz forces act on pancake vortices (F_L^p) and on the strings (F_L^s) for $\varphi = 90°$ (a) but only on the pancake vortices for $\varphi = 0°$ (b). (B' is the local field, B the field averaged over a few CuO layers. The small circles symbolise shielding currents of pancake vortices.)

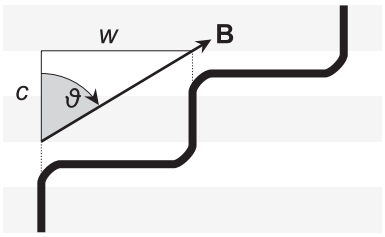

Figure 4.21
Relation between unit cell length c, string length w and ϑ: $w = c \tan \vartheta$.

Fig. 4.22 shows how the flux line lattice changes when B_z (a) or B_{ab} (b; B_y is chosen here for B_{ab}) are increased with other parameters remaining constant. In the first case the pancake density increases and the string length becomes shorter, yet the string density does not change. For the latter the string density and string length increase with constant pancake density. In case the field B is increased at constant ϑ (not shown), the string length w remains constant, but pancake and string density increase.

For $\vartheta = 0°$ ($w = 0$), the flux lines are parallel to the c-axis and the pancakes of each flux line are aligned. With increasing ϑ (increasing w) vortex strings parallel to the ab-plane start to appear. When the vortex strings become longer, adjacent pancakes are more and more decoupled, and thus the ability of strongly pinned pancakes to provide a pinning force to their neighbours diminishes. With increasing temperature this leads to deviations from the 2D model. A continuation of these arguments with further discussion of the ϑ dependence of J_c follows in section 4.6

4.4.2 Forces on pancakes and strings

In all hard type II superconductors two types of forces act on flux lines or flux line components, which are pinning forces originating from the interaction of the flux lines with

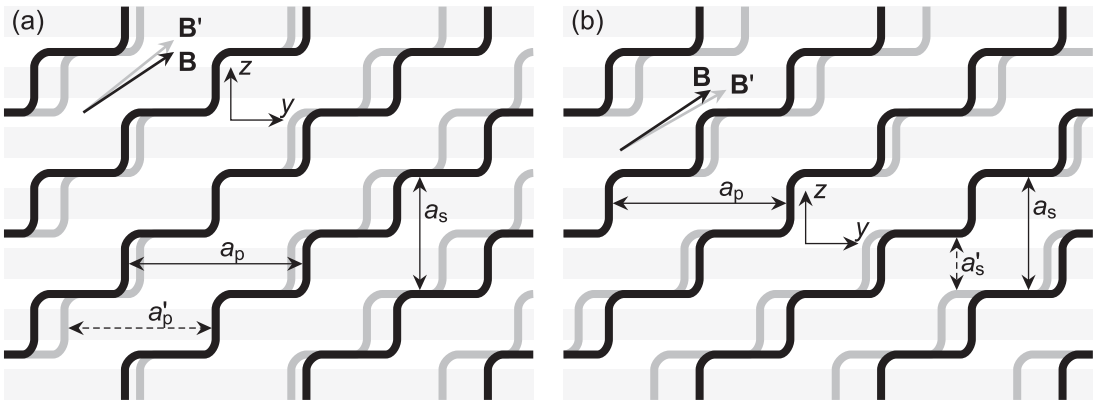

Figure 4.22
Schematic drawings of flux entering a sample with increasing B_z (a) and B_y (b). The black lines show the flux lines before the increase of B_z and B_y respectively, the dark grey lines after the increase. In the first case the average pancake spacing is reduced ($a_p \rightarrow a'_p$) while the string spacing stays constant (a_s). In the second case strings come closer ($a_s \rightarrow a'_s$) while a_p is constant. (In reality the flux lines never come as close as drawn.)

inhomogeneities in the crystal structure of the material and Lorentz forces caused by an applied transport current. The *critical* current is reached when the Lorentz force and the maximum pinning force in opposite direction of the Lorentz force are in equilibrium. A further increase of J unavoidably leads to flux line movement and dissipation.

4.4.2.1 Lorentz forces

In Fig. 4.20 forces on pancakes and strings are drawn for tilted flux lines in *c*-axis films with $\varphi = 90°$ (a) and $\varphi = 0°$ (b). They are related to the macroscopic forces of Fig. 4.15 in the following way: The force density on all pancakes is equal to F_L^{ab}. Since this force density and the (volume) density of pancakes are both proportional to B_z, the force on a single pancake vortex is $F_L^p = c\,\Phi_0 J$. It only depends on J. F_L^p is always parallel to the y-axis because it has to be normal to the current direction, which defines the x-axis.

The flux line strings parallel to the *ab*-plane can be normal to the current direction (Fig. 4.20a, $\varphi = 90°$), parallel (Fig. 4.20b, $\varphi = 0°$) or at an intermediate angle. Since the Lorentz force is proportional to the vector product between **B** and **J**, it depends on the sine of the angle between them, which is φ (see Fig. 4.3). Thus F_L^s, the force on a unit length of string, is maximal for $\varphi = 90°$ and zero for $\varphi = 0°$. It is always parallel to the z-axis and presses the strings against the intrinsic pinning potential. The force density on all strings is F_L^c (see Fig. 4.15) and the force per unit length on a string is $F_L^s = \Phi_0 J \sin\varphi$.

4.4.2.2 Pinning forces

Since only core pinning is practically relevant in the HTS, the pinning of pancakes is caused by changes of the order parameter in the CuO_2 planes, originating from oxygen defects, twin planes, and many other types of disturbances of the crystal lattice. On average the pinning forces are equal in all directions of the *ab*-plane (except for coherently directed defects; see chapter 6) and independent of the direction of the flux line strings (i.e. φ; see section 4.4.3).

For the flux line strings parallel to the *ab*-plane, pinning forces in *c*-direction are fundamentally different from pinning forces in the *ab*-plane. The former are the intrinsic pinning forces provided by the (coherent) layering. They can be very strong, particularly at low temperatures, as the validity of the 2D model shows.

Pinning forces in the *ab*-plane on the other hand are caused by defects, just like for the pancakes. However, since the order parameter between the CuO_2 layers is already reduced, pinning potentials are shallower and maximal pinning forces are smaller than for the pancakes. In *c*-axis films no current – or current component – can flow in *c*-direction and it is therefore impossible to exert a Lorentz force parallel to the *ab*-plane on the strings, which could probe the in-plane pinning force on strings directly (For experiments with a *c*-component of *J*, see Berghuis *et al*., 1997). The possible influence of the in-plane string pinning force on J_c in the $\varphi = 0°$ configuration is further considered in section 4.5.2.

4.4.3 A model of a pancake vortex

In order to gain more insight into the pinning behaviour of flux lines in layered superconductors, a simple model of a flux line located in a defect was developed. The starting point is a hypothetical potential, which is modulated in *c*-direction to reproduce the layers and reduced around a point in a CuO_2 layer to simulate a pancake pin. With some assumptions, equilibrium positions for a flux line in this potential are found for various current densities, among them a maximum current density, which is J_c. Further assumptions allow the introduction of the angle φ into the model, and finally a dependence of J_c on φ is obtained, which is compared to experiments in section 4.5.

The model is based on pinning in the single vortex limit. To extend the model to the collective pinning regime further development work would be needed.

4.4.3.1 The potential

The amplitude of the order parameter squared ($|\psi|^2$) is proportional to the condensation energy in a superconductor. If a flux line is passing through a sample, the order parameter is suppressed at the core location and with it the condensation energy. Thus the system is in a higher energy state than without the flux line. It is therefore possible to define a potential for line elements of a flux line, which is simply proportional to $|\psi|^2$. If a line element is located at a position with a high potential, the loss in condensation energy of the system will be large. In a sample without current, the flux lines will therefore be located in the minima of the potential.

A contour plot of the cross section of the potential U used in the following simulation is shown in Fig. 4.23. The equation defining U is

$$U(x,y,z) = 8 + 20\left(1 - 0.8\,\Phi\left(5 - |z|\right)\exp\left(-\frac{x^2+y^2}{4^2}\right)\right)\cos^2\left(\frac{\pi\cdot z}{2\cdot 5}\right) \qquad (4.9)$$

with Φ the unit step function. The cosine factor generates the intrinsic modulation of the potential in z-direction, whereas the exponential produces the pancake pinning site at the origin (see saddle point in Fig. 4.23). To limit the disturbance to only one CuO_2 layer, the term is cut off with the step function at $|z| = 5$. The potential has cylindrical symmetry. The particular form of Equ. (4.9) has been chosen because it reproduces the desired features of intrinsic modulation and the pancake pin and it is mathematically simple.

4.4.3.2 Force balance of line elements and equilibrium configurations

In an equilibrium configuration of a flux line (i.e. it does not move) the sum of all forces on each line element has to be zero. The three forces acting are the Lorentz force, the pinning force which is determined by the gradient of the potential and the force of the two neighbouring line elements arising from the line tension (which is proportional to U). Since the neighbour elements pull in (roughly) opposite direction, the net force of the two is only proportional to the curvature of the flux line at that location. Now it is possible to resolve the force balance equation to determine the curvature of the flux line at each point from the Lorentz force and the gradient of the potential.

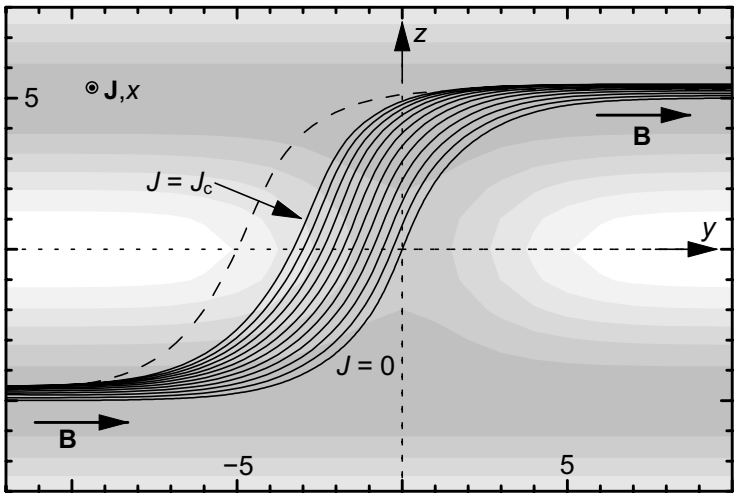

Figure 4.23
Pinning potential with flux line in equilibrium at several current densities. With increasing J the flux line moves left. Solid lines show stable configurations for $0 \le J < J_c$. The dashed line shows an unstable equilibrium position with $J > J_c$. (Potential maxima are white, minima dark grey.)

To find an equilibrium configuration of a complete flux line, an initial line element with a position y_0 on the y-axis is

chosen and the location of the two neighbour elements determined by using the curvature calculated for this position. Iteration of these steps leads to a flux line with any desired length. Two parameters remain to influence the shape of the flux line: the orientation of the starting element at y_o (i.e. the angle at which the flux line cuts the y-axis) and the current density J. These two degrees of freedom are used to adjust the flux line such that it runs parallel to the y-axis (with zero curvature), pressed against the intrinsic pinning potential, in the corners of Fig. 4.23. This is the boundary condition to meet.

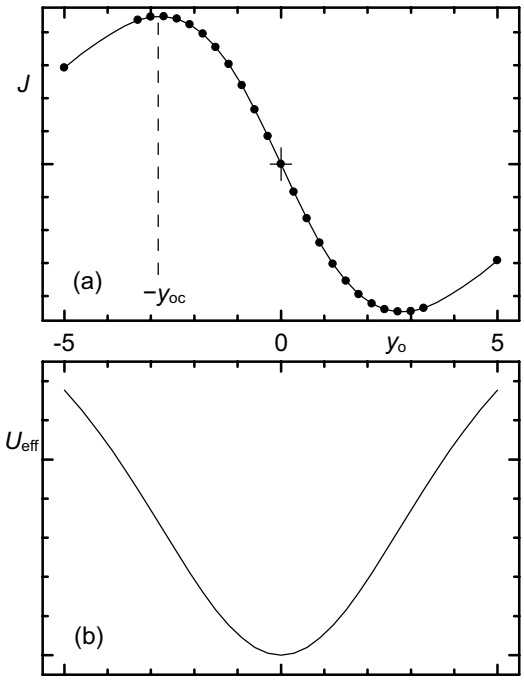

Figure 4.24
Current J to keep the flux line in equilibrium at position y_o (a) and effective potential calculated from different flux line positions (b). (The values for $y_o < 0$ are obtained by using the symmetry of the potential.)

A repetition of the procedure with different starting points y_o results in the configurations shown by the lines in Fig. 4.23 and a table relating J to y_o. Inversely it is possible to find an equilibrium position of the flux line for a given current density. Fig. 4.24a shows the relation between J and y_o with the expected maximum of J, which is located at $y_o = \pm y_{oc}$. The maximum J is the critical current density of the pancake pinning centre. Although there are equilibrium positions with $|y_o| > y_{oc}$, they are not *stable*. If, for instance, the dashed line in Fig. 4.23 only slightly moves to the left, the current exceeds the equilibrium current and the 'pancake' accelerates. Only for $J < J_c$ and $|y_o| < y_{oc}$ stable equilibrium configurations are available. Integration of U along a flux line section crossing the y-axis at y_o leads to the effective pinning potential U_{eff} (see Fig. 4.24b; compare Equ. (4.10)), which has points of inflection at $\pm y_{oc}$. In this last step it is assumed that y_o is an appropriate variable to parameterise the different flux line configurations.

4.4.3.3 Stiff flux line and effective potential

It is interesting to note that the shape of the flux line changes very little when the current increases from 0 to J_c (see Fig. 4.23). The flux line in equilibrium seems to be 'stiff'. In

a first approximation it appears therefore only necessary to use a single vector **t**, describing the transposition of the flux line from the $J = 0$ location, in order to find all other equilibrium configurations. Not all possible vectors **t** describe an equilibrium configuration, but it is assumed that for any current density in the *ab*-plane below J_c a transposition **t** can be found to reach the corresponding stable equilibrium flux line position.

So far only the mathematically simple two dimensional case has been considered, where **J** is normal to all flux line elements, i.e. $\varphi = 90°$ (In Fig. 4.23 the flux lines are in the drawing plane and **J** is pointing out of it.). The general case with arbitrary φ is substantially more difficult to calculate, although in principle not different. Avoiding this complication the stiff flux line assumption is used here to obtain an effective potential U_{eff}, which depends on the three components of the transposition vector. From this effective potential an effective maximum pinning force can be calculated, which, balanced to the correct Lorentz force, results in J_c for arbitrary angles φ.

U_{eff} is calculated by transposing the flux line from its position at the origin by **t** and integrating U along the line:

$$U_{\text{eff}}(\mathbf{t}) = \frac{1}{L}\int_L U(\mathbf{f}(\ell) + \mathbf{t})\,d\ell \tag{4.10}$$

with **t** the transposition vector, $\mathbf{f}(\ell)$ a parameterised description of the flux line at zero current and L the length of the segment. L has to be large enough for the segment to reach into an area undisturbed by the pancake pinning potential (about the length shown in Fig. 4.23). A schematic of transposed flux lines is shown in Fig. 4.25. The grey, cloud-like area symbolises the potential of the CuO layer with the pancake pin (white hole). The fading of the flux lines should hint that they dip into the potential.

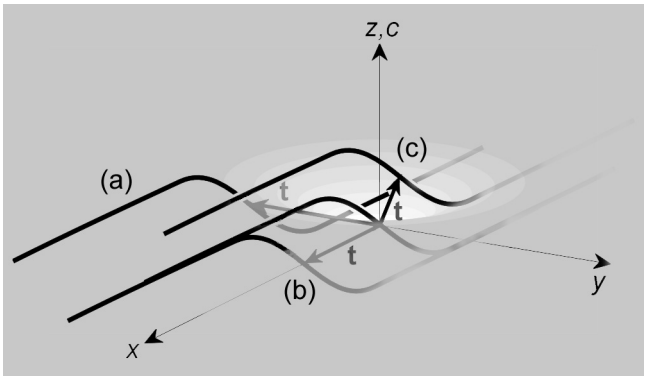

Figure 4.25
Schematic of flux line in a pancake pinning site in the zero current equilibrium configuration (the line passing through the origin) and transposed by three vectors **t** in $-y$-direction (a), x-direction (b) and in an

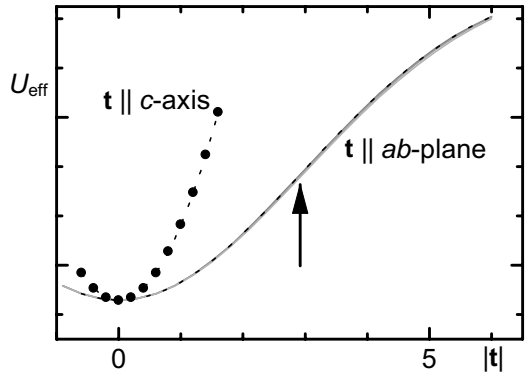

Figure 4.26
Effective potential as a function of t (= |**t**|) for several directions of **t**. The dotted lines are fits to Equ. (4.11).

Evaluating Equ. (4.10) for several directions of **t** within the *ab*-plane reveals that U_{eff} is nearly identical for all such directions. The three grey lines in Fig. 4.26 were calculated for **t** || $\mathbf{B}_{ab}$ ($\mathbf{B}_{ab}$ is the projection of **B** into the *ab*-plane), **t** ⊥ $\mathbf{B}_{ab}$ and at 45° in between. All three lines practically coincide. This result is not trivial because the cylindrical symmetry of the potential U is broken by the sloping shape of the flux line, which enters in Equ. (4.10). When the flux line is moved in *c*-direction on the other hand (**t** || *c*-axis), U_{eff} rises much faster, as the circular symbols in Fig. 4.26 show. In this case the flux line is moved against the intrinsic pinning force, which is stronger than the pinning force of the defect (the pancake pinning site at the origin). All the curves in Fig. 4.26 can be accurately fitted to a function, which is similar to the one describing the defect part in Equ. (4.9) ('negative Gaussian') such that the complete functional dependence of U_{eff} can be approximated in the vicinity of $t = 0$ by:

$$U_{eff} = U_0\left(1-\exp\left(-\frac{t_x^2+t_y^2}{2\,h_{ab}^2}-\frac{t_z^2}{2\,h_c^2}\right)\right) \qquad (4.11)$$

U_{eff}**(t)** has cylindrical symmetry as explained above. The two parameters h_{ab} and h_c describe the width and steepness of U_{eff}: The smaller h the narrower and steeper is U_{eff}. At $t = h$ the potential has a point of inflection, which is important because it is also the point with the steepest slope of U_{eff} (see arrow in Fig. 4.26). The values of h for the potential chosen in Equ. (4.9) are: $h_{ab} = 2.95$ and $h_c = 1.33$. They were found by fitting the data in Fig. 4.26 to Equ. (4.11) (see dotted lines).

4.4.3.4 Lorentz and pinning forces - critical currents

With the simplified form of the effective potential (Equ. (4.11)), it is now fairly straight forward to calculate the critical current of the pancake pin as a function of φ. For this purpose it is necessary to find the direction the Lorentz force is pulling the flux line and the maximum pinning force in that direction.

The Lorentz force on any flux line element is always lying within the *yz*-plane, because **J** is parallel to the *x*-axis (see also Fig. 4.15). $\mathbf{F}_\mathrm{L}^y$ only depends on the projection of the flux line on the *z*-axis, which is the layer spacing *c* (unit cell length), and *J*. Equally $\mathbf{F}_\mathrm{L}^z$ depends on *J* and on the projection of the length of flux line used here on the *y*-axis. The latter is proportional to $\sin\varphi$. In summary the two components are:

$$\mathbf{F}_\mathrm{L}^y = J\,\Phi_\mathrm{o}\,c \tag{4.12a}$$

$$\mathbf{F}_\mathrm{L}^z = J\,\Phi_\mathrm{o}\,L_{ab}\sin\varphi \tag{4.12b}$$

L_{ab} is the length of the projection of the flux line section onto the *ab*-plane. It is of the order of the dimensions of the pancake pin parallel to the *ab*-plane. Note that for a given angle φ the ratio between $\mathbf{F}_\mathrm{L}^y$ and $\mathbf{F}_\mathrm{L}^z$ is constant and independent of *J*.

The pinning force on the flux line section is independent of φ, because U_eff is cylindrically symmetric. Fig. 4.27 shows a 3D plot and a contour plot of U_eff as a function of t_y and t_z. The ellipses in plot (b) are equipotentials to which the gradient has to be normal. The pinning force on the flux line section is equal to the gradient of U_eff, but pointing in the opposite direction: $\mathbf{F}_\mathrm{p} = -\mathrm{grad}\,U_\mathrm{eff}$. Locations for which $\mathbf{F}_\mathrm{p}$ is pointing in the same direction lie on a straight line through the origin (see grey line in Fig. 4.27b), which is *not* parallel to $\mathbf{F}_\mathrm{p}$. The polar angles of the gradient (ϑ') and the line (θ') are related by $\tan\theta' = (h_{ab}/h_c)^2 \tan\vartheta'$. Moving along the line starting from the origin, $\mathbf{F}_\mathrm{p}$ increases until a maximum is reached ($\mathbf{F}_\mathrm{p}^\mathrm{max}$), which is the largest pinning force the potential can provide in the direction of $\mathbf{F}_\mathrm{p}$. In other words, $-\mathbf{F}_\mathrm{p}^\mathrm{max}$ is equal to the maximum gradient of the potential for a given gradient direction.

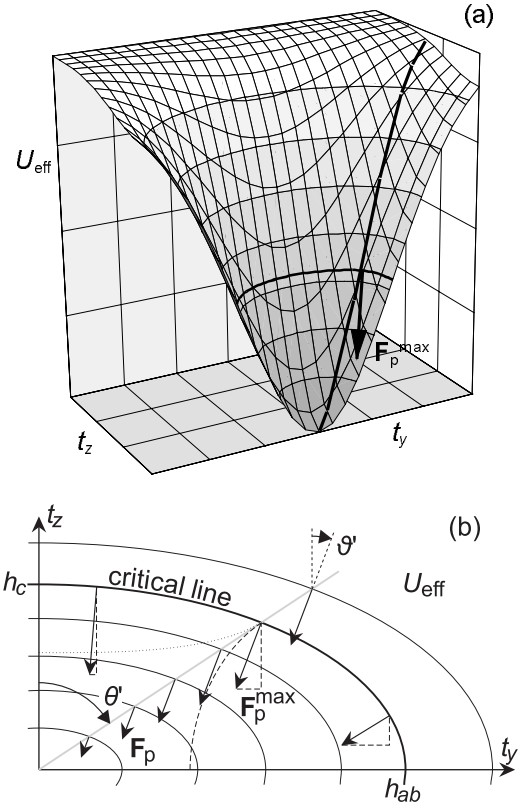

Figure 4.27
3D (a) and contour (b) plots of U_eff ($t_x = 0$). The flux line moves along the straight line (polar angle θ') when the Lorentz force pulls in the opposite direction of the pinning force which is marked by the arrows.

The maximum gradients for all directions are located on the bold line in Fig. 4.27b. This line marks the border between stable equilibrium configurations of the flux line (closer to the origin) and unstable equilibrium configurations ('outside'). Since the force balance between the maximum pinning force and the Lorentz force defines J_c, the border line can also be called the critical line.

The following explicit calculation illustrates the above arguments. From Equ. (4.11) the two components of the gradient are:

$$\frac{\partial U_{\text{eff}}}{\partial t_y} = \frac{U_0 t_y}{h_{ab}^2} \exp\left(-\frac{t_y^2}{2h_{ab}^2} - \frac{t_z^2}{2h_c^2} \right) = -F_p^y \tag{4.13a}$$

and

$$\frac{\partial U_{\text{eff}}}{\partial t_z} = \frac{U_0 t_z}{h_c^2} \exp\left(-\frac{t_y^2}{2h_{ab}^2} - \frac{t_z^2}{2h_c^2} \right) = -F_p^z \tag{4.13b}$$

The critical line is defined by the maximum gradient at constant θ' (or equivalently constant ϑ'). In Equ. (4.13) t_y is therefore substituted by $t\sin\theta'$ and t_z by $t\cos\theta'$ to calculate F_p^2 as a function of t and θ'. Finally the location of the maximum F_p is obtained by calculating the derivative of F_p^2 in respect to t and equating it to 0 (The location t_c of the maximum of F_p and of F_p^2 is the same, but the derivative of F_p^2 is easier to calculate.):

$$\frac{\partial F_p^2}{\partial t} = 2U_0^2 \left(t - t^3 \left(\frac{\sin^2\theta'}{h_{ab}^2} + \frac{\cos^2\theta'}{h_c^2} \right) \right) \left(\frac{\sin^2\theta'}{h_{ab}^4} + \frac{\cos^2\theta'}{h_c^4} \right) \exp\left(-\frac{t^2\sin^2\theta'}{h_{ab}^2} - \frac{t^2\cos^2\theta'}{h_c^2} \right)$$

$$\frac{\partial F_p^2}{\partial t} = 0 \quad \Rightarrow \quad t_c = \left(\frac{\sin^2\theta'}{h_{ab}^2} + \frac{\cos^2\theta'}{h_c^2} \right)^{-1/2} \tag{4.14a) and (4.14b}$$

Equ. (4.14b) is the equation of an ellipsis in polar coordinates with the semi-axes h_{ab} and h_c (see Fig. 4.27b). Returning to the Cartesian components t_y and t_z, the critical ellipsis is

$$\frac{t_{cy}^2}{h_{ab}^2} + \frac{t_{cz}^2}{h_c^2} = 1, \tag{4.15}$$

where t_{cy} and t_{cz} are the components of t_c. Now it is possible to balance the Lorentz force with the critical pinning force and determine J_c. The components of the critical pinning force obtained from Equ. (4.13) with Equ. (4.15) are:

$$F_{\mathrm{pc}}^{y} = -\frac{U_0 t_{\mathrm{c}y}}{h_{ab}^2} e^{-1/2} \qquad \text{and} \qquad F_{\mathrm{pc}}^{z} = -\frac{U_0 t_{\mathrm{c}z}}{h_c^2} e^{-1/2} \tag{4.16}$$

With the force balance equations $F_{\mathrm{L}}^{y} + F_{\mathrm{pc}}^{y} = 0$ and $F_{\mathrm{L}}^{z} + F_{\mathrm{pc}}^{z} = 0$, Equs. (4.12) and (4.16) and resolving to $t_{\mathrm{c}y}$ and $t_{\mathrm{c}z}$ one gets

$$t_{\mathrm{c}y} = \frac{\Phi_0 e^{1/2} J_{\mathrm{c}} h_{ab}^2 c}{U_0} \qquad \text{and} \qquad t_{\mathrm{c}z} = \frac{\Phi_0 e^{1/2} J_{\mathrm{c}} h_c^2 L_{ab} \sin\varphi}{U_0}. \tag{4.17}$$

Finally Equ. (4.17) can be inserted into Equ. (4.15) and resolved to J_{c}:

$$J_{\mathrm{c}} = \frac{U_0}{e^{1/2}\Phi_0} \left(h_{ab}^2 c^2 + h_c^2 L_{ab}^2 \sin^2\varphi \right)^{-1/2} \tag{4.18}$$

Since the flux line structure and the parameters in Equ. (4.18) are independent of φ, a direct experimental test of Equ. (4.18) is possible with φ-rotation measurements. The experiments presented in section 4.5 show that it describes the data surprisingly well in a wide temperature and field regime. Equ. (4.18) is the main result of the pancake pin model developed in this section.

4.4.3.5 Discussion

Equ. (4.18) shows that J_{c} is smaller for $\varphi = 90°$ than for $\varphi = 0°$. The only difference between the two configurations is an additional Lorentz force on the flux line section in *c*-direction (see also section 4.4.1) in the $\varphi = 90°$ case. This force reduces J_{c}, as a careful analysis of the potential U_{eff} (see Fig. 4.27) reveals. Although the absolute value of F_{pc} increases with decreasing θ', the component F_{pc}^{y} decreases (Compare the three arrows originating on the critical line in Fig. 4.28b and their components marked by straight dashed lines.). This means that the Lorentz force in *y*-direction has to overcome the maximum pinning force in *y*-direction when there is no Lorentz force on the flux line section in *c*-direction. Although the intrinsic pinning force in *c*-direction is much stronger than the pinning force on the pancakes within the *ab*-plane, a Lorentz force in *c*-direction 'helps' the pancake out of the pinning potential at a lower current density than if there is no such force.

The dashed curve in Fig. 4.28b is a line of constant F_{p}^{y} and the dotted curve a line of constant F_{p}^{z}. It can be seen that F_{p}^{y} on the former is smaller than at the point ($t_y = h_{ab}$,

$t_z = 0$), where it reaches it's maximum. The dotted and the dashed curves touch the grey line on the critical line, showing that $\mathbf{F}_p$ does not change there when moving along the grey line: it reached it's maximum (in that particular direction).

Going back to the simulation of the complete flux line section (without the stiff flux line assumption), the movement parallel to the *c*-axis is apparent in the $\varphi = 90°$ case (see Fig. 4.23) and J_c is reached at a smaller value than if the flux line moves exclusively in $-y$-direction. This can be directly verified by evaluating Equ. (4.10) for the calculated positions shown in Fig. 4.23 and for transpositions **t** parallel to the *ab*-plane. The result that a Lorentz force component in *c*-direction reduces J_c is therefore independent of the stiff flux line assumption and the effective potential chosen in Equ. (4.11).

It is interesting to compare Equ. (4.18) to the φ dependence of J_c in an isotropic and not layered superconductor. In this case the maximum pinning force is equal in all directions normal to **B**. With a standard Lorentz force argument J_c should then be inversely proportional to the sine of the angle α between **J** and **B**, which, expressed with ϑ and φ, leads to

$$J_c \propto \sin^{-1}\alpha = (\cos^2\vartheta + \sin^2\vartheta \sin^2\varphi)^{-1/2}. \tag{4.19}$$

For constant ϑ Equ. (4.19) can lead to the same functional dependence as Equ. (4.18), but generally this is not the case because the coefficients are rigidly fixed to $\cos^2\vartheta$ and $\sin^2\vartheta$ in Equ. (4.19), whereas they take the different pinning forces of the pancake pin (h_{ab}) and the intrinsic pinning (h_c) as well as the shape of the flux line section (c and L_{ab}) into account in Equ. (4.18).

4.4.4 Summary of flux lines in layered superconductors

Section 4.4 presented concepts of flux lines and the forces on them in layered superconductors. After the introduction of flux pancakes and flux line strings parallel to the *ab*-plane, their different modes of entry into a sample were studied when B, B_z or B_{ab} are increased, which arise from the discreteness of the layers. Here the important parameter w was introduced which describes the displacement of neighbouring pancakes of a flux line. A description of Lorentz and pinning forces on pancakes and flux line strings followed in section 4.4.2.

Finally a model of a flux pancake was developed to gain additional physical insight into the shape of flux lines in equilibrium and how a Lorentz force originating from an applied transport current moves the flux line. Using a number of simplifications it was found that a Lorentz force in *c*-direction can reduce the critical current density of a pancake pin, even when that Lorentz force is much smaller than the intrinsic pinning force. The model also allowed the derivation of a prediction for the φ-dependence of J_c, which is compared to experimental data in the following section.

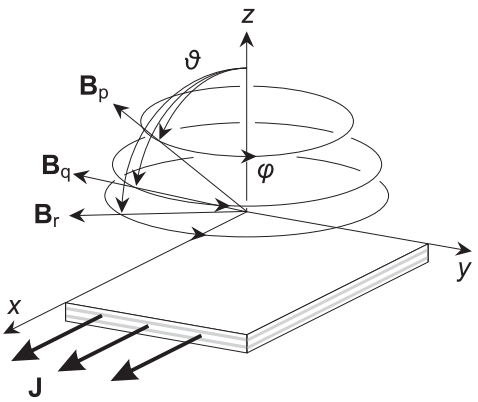

Figure 4.28
Geometry of $J_c(\varphi)$ measurements at various angles ϑ.

4.5 φ-dependence of J_c

The majority of researchers who investigated the J_c dependence in YBCO films on the direction of an applied field, changed only the angle ϑ in their experiments. Most chose the geometry such that the field was always normal to the current direction, which corresponds to $\varphi = 90°$, but a few also investigated the $\varphi = 0°$ configuration (Adrian *et al*., 1993; Jakob *et al*., 1993; Walkenhorst *et al*., 1991; Aomine *et al*., 1993). On the φ-dependence of transport properties in HTS only a very small number of experiments have been published. Iye *et al*. (1989) found ρ to be independent of φ in BiSCCO films ($\vartheta = 90°$, see section 4.1.5). For $J_c(\varphi)$ measurements at 77 K Nishizaki *et al*. (1991a; 1991b; 1993) found a reasonable fit in

$$J_c(\varphi) = \frac{A_p}{B|\sin\varphi| + A_p/J_c(0°)}, \tag{4.20}$$

where A_p is a constant 'pinning force parameter' ($\vartheta = 90°$).

Measurements at constant ϑ and varying φ are interesting because they allow a continuous increase of the Lorentz force component parallel to the *c*-axis on the flux line (F_L^s in Fig. 4.20) with an unchanged flux line structure. The geometry of φ-scans is shown in Fig. 4.28.

4.5.1 Experiments

The model of a flux line in a pancake pin developed in the previous section led to Equ. (4.18) describing the φ-dependence of J_c. When the parameters in Equ. (4.18) are adapted to fit the experimental data at $\varphi = 0°$ and $\varphi = 90°$ (at constant B and ϑ) the equation becomes

$$J_c(\varphi) = \frac{J_c(0°)}{\sqrt{1+\left(\frac{J_c^2(0°)}{J_c^2(90°)}-1\right)\sin^2\varphi}} = \frac{1}{\sqrt{\frac{\cos^2\varphi}{J_c^2(0°)}+\frac{\sin^2\varphi}{J_c^2(90°)}}} \tag{4.21}$$

All $J_c(\varphi)$-measurements conducted on *c*-axis films for this thesis could be well described by Equ. (4.21). Fig. 4.29 shows typical data, in this case for $\vartheta = 90°$ and at 50 K. At this rather high temperature the difference between the J_c minimum (at $\varphi = 90°$) and maximum (at $\varphi = 0°$) is large, indicating that the intrinsic pinning force is comparable to the pinning forces of the defects. At low temperatures intrinsic pinning is strong and J_c nearly φ independent. It is however still possible to describe the small variation with Equ. 4.21 (see Fig. 4.30). A measurement on a de-oxygenated sample (see section 4.7)

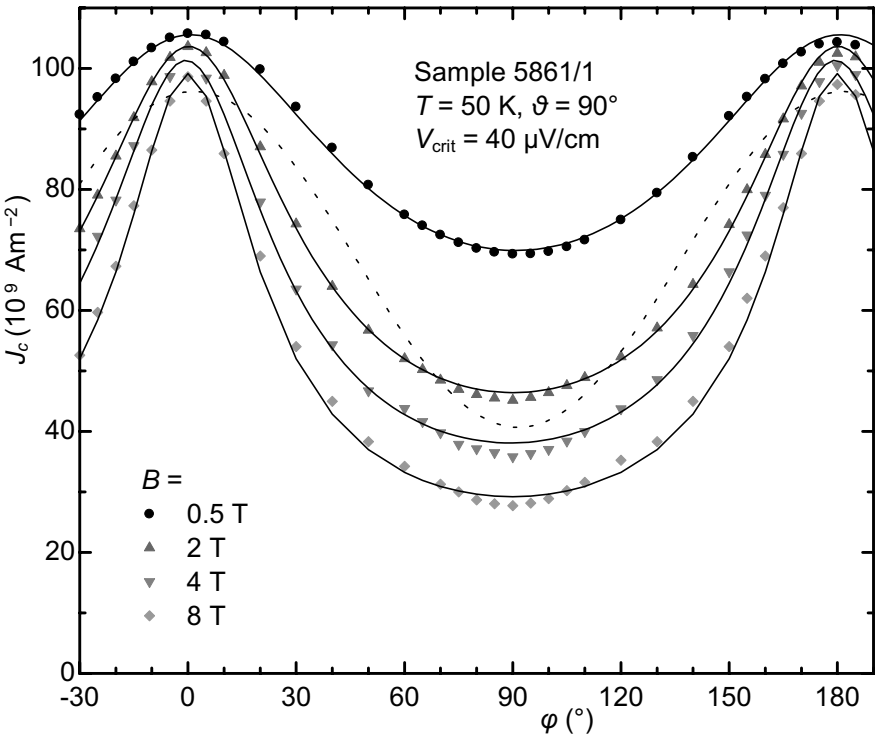

Figure 4.29
$J_c(\varphi)$ at 50 K and several fields. The solid lines are drawn according to Equ. (4.21), the dashed line is a fit of the 2 T data to Equ. (4.23).

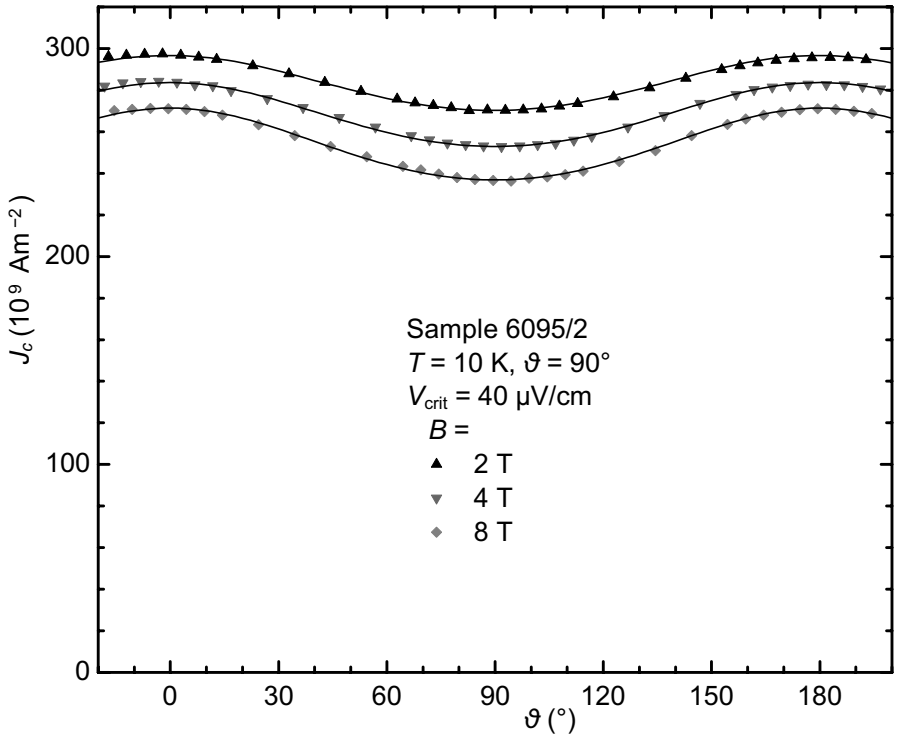

Figure 4.30
$J_c(\varphi)$ at 10 K and several fields. Intrinsic pinning is strong and the variation with φ small. The lines are drawn according to Equ. (4.21).

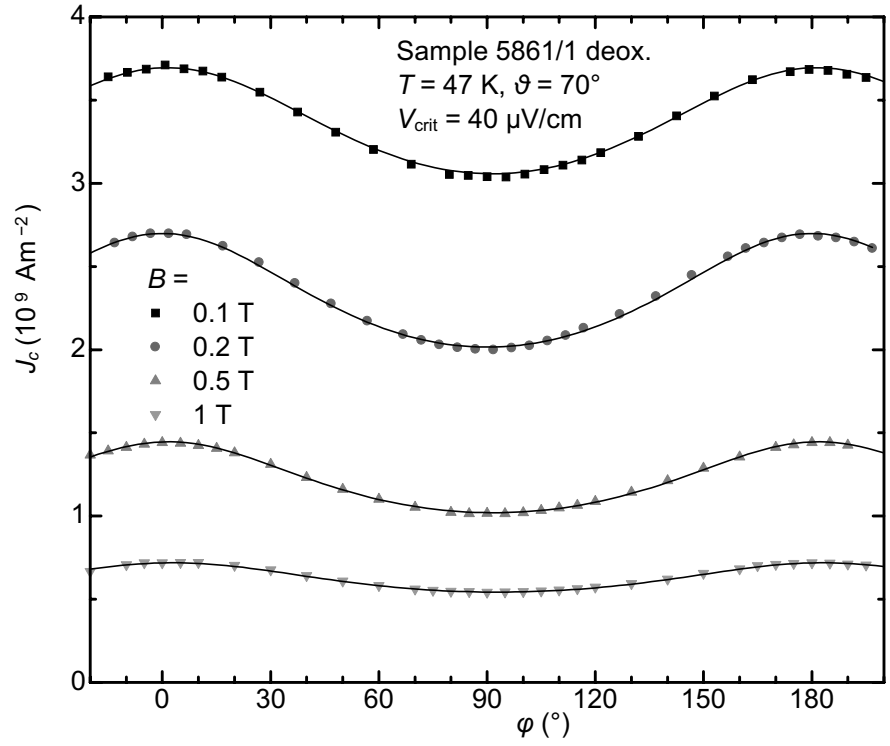

Figure 4.31
$J_c(\varphi)$ of the deoxygenated sample 5861/1 at 47 K and with $\vartheta = 70°$. The lines are drawn according to Equ. (4.21).

with $\vartheta = 70°$ is shown in Fig. 4.31, where Equ. 4.21 again describes the data very well.

From Equ. (4.18) it can be seen that

$$\frac{J_c(0°)}{J_c(90°)} = \sqrt{1+\left(\frac{h_c\, L_{ab}}{h_{ab}\, c}\right)^2} \,. \tag{4.22}$$

At low temperatures intrinsic pinning is most pronounced and h_c therefore much smaller than h_{ab} (h_c is the length over which the pinning potential changes from its minimum to the maximum gradient in c-direction. It is inversely proportional to that gradient.) With c and L_{ab} being of the same order of magnitude, this results in a ratio $J_c(0°)/J_c(90°)$ only slightly larger than 1, in agreement with the experiment (see Fig. 4.30). At higher temperatures intrinsic pinning becomes softer, h_c increases relative to h_{ab} and with it the ratio in Equ. (4.22) (see Fig. 4.29).

Inversely, with Equ. (4.22) the relative strength of intrinsic pinning and the pinning of pancakes by defects can be deduced from experimental data.

4.5.2 Defect pinning of flux line strings

In addition to the intrinsic pinning force parallel to the c-axis there can be a pinning force parallel to the ab-plane on the flux line strings, which originates from defects, just like for the pancakes (see section 4.4.2.2).

Since in c-axis films no current can flow in c-direction, this pinning force can not be probed directly. However, an indirect pinning effect on the flux line structure is possible. When pancakes are depinned and a flux line starts moving parallel to the ab-plane, the flux strings have to move as well. This can only happen when they too are moved out of their defect pinning sites. To asses the influence on J_c, the additional force from these pinning sites countering the Lorentz force has to be estimated. In the following a number of simplifications are assumed to derive the φ-dependence of the effect.

In Fig. 4.32 a section of a flux line is shown, which starts at a string pinning site (small grey area), passes through a pancake pin (larger grey area) and ends at a second string pinning site. With no applied current, the projection of the flux line onto the ab-plane is on average straight (see dashed line in Fig. 4.32b). With increasing current a Lorentz

force pulls the pancake out of its pinning potential and the projection becomes kinked. Via the line tension a net force in (−y)-direction is exerted from the string pins opposing the Lorentz force on the pancake string. Thus a higher current density is required to depin the pancake than if the Lorentz force is only acting against the pinning force of the pancake.

From the variables u (average spacing between pancake and string pins), y', y'' and the line tension it is possible to calculate the net force from the string pins. With the assumption that $y' - y'' \ll u$, the force balance in y-direction can be written

$$F_{\mathrm{Lc}}^{\mathrm{p}} = F_{\mathrm{pc}}^{\mathrm{p}} + 2k(y' - y'')u^{-1}\cos^2\varphi \propto J_{\mathrm{c}}, \tag{4.23}$$

with k the line tension, $F_{\mathrm{Lc}}^{\mathrm{p}}$ the critical Lorentz force on the pancake and $F_{\mathrm{pc}}^{\mathrm{p}}$ the maximum pancake pinning force. The line tension of the flux line strings can be comparatively small, because the order parameter between the CuO_2 layers is suppressed. The displacement y' is of the order of ξ_{ab} and y'' a fraction of y', since there is no direct Lorentz force on the string.

The discussion in the preceding paragraphs did not take the effect of the Lorentz force in c-direction into account, which was discussed in section 4.4.3 and led to a different φ-dependence of J_{c}. Since the experiments strongly favour an interpretation according to Equ. (4.21) rather than Equ. (4.23) (compare the solid and dashed lines in Fig. 4.29), it must be concluded that the pinning of flux strings by defects has a small effect on J_{c}. This assessment is supported by the experiments of Berghuis *et al.* (1997), who observed a minimum in J_{c} when flux strings were pushed in the ab-plane by a current parallel to the c-axis. Another hint in this direction is that J_{c} for a tilted flux line ($\vartheta > 0°$) is never larger than the 2D model predicts. In principle the

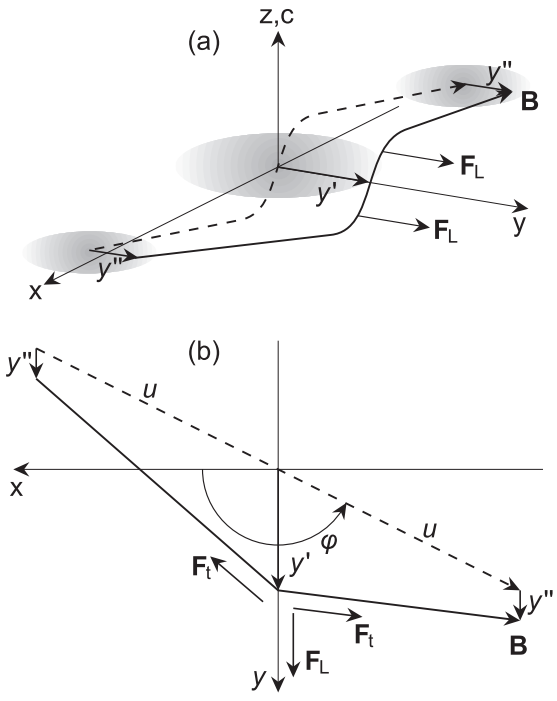

Figure 4.32
Effect of defect pinning of flux strings on pancakes. ($\mathbf{F}_{\mathrm{t}}$ is the force originating from the line tension.)

string pins could provide additional pinning for the pancakes and increase J_c relative to the 2D model, but no clear sign of this effect has been observed.

The only detectable traces of defect pinning of flux line strings are possibly the slight deviations from the fits to Equ. (4.21) in Fig. 4.29. It is conceivable that an even better fit to the data is obtained when defect pinning of the strings is considered in addition to the influence of F_L^z. However, the deviations are small and the Lorentz force effect is clearly dominant.

4.6 ϑ-dependence of J_c

In section 4.3.2 it was found that the 2D model describes the low temperature J_c behaviour in YBCO films best. The key parameter in the 2D model is the field component B_z parallel to the *c*-axis, which determines the pancake density (see Fig. 4.3). Thus the pancake density has the strongest influence on J_c in *c*-axis YBCO films, at least at low temperatures. From studies of the φ-dependence of J_c (see sections 4.4.3 and 4.5) a second parameter influencing J_c emerged, which is the Lorentz force component in *c*-direction, F_L^z. It causes the minimum in J_c for $\varphi = 90°$ where F_L^z has a maximum. The depth of the minimum depends on the ratio of the intrinsic pinning strength to the pancake pinning strength. A closer look at the $J_c(\vartheta)$ data shows that there remain two open questions in order to obtain a reasonably complete understanding of the angular dependence of J_c:

1. What is the origin of the small deviations of $J_c(\vartheta, \varphi = 0°)$ from the 2D model and
2. How does the ratio of pancake and intrinsic pinning depend on ϑ?

For the first question F_L^z has no relevance, since it is zero for $\varphi = 0°$. To get a better picture of the deviations, the strong influence of B_z is eliminated by the introduction of the ratio (compare Equ. (4.2))

$$r(B,\vartheta) = \frac{J_c(B,\vartheta,\varphi = 0°)}{J_c(B\cos\vartheta, \vartheta = 0°, \varphi = 0°)}. \tag{4.24}$$

The denominator is the J_c measured with the field $B\cos\vartheta$ applied parallel to the *c*-axis, which is the reference configuration of the 2D model (see also section 4.3.2). In that configuration all pancakes of a flux line are well aligned. For ideal 2D scaling *r* is

identical 1, which is practically fulfilled at low temperatures (see Fig. 4.33). At higher temperatures, however, deviations occur.

To study the second question another ratio s is introduced:

$$s(B,\vartheta) = \frac{J_c(B,\vartheta,\varphi = 90°)}{J_c(B,\vartheta,\varphi = 0°)} \tag{4.25}$$

Within the model for pinning of a single pancake vortex in the presence of a Lorentz force F_L^z, s is directly related to the relative strength of pancake pinning and intrinsic pinning. The ratio s is the inverse of the ratio introduced in Equ. (4.22) (s, rather than $1/s$, is used here to allow a direct comparison to r). When the intrinsic pinning force is much stronger than the pancake pinning force, s is only slightly smaller than 1 and J_c independent of φ. The weaker intrinsic pinning becomes with higher temperatures, the more s falls below 1.

Both ratios (r and s) are 1 at $\vartheta = 0°$, because the nominators and denominators are identical when B is parallel to the c-axis. In the following the ϑ-dependence of r and s is studied, first at low temperatures (section 4.6.1) and subsequently at higher temperatures (section 4.6.2).

4.6.1 $J_c(\vartheta)$ at low temperatures

At low temperatures ($\lesssim 10$ K) the 2D model describes the behaviour of $J_c(\vartheta)$ very well for $\varphi = 0°$, with deviations smaller than a few percent ($\lesssim 5$ %) at all angles ϑ. However, for $\varphi = 90°$ deviations from the model are observable even at these low temperatures in fully oxygenated films

The logarithmic plot in Fig. 4.33 shows typical J_c data recorded at 10 K. For each field (see symbols) two curves are drawn for $\varphi = 0°$ (larger J_c) and $\varphi = 90°$ (smaller J_c) respectively. The black lines without symbols, which were calculated from $B \parallel c$ measurements, show the prediction of the 2D model. Deviations from the 2D model are very small for $\varphi = 0°$ and reach a maximum of 20 % for $\varphi = 90°$ and $B = 8$ T at $\vartheta = 75°$.

The accurate description of the $\varphi = 0°$ data by the 2D model shows that the decoupling of pancakes belonging to the same flux line, which occurs with increasing ϑ (see Fig. 4.21), has no influence on J_c. In this temperature regime each pancake is pinned in-

dividually and not by its neighbours, showing that the coupling between layers is weak in comparison to the strong pinning.

Because $J_c(B \parallel c)$ is nearly proportional to $B^{-1/2}$, the 2D model approximately predicts that $J_c \propto \cos^{-1/2}\vartheta$. In contrast a simple Lorentz force argument results in $J_c \propto \cos^{-1}\vartheta$ in an isotropic superconductor for $\varphi = 0°$, if a ϑ independent pinning force is assumed. The two angular functions can be clearly distinguished and consequently a simple 3D explanation for the $J_c(\vartheta, \varphi = 0°)$ behaviour excluded.

The deviations for $\varphi = 90°$ on the other hand show that the Lorentz force in *c*-direction (F_L^z) reduces J_c by the mechanism described in section 4.4.3 at low temperatures. This could indicate that the order parameter between the CuO_2 layers is not completely dropping to zero, but that it is only reduced. A certain 3D character, with Josephson coupling between the layers, thus remains in fully oxygenated YBCO even at very low temperatures.

A more detailed analysis of *r* and *s* was conducted on data of sample 5861/1 at 20 K (J_c of this measurement is shown in Fig. 4.16). At this temperature deviations from the 2D model start to appear for $\varphi = 0°$, but they are still small with a maximum of about 15 %

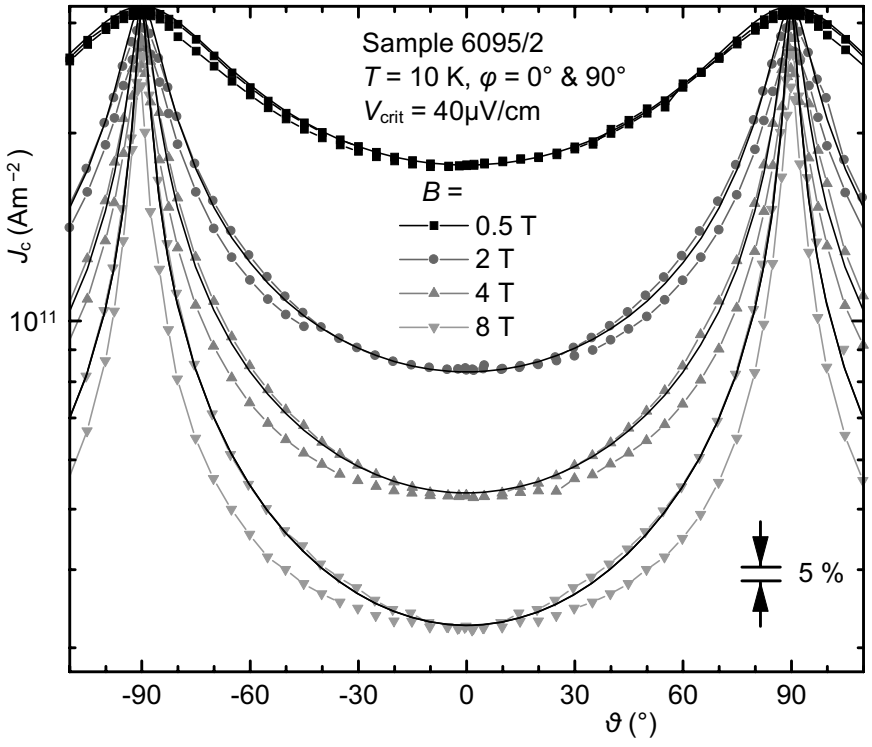

Figure 4.33
$J_c(\vartheta)$ of sample 6095/2 at 10 K for $\varphi = 0°$ and 90°.

at 8 T (Fig. 4.34). With ϑ increasing from 0°, $r(\vartheta)$ gradually drops below 1, reaches a minimum at $\vartheta_{min} \approx 75°$ and increases to 1 again at $\vartheta = 90°$. A possible explanation for this behaviour is that a certain mutual pinning by adjacent pancakes starts to appear with increasing temperature enhancing the J_c of aligned pancakes ($\vartheta = 0°$). When the pancakes become decoupled with increasing ϑ (see Fig. 4.21), they are therefore less well pinned and r drops below 1. Once the pancakes are sufficiently decoupled (i.e. the average string length exceeds $w_{min} = c \tan\vartheta_{min}$), they can better adapt to pancake pinning sites and r rises to 1 for $\vartheta = 90°$. This means that the zero field J_c is reached in the force free configuration ($J \parallel B$; $\vartheta = 90°$, $\varphi = 0°$), even at an applied field of 8 T. The peak in r at $\vartheta = 90°$ corresponds to a very sharp peak in $J_c(\vartheta)$ (see Fig. 4.16).

At 20 K r drops only to a minimum of 0.85 at an applied field of 8 T, but it is already discernible that ϑ_{min} is roughly independent of B. Thus the shape of r seems to be determined by w, which is a property of a single flux line, whereas B influences the magnitude of deviations from the 2D model. This feature is more pronounced at higher temperatures.

Interestingly the shape of $s(\vartheta)$ (see Fig. 4.35) is similar to the shape of $r(\vartheta)$, which

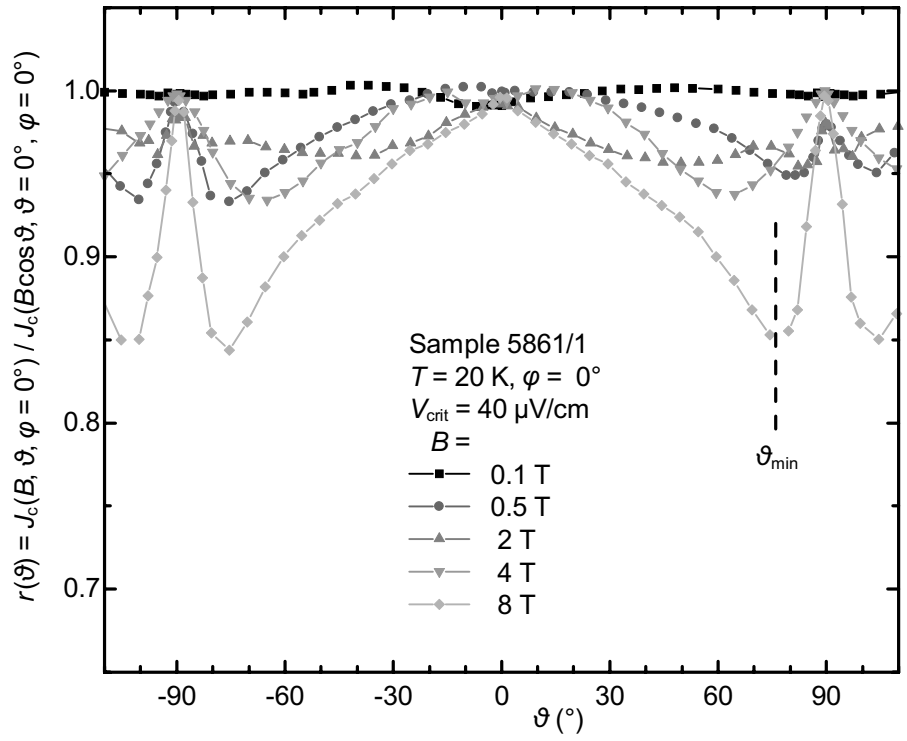

Figure 4.34
Deviations r from the 2D model at 20 K for $\varphi = 0°$.

suggests that it is also caused by the coupling or the spacing of neighbouring pancakes. However, two significant differences are recognisable: s drops to smaller values than r and s does not reach 1 at $\vartheta = 90°$. The mechanism causing the shape of s is perhaps easier to understand than the one for r, since an additional Lorentz force component pulls on the flux lines: Like s, r is by definition 1 for $\vartheta = 0°$. When flux line strings parallel to the ab-plane appear with increasing ϑ, the Lorentz force F_L^z acts on them and s starts to drop. Again a minimum can be seen at a field independent ϑ_{min} and a peak at $\vartheta = 90°$. When the string lengths exceed w_{min} the pancakes can better adapt to the strongest pinning sites and s increases. However, s does not reach 1 because the Lorentz force F_L^z reduces J_c even at $\vartheta = 90°$.

This is to some extent surprising because perfect alignment of B with the ab-plane should lead to the complete disappearance of pancakes and the strong pinning of the strings parallel to the ab-plane to φ independence. There are two possible explanations for this effect. The first is based on the presence of residual pancakes, which could be generated by thermal activation (Iye *et al.*, 1990), the Lorentz force F_L^z and the mechanism described in section 4.4.3. The second explanation is that at J_c the Lorentz force F_L^z simply exceeds the intrinsic pinning force. At low temperatures intrinsic

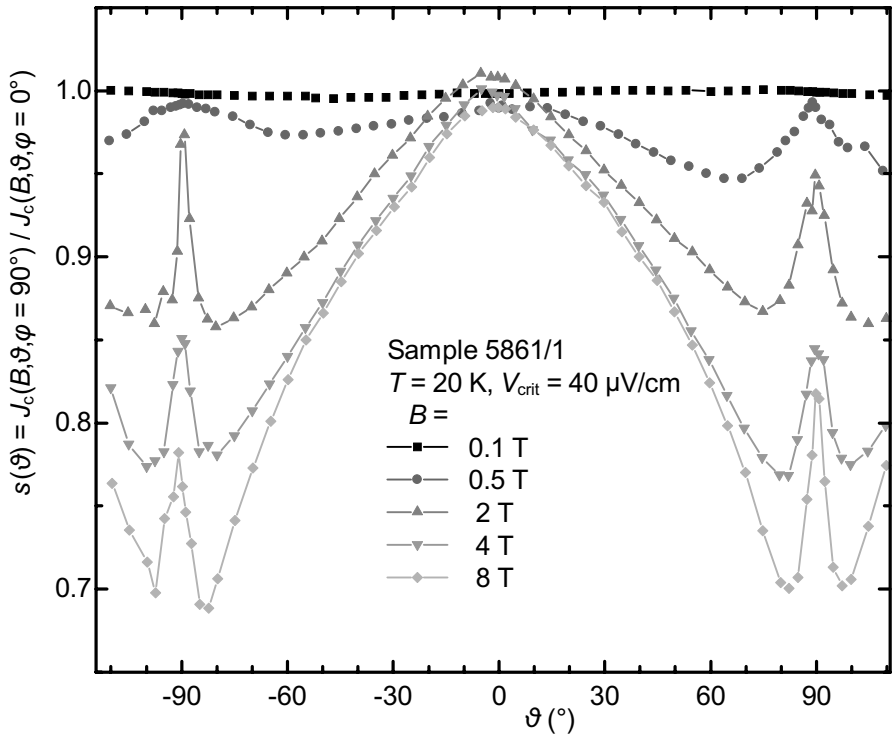

Figure 4.35
Ratio s for sample 5861/1 at 20 K.

pinning is very strong and therefore the first explanation more likely. However, with increasing temperatures the modulation of the order parameter is reduced and thereby intrinsic pinning, such that direct depinning of the flux line strings becomes possible. The behaviour of J_c, r and s at higher temperatures is analysed in the next section.

4.6.2 $J_c(\vartheta)$ at higher temperatures

When the temperature rises above ~20 K, deviations from the 2D model increase more and more. Equally the difference in J_c between the $\varphi = 0°$ and $\varphi = 90°$ configurations grows. Fig. 4.36 shows a comparison of J_c measurements at temperatures between 20 and 77 K at 2 T.

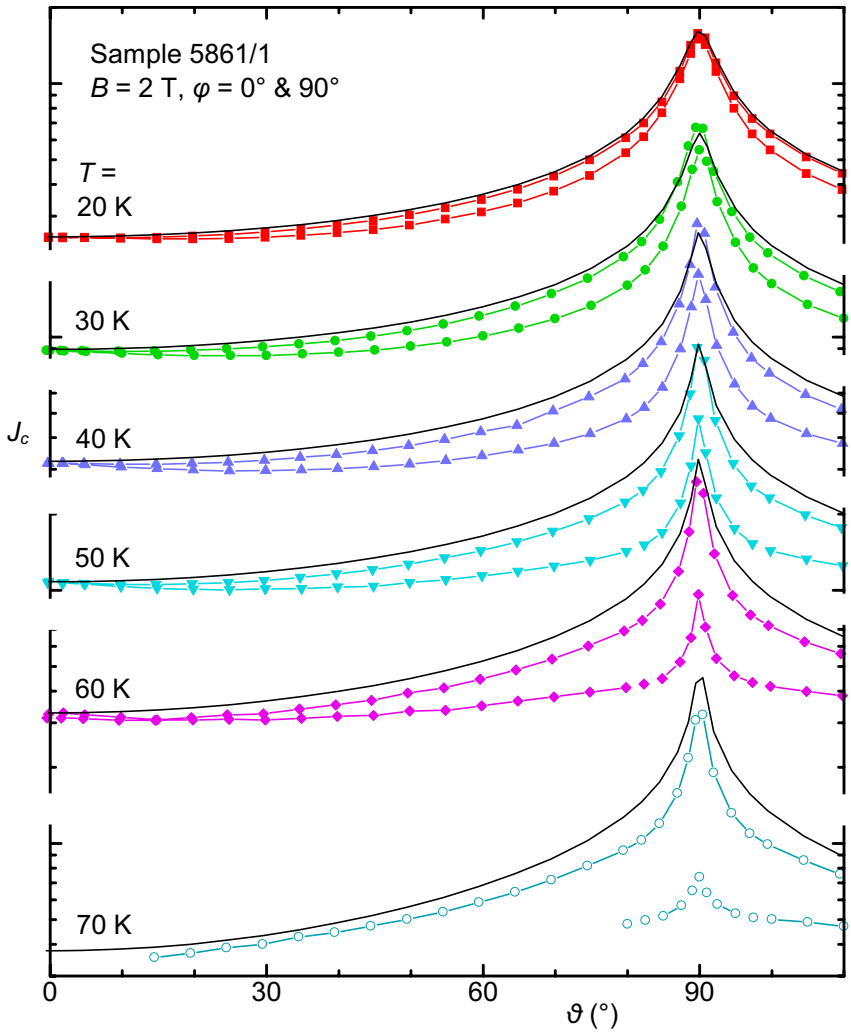

Figure 4.36
Comparison of $J_c(\vartheta)$ at different temperatures. (The curves are shifted vertically to prevent overlapping; absolute data from different temperatures can therefore not be compared.)

For $\varphi = 90°$ the anisotropy becomes smaller at higher temperatures and deviations from the 2D model are much more pronounced.

At 20 K, 2 T and $\varphi = 90°$ J_c is 10 to 15 times larger for $\vartheta = 90°$ than for $\vartheta = 0°$, but at 77 K this factor is reduced to about two, although the field dependence of J_c for $B \parallel c$ remains similar (see Fig. 4.9). The likely reason for this change is the reduction of the intrinsic pinning force. A supporting observation is that J_c is nearly independent of ϑ at 77 K with only a small peak at $\vartheta = 90°$ remaining as a sign of coherent pinning. The

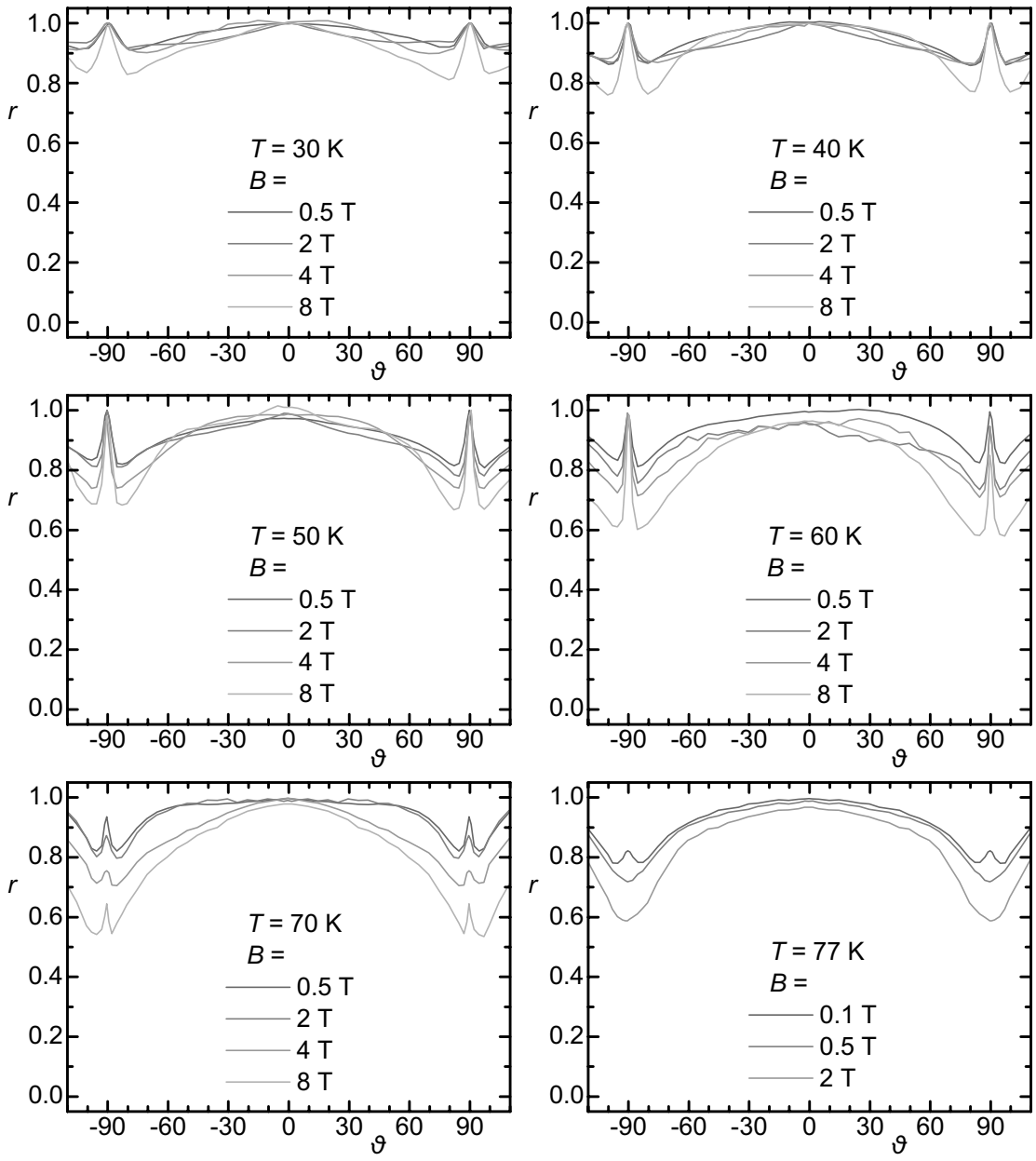

Figure 4.37
The ratio *s* showing the difference between $\varphi = 0°$ and $\varphi = 90°$ measurements, which are related to the Lorentz force component in *c*-direction. $V_{crit} = 40$ μV/cm.

small variation of J_c with ϑ is perhaps surprising, since, with increasing ξ, one might expect a behaviour described by the anisotropic GL theory. J_c should then show a characteristic ϑ dependence (see Fig. 4.19 lowest dashed line), which is not much different from the 2D model for $\vartheta \lesssim 50°$, but has a reduced peak at $\vartheta = 90°$. This is clearly not observed.

To see how the deviations from the 2D model develop with increasing temperature, particularly the minima close to $\vartheta = 90°$, r is plotted for several temperatures and fields

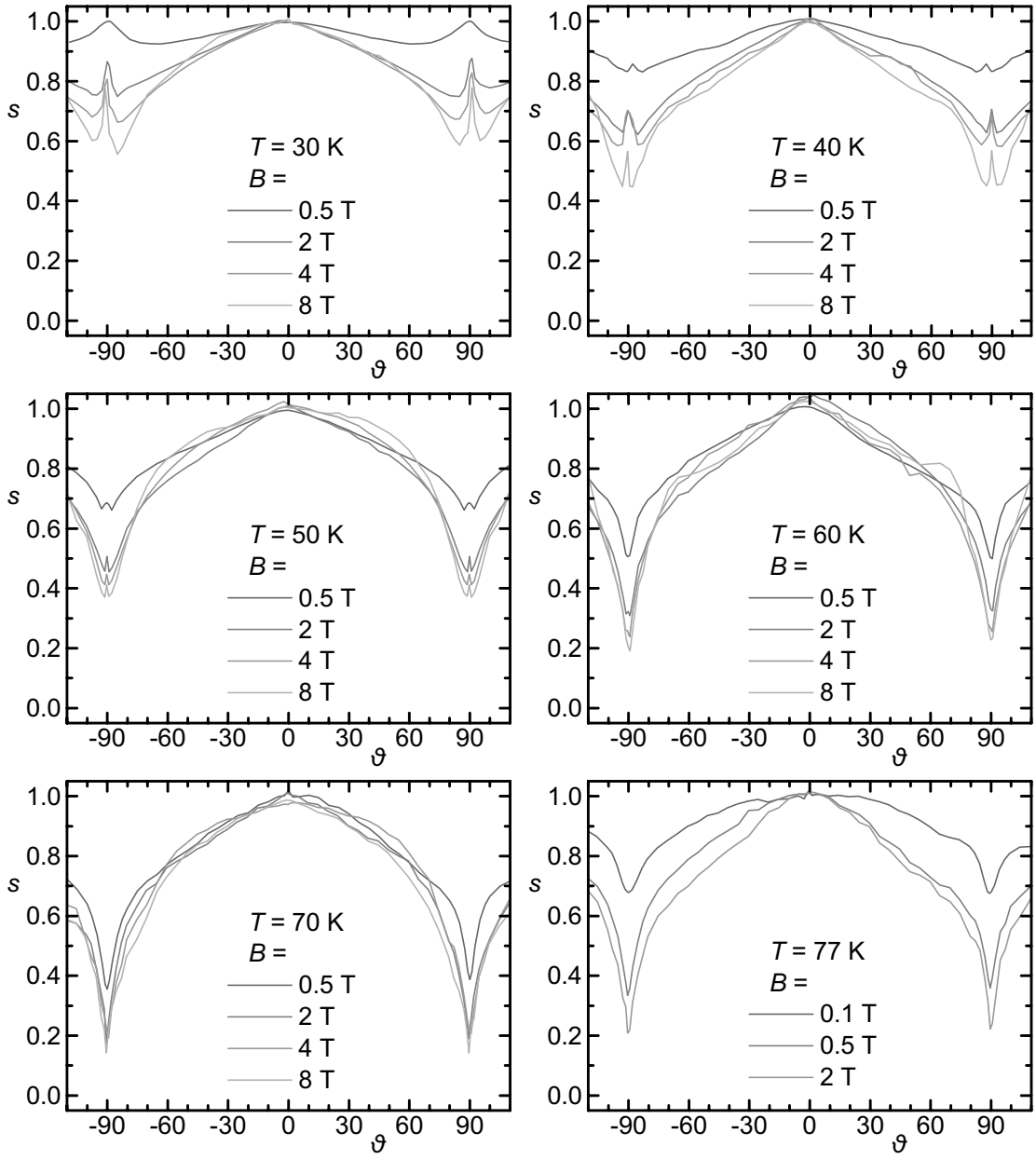

Figure 4.38
Deviations from the 2D model at different temperatures. All plots show measurements on sample 5861/1 with $\varphi = 90°$ and $V_{crit} = 40$ µV/cm.

in Figs. 4.34 and 4.37. A clear trend is observable: the location of the minima remains independent of B (within each plot they are at the same angle ϑ), but with increasing temperature they move closer to $\vartheta = 90°$ until they disappear with the diminishing peaks. In the microscopic picture this means that flux lines have to be tilted ever more with rising T until the pancakes become decoupled and they can individually adapt to pinning sites, i.e. w_{min} increases. At about 70 K this effect disappears completely, the pancakes never fully decouple and the picture of a conventional 3D flux line is more appropriate. The field independence of w_{min} at a given temperature is a strong indication that the shape of r only depends on the structure of a single vortex and not on the vortex-vortex interaction. This is the case at all temperatures.

The plots in Figs. 4.35 and 4.38 show that $s(\vartheta)$ behaves similarly to $r(\vartheta)$. Again, the minimum in s is independent of B, but with rising temperature it moves closer to $\vartheta = 90°$ and it disappears already at $T \approx 60$ K. At this and higher temperatures the pinning forces in c-direction and within the ab-plane are comparable and the model described in section 4.4.3 becomes less useful. Instead a transition to a more conventional 3D-like interpretation is suggested by the small variation of $J_c(\vartheta)$ in the $\varphi = 90°$

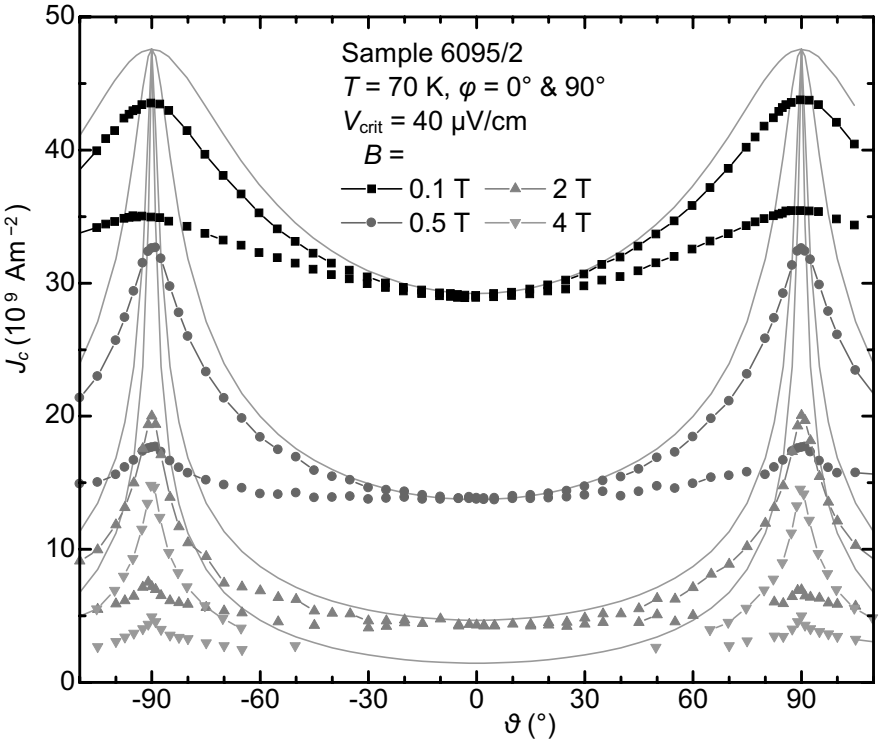

Figure 4.39
$J_c(\vartheta)$ of sample 6095/2 at 70 K and various fields. The smaller J_c values for each field are for $\varphi = 90°$.

case (see Fig. 4.39), consistent with an increasing $\xi(T)$. In this scenario pancakes are strongly coupled and form a nearly conventional flux line. The reduced modulation of the order parameter leads to a disappearing intrinsic pinning effect. A possible origin of the discrepancy between the observed behaviour and the predictions of the anisotropic GL theory, which should appear with ξ_c exceeding c, could be the effects of thermal activation. A more detailed investigation of these, however, remains the subject of a future project.

In this section the detailed behaviour of $J_c(\vartheta)$ at $\varphi = 0°$ and 90° was analysed with the result that deviations from the 2D model for $\varphi = 0°$ ($r(\vartheta)$) as well as the ratio of pancake to intrinsic pinning ($s(\vartheta)$) depend on the coupling or the spacing of pancakes of one flux line and the magnitude of the applied magnetic field. The former, for which the distance between adjacent pancakes w can be used as a measure, mainly determines the shape of r and s, whereas B influences the magnitude of the deviations of r and s from 1. In addition to the pancake density and the Lorentz force component in c-direction, w and B are thus the third and fourth parameters influencing the angular dependence of J_c in c-axis YBCO films.

4.7 J_c in deoxygenated samples

Experiments presented in the previous section showed that although intrinsic pinning is very strong in fully oxygenated YBCO films at low temperatures (~10 K), J_c still varies when an applied field is rotated in the *ab*-plane (i.e. J_c varies with φ when $\vartheta = 90°$). Thus the behaviour deviates from the predictions of the 2D model and a residual 3D character remains visible in YBCO, contrasting the near perfect 2D behaviour of the much more anisotropic BiSCCO (Iye *et al*., 1989). For YBCO it has been suggested (Cava *et al*., 1990) that a removal of oxygen from the chain sites (O1A sites in Fig. 2.1) further decouples the CuO_2 plains and leads to more 2D like electric properties. To see if the character of $J_c(\vartheta,\varphi)$ becomes more two dimensional, a number of samples were deoxygenated and J_c measured and analysed in the same way as described in the previous sections.

4.7.1 Deoxygenated YBCO films

Several YBCO films were deoxygenated in an ultra high vacuum system, which was mainly used to deposit films (see section 3.1.3). The amount of deoxygenation was determined with a T_c measurement after the treatment and the now well established relation between T_c and δ (see Fig. 2.3 and Poulsen *et al*., 1991a; Poulsen *et al*., 1991b). In Fig. 4.40 the resistive transitions of sample 5861/1 are compared in fully oxygenated condition and after deoxygenation. In the latter state T_c is 61.5 K, which is just above the 60 K plateau, resulting in a δ of about 0.3.

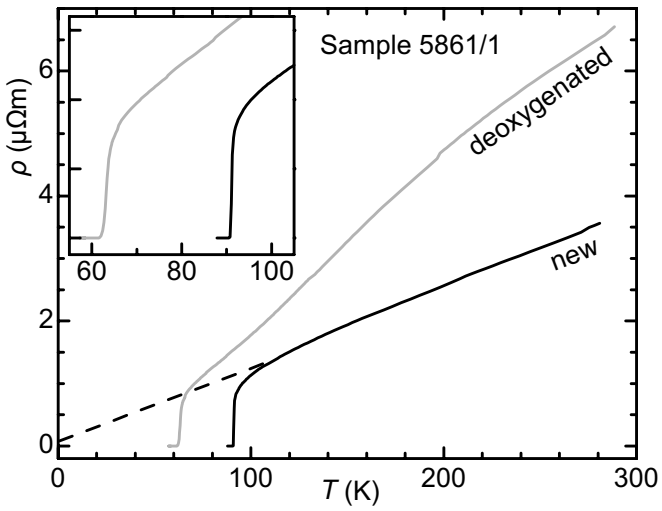

Figure 4.40
Resistive transition of sample 5861/1 before and after deoxygenation. The insert shows a magnification around T_c.

In addition to the change in T_c, deoxygenation has as strong effect on J_c for fields applied parallel to the *c*-axis (see Fig. 4.41). At 10 K and small applied fields J_c drops by a factor of about two from the J_c of the fully oxygenated film, but by much more at fields above 3 T, because of a substantial drop of B_{c2}^{c} as can be seen by the downward curvature of the 10 K line in Fig. 4.41. In fully oxygenated films a similar downward bending can only be observed for temperatures above 50 K in the experimentally accessible field range between 0 and 8 T (compare Fig. 4.10). With increasing T, $J_c(B = 0)$ and B_{c2}^{c} drop, leading to a shift of the $J_c(B)$ lines to the lower left corner in Fig. 4.41. At low temperatures $J_c(B)$ still follows an inverse power law in a field region between ~0.1 and 3 T, but the exponent is not exactly 1/2 any more but with 0.67 slightly larger. Christen and Feenstra (1991) argue that the defect density in fully oxygenated films already results in near optimal pinning, which can not be improved by the introduction of oxygen defects, and so deoxygenation only leads to a reduction of the carrier density in the CuO_2 planes and hence a decrease of J_c.

4.7.2 ϑ-dependence of J_c in deoxygenated films

This section presents the differences between the ϑ-dependence of J_c in deoxygenated YBCO films and the one in fully oxygenated samples, which occur mainly at low temperatures. There is no difference in the φ-dependence of J_c, which can again be described by Equ. (4.21). Because $J_c(\vartheta)$ is even more two dimensional in deoxygenated than in fully oxygenated films, the same analytical methods as in section 4.6 are used in the following, namely the ratios $r(\vartheta)$ and $s(\vartheta)$ defined in Equs. (4.24) and (4.25) respectively.

J_c at 10 K varies by more than two orders of magnitude when a magnetic field of 8 T is rotated from parallel to the *c*-axis to parallel to the *ab*-plane (see Fig. 4.42). Over this whole range deviations from the 2D model are negligible for $\varphi = 0°$ and reach a maximum of only ~20% for $\varphi = 90°$ at 8 T and $\vartheta = 82°$. However, the main difference to the fully oxygenated films is the fact that J_c reaches the zero field value for all angles φ when the field is exactly parallel to the *ab*-plane. Since the peak at $\vartheta = 90°$ is extremely sharp at high fields, it was necessary to change ϑ in very small steps at a series of φ values in order to resolve the real J_c maxima. Only after numerically removing a small

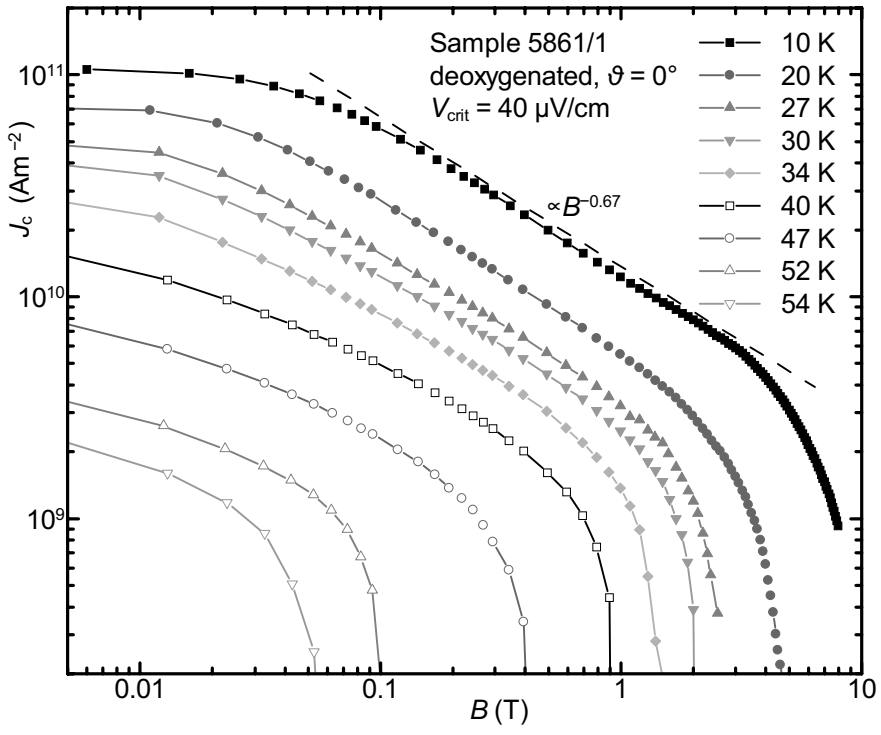

Figure 4.41
J_c of deoxygenated sample 5861/1 as a function of a field applied parallel to the *c*-axis.

misalignment error of the instrument (see section 3.3.2) the correct J_c variation could be plotted in Fig. 4.43. It can be seen that J_c drops to half the maximum when the field is rotated away from the *ab*-plane by only one degree. The maximum value on the other hand is independent of φ.

At 20 K the behaviour of J_c, r and s is similar to the one at 10 K: r is identical 1 for all fields and although the minima in $s(\vartheta)$ drop to ~0.6 at $\vartheta_{min} = 86°$ for 8 T, J_c reaches the zero field value for $\vartheta = 90°$ in a very sharp peak (i.e. s is 1 at $\vartheta = 90°$; see Fig. 4.44 left).

At 27 K the situation is however different. At $\vartheta = 90°$ s does not reach 1 any more (right Fig. 4.44), but the very narrow peak is cut off at 0.8. Also $r(\vartheta)$ deviates from 1 in the vicinity of $\vartheta = 90°$ in a similar way to fully oxygenated films at all but the lowest temperatures (compare Fig. 4.37). (Because B_{c2}^{c} cuts J_c off at $B \parallel c \approx 2.5$ T at 27 K, $J_c(\vartheta)$, s and r are limited to a window around $\vartheta = 90°$ – see Fig. 4.41.)

A possible explanation of this change of behaviour between 20 and 27 K is that at lower temperatures the coupling between CuO_2 layers is weak and each pancake has to be pinned individually, independent of w, the horizontal displacement between neigh-

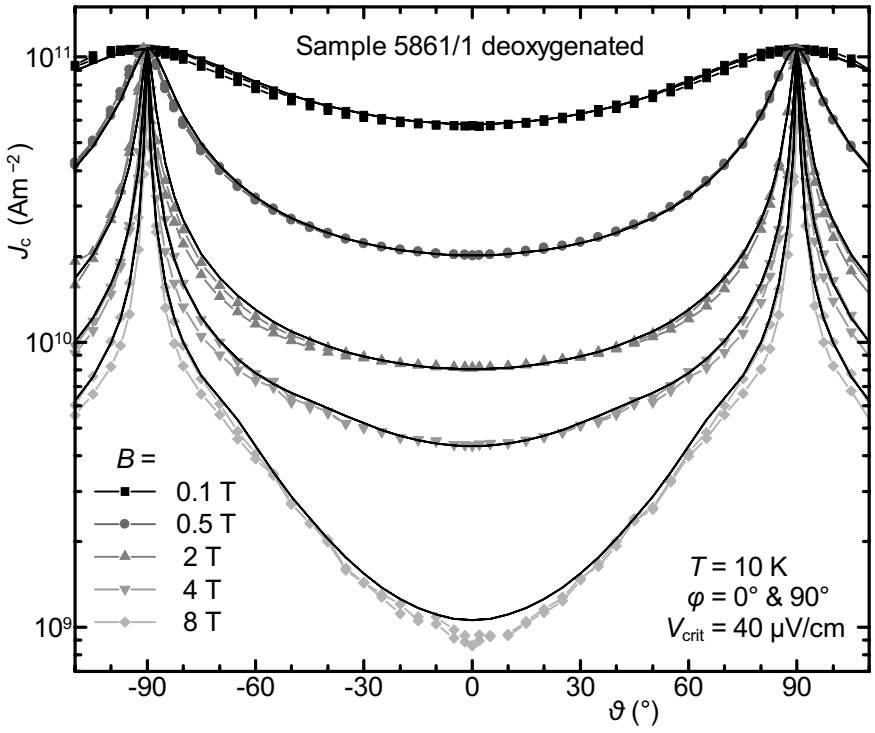

Figure 4.42
$J_c(\vartheta)$ of the deoxygenated sample 5861/1 at 10 K. At each field and angle ϑ the symbols with larger J_c are for $\varphi = 0°$ and the ones with smaller J_c $\varphi = 90°$.

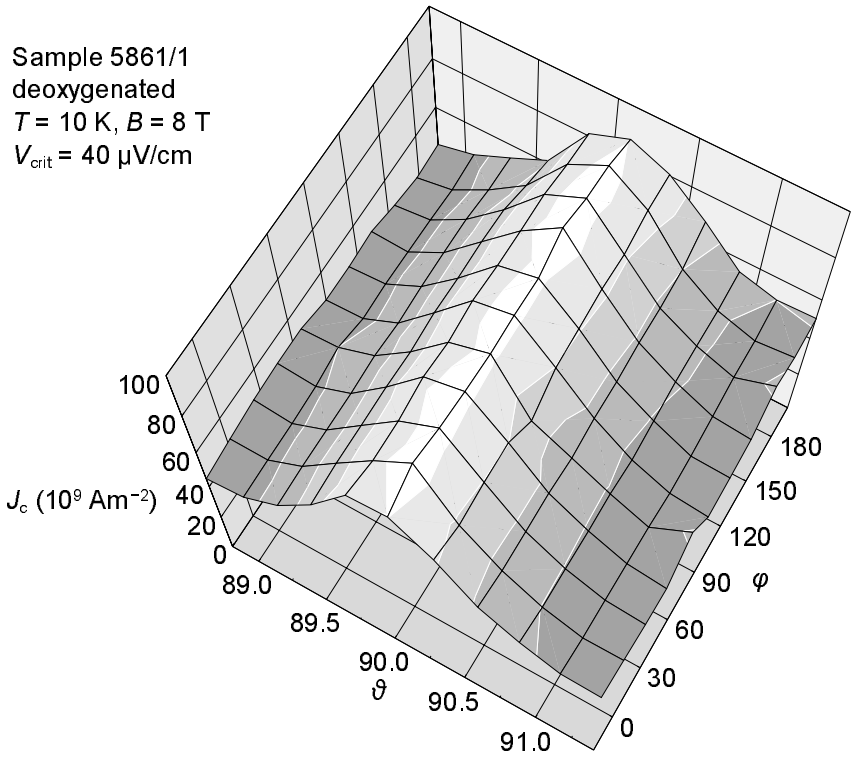

Figure 4.43
J_c of the deoxygenated sample 5861/1 with **B** close to the *ab*-plane. Note the different scales on the ϑ and φ axes.

bouring pancakes. The weak coupling also means that the order parameter is strongly reduced between the layers so that a field applied exactly parallel to the *ab*-plane passes through the sample leaving $|\psi|^2$ in the CuO_2 layers unchanged. In addition the strong modulation of the order parameter leads to a very strong intrinsic pinning force such that the zero applied field J_c can be reached for fields applied parallel to the *ab*-plane and normal to the current direction where the maximum Lorentz force is acting (i.e. ϑ and φ are 90°). At 27 K ξ_c seems to be just large enough to enable coupling between the CuO_2

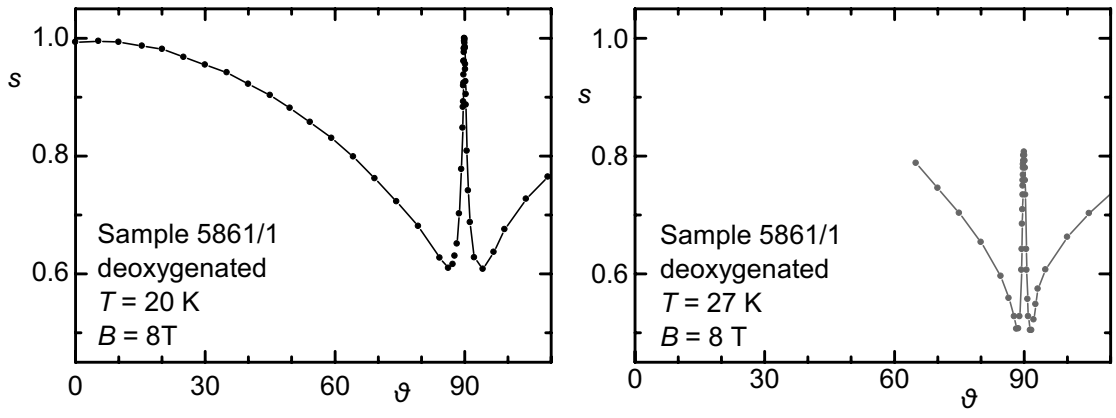

Figure 4.44
$s(\vartheta)$ of sample 5861/1 after deoxygenation at 20 K (left) and 27 K (right).

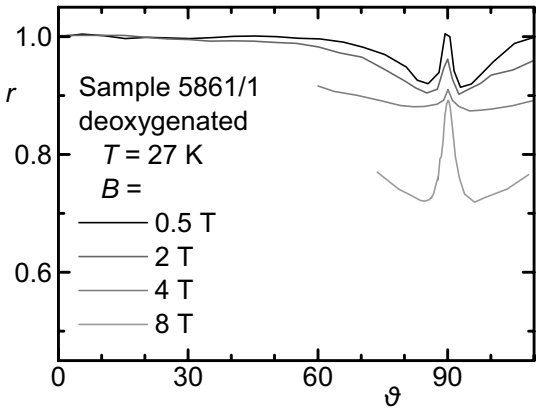

Figure 4.45
$r(\vartheta)$ of the deoxygenated sample 5861/1 at 27 K.

planes. In this case J_c is larger for aligned and coupled pancakes ($0° \leq \vartheta \lesssim 60°$) than for decoupled pancakes which all have to be pinned individually ($\vartheta \approx \vartheta_{min}$; see Fig. 4.45). When the field moves to the force free configuration and the number of pancakes is rapidly reduced, s increases to a maximum at $\vartheta = 90°$.

The angular dependence of J_c at 27 K and higher temperatures is qualitatively similar to the one observed in fully oxygenated films. The main differences in this regime arise from the lower T_c and B_{c2}^{c}.

In summary experiments on deoxygenated films showed that J_c and B_{c2} are substantially reduced in comparison to fully oxygenated films and that characteristic features of 2D behaviour remain observable up to higher temperatures (~20 K).

4.8 Conclusions

Chapter 4 presented a detailed investigation of critical currents in *c*-axis YBCO films. Since the intrinsic layered structure of the material generates a strong anisotropy of the basic superconducting properties, J_c depends crucially – and differently to isotropic superconductors – on the direction of an externally applied field. J_c was measured on a number of films with a purpose built goniometer.

Following a review of models suggested by a number of authors to explain the angular dependence of J_c (section 4.1), experiments showed that the 2D model proposed by Kes *et al*. (1990) is the most adequate to describe the behaviour, particularly at low temperatures (sections 4.2 and 4.3). Because this model takes the layered structure explicitly into account, concepts of flux lines in layered superconductors are presented in section 4.4. A model of a single pancake vortex at a pinning site resulted in an expression of the φ-dependence of J_c, which proved to describe the experiments presented in section 4.5 accurately. A closer look at the deviations from the 2D model followed in section 4.6 and a brief overview of experiments in deoxygenated films

showed that some characteristic 2D properties remain at higher temperatures (up to 20 K) than in fully oxygenated films.

In agreement with the 2D model it was found that the most influential parameter on J_c is the field component parallel to the *c*-axis, which microscopically determines the density of pancake vortices. In deoxygenated films at 10 K J_c is reduced by a factor of 100 when the field is increased to 8 T. A second parameter reducing J_c is a Lorentz force component parallel to the *c*-axis F_L^z, which acts on the flux strings parallel to the *ab*-plane. Particularly at higher temperatures, where the intrinsic pinning potential is reduced ('washed out'), F_L^z can overcome the intrinsic pinning force comparatively easily and J_c nearly behaves as in isotropic materials (i.e. is independent of ϑ for $\varphi = 90°$).

The structure of deviations from the 2D model can be explained by the coupling of pancakes of one flux line, which depends on the spacing between adjacent pancakes *w* and hence ϑ. The amount of the deviations depends on the magnitude of the applied field *B*.

The main physical conclusions from the experiments on *c*-axis YBCO films are that the dependence of J_c on the direction of an applied field can be well explained by the 2D model and the effect of intrinsic pinning. At low temperatures and $\varphi = 0°$ the model is very accurate, but a Lorentz force on the flux line strings parallel to the *ab*-plane can reduce J_c, implying a deviation from the pure 2D model.

With increasing temperature coupling between the CuO_2 layers becomes stronger, the modulation of the order parameter is reduced and with it the strength of the intrinsic pinning effect. This gradual transition occurs at higher temperatures in deoxygenated films than in fully oxygenated ones.

4.9 References

Adrian, H., G. Jakob, C. Tomé-Rosa, M. Schmitt, P. Wagner, T. Hahn, T. Kluge and M. Speckmann, 1993, Int. Jour. of Mod. Phys. **B7**, 113-122.

Anderson, P.W., 1962, Phys. Rev. B **9** (7), 309-311.

Anderson, P.W. and Y.B. Kim, 1964, Reviews of ModernPhysics **January**, 39-43.

Aomine, T., T. Nishizaki, F. Ichikawa, T. Fukami, T. Terashima and Y. Bando, 1993, Physica B **194-196**, 1613-1614.

Berghuis, P., E. Di Bartolomeo, G.A. Wagner and J.E. Evetts, 1997, Phys. Rev. Lett, **79** (12), 2332-2335.

Berghuis, P., R. Herzog, R.E. Somekh, J.E. Evetts, R.A. Doyle, F. Baudenbacher and A.M. Campbell, 1996a, Physica C **256**, 13-32.

Berghuis, P., G.A. Wagner, S.C. Fan and J.E. Evetts, 1996b, The 8th IWCC in Superconductors, Kitakyushu, Japan, World Scientific, Singapore, 1996.

Blatter, G., M.V. Feigel'man, V.B. Geshkenbein, A.I. Larkin and V.M. Vinokur, 1994, Reviews of Modern Physics **66** (4), 1125-1388.

Blatter, G., V.B. Geshkenbein and A.I. Larkin, 1992, Phys. Rev. Lett. **68** (6), 875-878.

Brongersma, S.H., Thesis 1996, *Vortex configurations in superconducting thin films and multilayers*. Vrije Universiteit Amsterdam, Amsterdam

Bugoslavsky, Y.V., A.A. Zhukov, G.K. Perkins, A.D. Caplin, H. Kojima and I. Tanaka, 1997, Phys Rev B **56** (9), 5610-5616.

Cava, R.J., A.W. Hewat, E.A. Hewat, B. Batlogg, M. Marezio, K.M. Rabe, J.J. Krajewski, W.F. Peck and L.W. Rupp, 1990, Physica C **165**, 419-433.

Chaudhari, P., R.H. Koch, R.B. Laibowitz, T.R. McGuire and R.J. Gambino, 1987, Phys Rev Lett **58** (25), 2684-2686.

Christen, D.K. and R. Feenstra, 1991, Physica C **185-189**, 2225-2226.

Christen, D.K., C.E. Klabunde, R. Feenstra, D.H. Lowndes, D. Norton, J.D. Budai, H.R. Kerchner, J.R. Thompson, L.A. Boatner, J. Narayan and R. Singh, 1990, Physica B **165**, 1415-1416.

Christen, D.K., C.E. Klabunde, R. Feenstra, D.H. Lowndes, D.P. Norton, J.D. Budai, H.R. Kerchner, J.R. Thompson, S. Zhu and A.D. Marwick, 1991, Supercond. and its Appl. **219** (75), 336.

Clem, J.R., 1991, Phys. Rev. B **43** (10), 7837-7846.

Clem, J.R., 1992, Superconductor Science & Technology **5**, S33-40.

Clem, J.R., 1993, Anisotropic Superconductors: Fundamentals of Vortices in Layered Superconductors. *Proceedings of the NATO Advanced Study Institute, Vortices in Superconductors* N. Bontemps, Ed. Dordrecht, Kluwer.

Dinger, T.R., T.K. Worthington, W.J. Gallagher and R.L. Sandstrom, 1987, Phys. Rev. Lett. **58** (25), 2687-2690.

Dolan, G.J., F. Holtzberg, C. Feild and T.R. Dinger, 1989, Phys. Rev. Lett. **62**, 827.

Douwes, H., P.H. Kes, C. Gerber and J. Mannhart, 1993, Cryogenics **33** (5), 486-491.

Iye, Y., S. Nakamura and T. Tamegai, 1989, Physica C **159**, 433-438.

Iye, Y., S. Nakamura, T. Tamegai, T. Terashima, K. Yamamoto and Y. Bando, 1990, Physica C **166**, 62-70.

Iye, Y., T. Tamegai, T. Sakakibara, T. Goto, N. Miura, H. Takeya and H. Takei, 1988, Physica C **153-155**, 26-31.

Jakob, G., M. Schmitt, T. Kluge, C. Tomerosa, P. Wagner, T. Hahn and H. Adrian, 1993, Phys. Rev. B **47** (18), 12099-12103.

Kes, P.H., J. Aarts, V.M. Vinokur and C.J. van der Beek, 1990, Phys. Rev. Lett. **64** (9), 1063-1066.

Kim, Y.B., C.F. Hempstead and A.R. Strnad, 1963, Physical Review **131** (6), 2486-2495.

Kramer, E.J., 1973, J. Appl. Phys. **44** (3), 1360-1370.

Kuwasawa, Y., T. Yamaguchi, T. Tosaka, S. Aoki and S. Nakano, 1990, Physica C **169** (1-2), 39-42.

Lawrence, W.E. and S. Doniach, 1970, 12th Int. Conf. on Low Temperature Physics, Kyoto, Keigaku, Tokyo 1970.

Li, Q., C. Kwon, X.X. Xi, S. Bhattacharya, A. Walkenhorst, T. Venkatesan, S.J. Hagen, W. Jiang and R.L. Greene, 1992, Phys. Rev. Lett. **69** (18), 2713-2716.

Lowndes, D.H., D.K. Christen, C.E. Klabunde, Z.L. Wang, D.M. Kroeger, J.D. Budai, Shen Zhu and D.P. Norton, 1995, Phys. Rev. Lett. **74** (12), 2355-2358.

Mannhart, J., D. Anselmetti, J.G. Bednorz, C. Gerber, K.A. Müller and D.G. Schlom, 1992, Supercond. Sci. Technol. **5** (S1), S125-S128.

Niel, L., 1992, Cryogenics **32** (11), 975-978.

Nishizaki, T., T. Aomine, I. Fujii, K. Yamamoto, S. Yoshii, T. Terashima and Y. Bando, 1991a, Physica C **185**, 2259-2260.

Nishizaki, T., T. Aomine, I. Fujii, K. Yamamoto, S. Yoshii, T. Terashima and Y. Bando, 1991b, Physica C **181** (4-6), 223-232.

Nishizaki, T., F. Ichikawa, T. Fukami, T. Aomine, T. Terashima and Y. Bando, 1993, Physica C **204** (3-4), 305-314.

Oussena, M., P.A.J. de Groot, R. Gagnon and L. Taillefer, 1994, Phys. Rev. Lett. **72** (22), 3606-3609.

Palstra, T.T.M., B. Batlogg, R.B. van Dover, L.F. Schneemeyer and J.V. Waszczak, 1988, Appl. Phys. Lett. **54** (8), 763-765.

Pan, V.M., 1993, J. of Alloys and Compounds **195**, 451.

Poulsen, H.F., N.H. Andersen, J.V. Andersen, H. Bohr and O.G. Mouritsen, 1991a, Physical Review Letters **66** (4), 465-468.

Poulsen, H.F., N.H. Andersen, J.V. Andersen, H. Bohr and O.G. Mouritsen, 1991b, Nature **349** (14. Feb. 1991), 594-596.

Ravi Kumar, G., M.R. Koblischka, J.C. Martinez, R. Griessen, B. Dam and J. Rector, 1994, Physica C **235-240**, 3053-3054.

Roas, B., L. Schultz and G. Saemannischenko, 1990, Phys. Rev. Lett. **64** (4), 479-482.

Samadi Hosseinali, G., R.M. Schalk, H.W. Weber, A. Pönninger, S. Proyer and P. Schwab, 1994, Physica B **194** (Pt2), 2357-2358.

Schalk, R.M., G.S. Hosseinali, H.W. Weber, Z.H. Barber, P. Przyslupski, J.E. Evetts, A. Pönninger, P. Schwab, S. Proyer, A. Kochemasov and D. Bäuerle, 1993, Cryogenics **33** (3), 369-374.

Schalk, R.M., G. Samadi Hosseinali, H.W. Weber, J.E. Evetts, A. Pöninger and D. Bäuerle, 1992a, Workshop of EU Science Program (SCI-0389) on Flux Pinning in HTS, Zaragoza.

Schalk, R.M., G. Samadi Hosseinali, H.W. Weber, S. Proyer, P. Schwab, D. Bäuerle and S. Gründorfer, 1994, Phys. Rev. B **49** (5), 3511-3519.

Schalk, R.M., H.W. Weber, Z.H. Barber, P. Przyslupsky and J.E. Evetts, 1992b, Physica C **199** (3-4), 311-320.

Schmitt, M., T. Kluge, C.T. Rosa, G. Jakob, P. Wagner, T. Hahn and H. Adrian, 1993, Int. Jour. of Mod. Phys. B **7** (1-3), 135-138.

Schmitt, P., P. Kummeth, L. Schultz, B. Roas and G. Saemann-Ischenko, 1992, Superconductor Science & Technology **5** (S1), S101-S104.

Tachiki, M., T. Koyama and S. Takahashi, 1991, Physica C **185-189**, 303-308.

Tachiki, M. and S. Takahashi, 1989a, Solid State Communications **72** (11), 1083-1086.

Tachiki, M. and S. Takahashi, 1989b, Solid State Communications **70** (3), 291-295.

Tinkham, M., 1996, *Introduction to Superconductivity*. New York, McGraw-Hill.

Walkenhorst, A., C. Tomerosa, C. Stölzel, G. Jakob, M. Schmitt and H. Adrian, 1991, Physica C **177** (1-3), 165-170.

Welp, U., W.K. Kwok, K.G. Crabtree, K.G. Vandervoort and J.Z. Liu, 1989, Phys. Rev. B **40** (7), 5263.

Wördenweber, R., 1992, Phys. Rev. B **46**, 3076.

Yeshurun, Y., A.P. Malozemoff, T.K. Worthington, R.M. Yandrofski, L. Krusin-Elbaum, F.H. Holtzberg, T.R. Dinger and G.V. Chandrashekhar, 1989, Cryogenics **29**, 258-262.

Chapter 5

Critical Currents in (110) YBCO Films

For the study of the anisotropic properties of YBCO *c*-axis films are well suited because high quality epitaxial samples are available with excellent alignment of the *c*-axis of all grains (except outgrowths) with the film normal (see chapter 4). However, it is not possible to apply a current in *c*-direction in these films, which is a severe restriction for a complete understanding of the critical currents in YBCO. To overcome this limitation films were deposited with the *c*-axis parallel to the film surface and test tracks patterned normal and parallel to the *c*-axis. This chapter describes J_c measurements on such films as a function of a magnetic field applied in various directions. Some of the resulting configurations have not been investigated before.

The first section of this chapter describes the deposition and characterisation of (110) films and the reason for the choice of this particular film type. Subsequently some experiments by other authors on similar films are reviewed. The sections 5.3 and 5.4 present J_c measurements on tracks normal and parallel to the *c*-axis respectively.

5.1 Deposition and characterisation of (110) YBCO films

On (100) $SrTiO_3$ substrates it is possible to deposit YBCO films with the *c*-axis parallel to the film surface by heating the substrate to only about 600 °C during deposition rather than to the ~700 °C optimal for *c*-axis growth (see section 3.1.1). Films made with this method are called *a*-axis films. Unfortunately they are in general heavily twinned, which

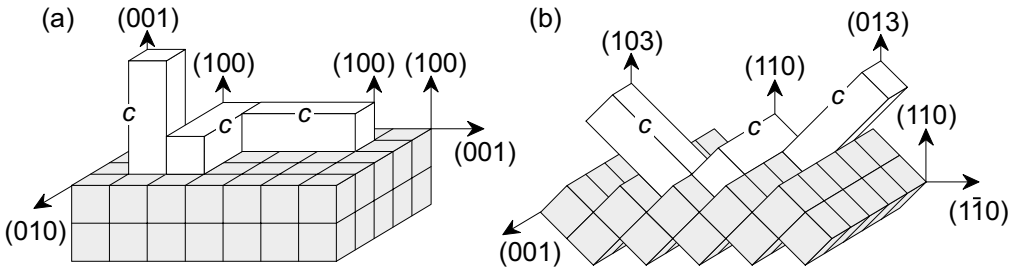

Figure 5.1
YBCO unit cells on (100) and (110) $SrTiO_3$ substrates (grey). Films with *a*-axis orientation grown on (100) substrates (a) are nearly always twinned and the *c*-axes of two grains are generally not aligned (two lying unit cells). Many *a*-axis films also show a fair amount of *c*-axis outgrowth (upright unit cell). On (110) substrates (b) (110)-film-growth is favourable under carefully controlled conditions and the growth of (103) and (013) films is suppressed. Arrows attached to the substrate indicate normals to substrate crystal planes, arrows attached to film cells indicate normals to film crystal planes.

means that the directions of the *c*-axis of different twin domains are not aligned although they are all parallel to the film plane (see Fig. 5.1a). An elegant way to circumvent this difficulty is the use of $SrTiO_3$ substrates polished parallel to the [110] plane. On such substrates it is possible to deposit films where the *c*-axis of all grains is aligned with the (001) direction of the $SrTiO_3$ (see Fig. 5.1b).

The samples described in this chapter have been produced in our research group using a slight variation of the on-axis high pressure DC sputtering technique, called template process (Inam *et al*., 1990). A 50 nm layer of YBCO (the template layer) is grown hetero-epitaxially on (110) $SrTiO_3$ at a substrate temperature of 600 °C. Subsequently the temperature is increased to about 710 °C and the main part of the film (150 nm) grown homo-epitaxially on the template layer at conditions optimised for single crystal films. The initial lower deposition temperature reduces the mobility of the ions condensing on the substrate thereby suppressing the growth of (103) grains. Fig. 5.2 shows x-ray ω-scans of four films where the template layer was deposited at the temperature indicated. Only in the films where the template layers were deposited at 665 and 705 °C the (0 0 13) peak of the (103) phase becomes detectable, giving a clear indication that no such phase is present in the other two films. For the experiments described below, films of the latter type were chosen.

The microstructure of (110) films produced by the described process is different from the microstructure of sputtered *c*-axis films. This can be clearly seen using an Atomic Force Microscope (Fig. 5.3). YBCO crystallites grow much faster along the *ab*-plane than in *c*-direction. Nucleating grains hence expand quicker normal to the film surface and in the (110) direction within the film plane than along the *c*-axis, forming the structure of upright standing

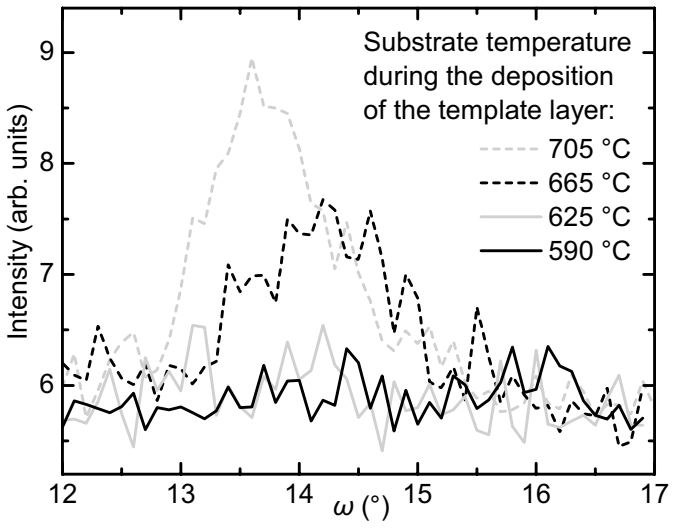

Figure 5.2
X-ray ω-scans of films with template layers deposited at different substrate temperatures. At deposition temperatures below ~630 °C no (103) grains are detectable.

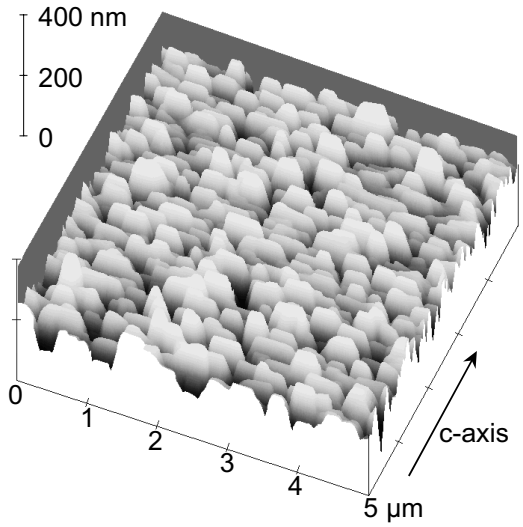

Figure 5.3
Atomic Force Microscopy image of the surface of a (110) YBCO film.

platelets readily discernible in Figure 5.3. They are about 180 nm thick (in *c*-direction) and 700 nm wide, which compares to the $700 \times 700\,\mathrm{nm}^2$ grain size of *c*-axis films. Because the grains are smaller and not as well aligned and grown together as the ones in *c*-axis films, grain boundaries have a more prominent influence on J_c.

The patterning process proved to be more difficult with the (110) films than with the *c*-axis films. Particularly the wet etching step with EDTA reduced the quality (reduction of T_c and increase of ρ_{300}) of a number of films substantially. This increased sensitivity is probably a consequence of the increased ease with which oxygen can leave a sample. Oxygen atoms, which diffuse much faster along the *ab*-plane than in *c*-direction, on average only need to move a distance of half the film thickness (~200 nm) in (110) films to reach the surface rather than half the track width (30 µm) in *c*-axis films. To reduce the risk of loosing oxygen the spun on photoresist was not hardened by heating the sample to the usual 100 °C. After several attempts high quality tracks with a high critical temperature were obtained. The anisotropy of the (110) films within the film plane is also visible at the edges of slightly overetched structures. The etch process is not uniform, but faster along the (110) direction, resulting in the jagged edge visible in Fig 5.4.

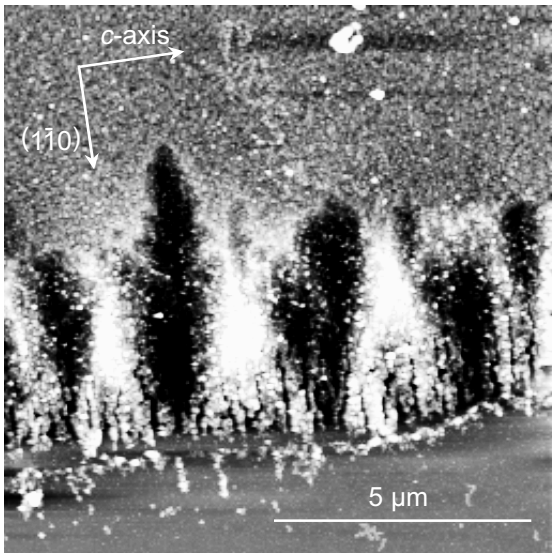

Figure 5.4
AFM image showing the edge of track in a (110) film which has been etched slightly too long (top – film surface, bottom – substrate surface).

Fig. 5.5 shows resistive transition curves of sample 7178/3. Four tracks have been patterned on this film, two in (110) direction and two parallel to the *c*-axis. It is immediately visible that the resistivity in

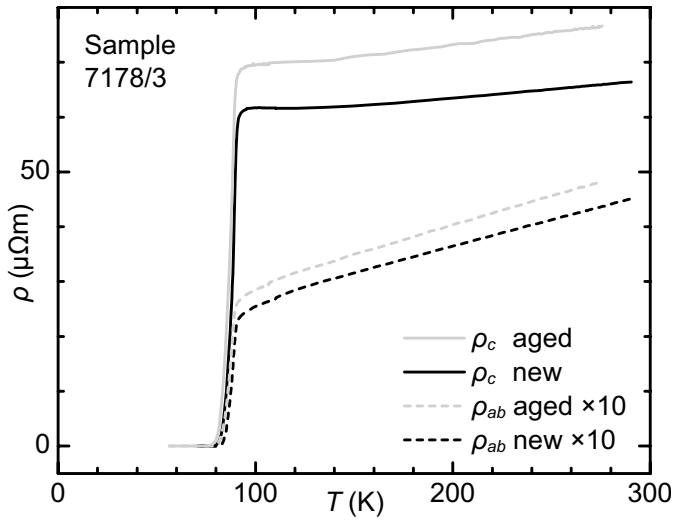

Figure 5.5
Resistive transition of two different tracks on (110) YBCO film patterned in *c*-direction and parallel to the *ab*-plane respectively. During storage of the film for 7 months the resistance increased as shown. (Note that ρ_{ab} is drawn 10 times enlarged; ρ_{ab} (T = 300 K) ≈ 4.7 μΩm.)

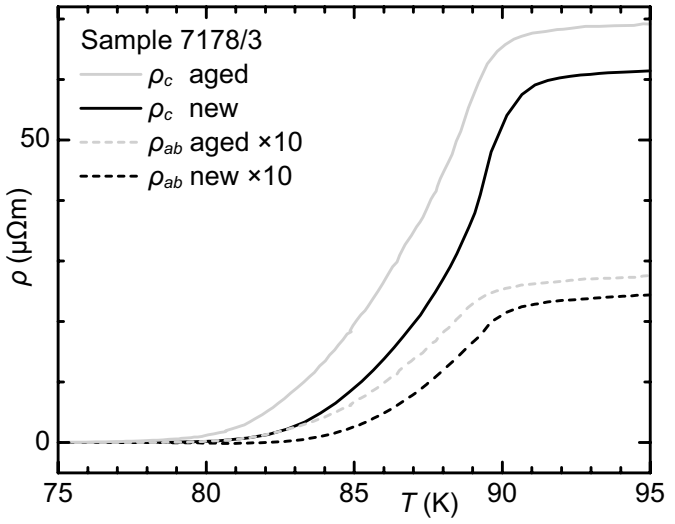

Figure 5.6
Enlargement of Fig. 5.5. The onset of T_c is high at 90 K, but the transition width rather large, indicating a high degree of oxygen disorder.

c-direction is substantially higher than the resistivity within the *ab*-plane (by a factor of 15 at 300 K and 25 at 100 K; for clarity ρ_{ab} is multiplied by 10 in Figs. 5.5 and 5.6). The shape of the two resistivity lines above T_c is different as well: ρ_{ab} decreases linearly with falling temperature, similarly to the resistivity of *c*-axis films, although the intercept is not zero, whereas ρ_c is virtually constant between 100 K and 300 K. Films of lower quality (i.e. films with lower T_c and higher ρ at 100 K) show an increase of ρ_c with falling temperature close to T_c indicating semiconducting behaviour. The critical temperature of (110) films is generally not as high as the T_c of *c*-axis films because of the easy out-diffusion of oxygen and the associated oxygen disorder. This is confirmed by the drop of T_c and the increase of ρ after storage of the sample for several months at ambient conditions (see Figs. 5.5 and 5.6).

5.2 Previous experiments and their interpretations

Although many researchers conducted transport measurements on *c*-axis YBCO films and others developed several models to explain the experimental evidence (see section 4.1), few J_c measurements on *a*-axis or (110) films have been reported. Wu and Chu

(1993; 1994) conducted a series of J_c measurements on *a*-axis, (110) and (113) films. They patterned tracks in various directions on their films, corresponding to different directions relative to the crystal axes, and measured J_c as a function of magnitude and direction of applied field as well as temperature. With all their measurements they kept the applied field normal to the current in the film. In the twinned *a*-axis films, with their differently oriented domains, J_c is always determined by the grains in which the current is flowing parallel to the CuO_2 planes, because $J_c \parallel ab$ (in the following J_c^{ab}) is much larger than $J_c \parallel c$ (J_c^c). At J_c nearly all current is flowing along paths parallel to the CuO_2 planes. The functional dependence of J_c on ϑ ($\varphi = 90°$) is similar to the one observed in *c*-axis films, except that the intrinsic peak is not at $\vartheta = 90°$, but at $\vartheta = 0°$, clearly indicating that J_c depends on the orientation of an applied magnetic field relative to the crystal axis and not relative to the film geometry. Only at higher temperatures they observe a small local maximum at $\vartheta = 90°$, which they ascribe to other pinning centres present in their films or surface pinning. Angular measurements on the (113) films gave rather complicated results which they could explain by the three different domain types present in these films.

Their measurements most relevant to the work here are however the ones on (110) films. Again $J_c^{ab}(\vartheta)$ is similar to J_c in *c*-axis films, but with the intrinsic peak at $\vartheta = 0°$ (i.e. with *B* parallel to the CuO_2 planes). When the current flows in *c*-direction though, the situation is different. $J_c^c(\vartheta)$ is constant (i.e. independent of ϑ), which is not unexpected since *B* is rotated in the *ab*-plane in this experiment. Also this result confirms the dominance of the intrinsic pinning mechanism compared to other pinning effects like growth defects or surface pinning. Hu and Chu measure a J_c^{ab} roughly 60 times larger than J_c^c at low temperatures. This ratio is several times higher than the one observed by magnetic measurements where J_c is calculated using the Bean critical state model (Dinger *et al*., 1987; Senoussi *et al*., 1988). The temperature dependence of J_c^c could be well explained with the assumption that CuO_2 planes are coupled by Josephson tunnelling.

Recently a group at the University of Maryland managed to produce untwinned *a*-axis films on (100) $LaSrGaO_4$, which has a tetragonal crystal structure closely matching the *b*- and *c*-axis constants of YBCO (Takeuchi *et al*., 1995; Trajanovic *et al*., 1995).

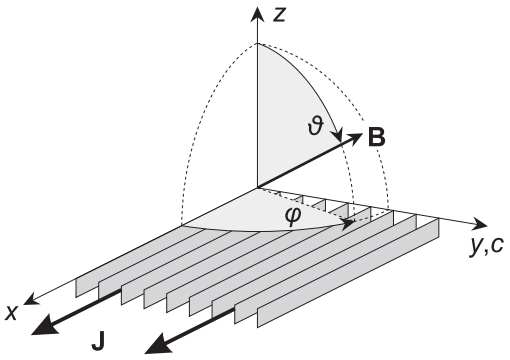

Figure 5.7
Definition of ϑ and φ for experiments on (110) films with the current flowing normal to the *c*-axis.

J_c measurements on these films (Trajanovic *et al.*, 1997) gave results with similar angular field dependencies to the ones observed by Hu and Chu on (110) films. However, additional experiments, where both the current and the applied field were parallel to the *c*-axis, showed that the field orientation relative to the crystal axes has a stronger influence on J_c than the angle between field and current. This is the case for currents flowing parallel to the *ab*-plane as well as in *c*-direction.

5.3 Currents in (110) direction

With the photolithographic methods described in chapter 3 up to four test tracks per sample were patterned parallel and normal to the *c*-axis of (110) films. Because deposition conditions, patterning, oxygenation and the microstructure are very similar for the tracks of one sample, the influence of the current direction relative to the crystal axes

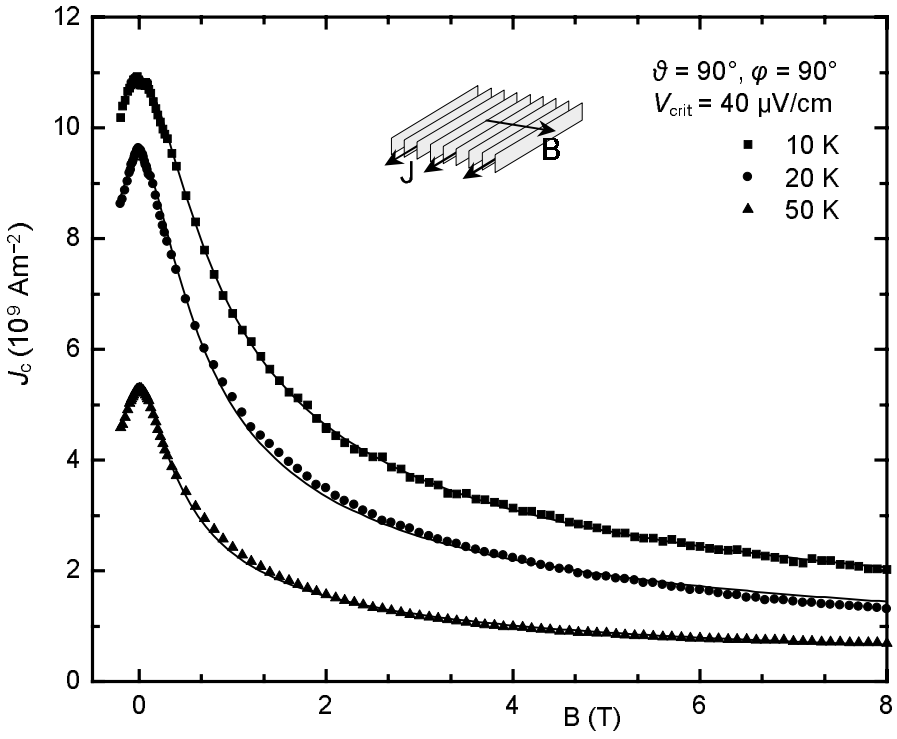

Figure 5.8
$J_c^{ab}(B)$ at 10, 20 and 50 K. The small inset shows a sketch of the geometry of this measurement. The parallel planes symbolise the CuO_2 layers. The arrows show the direction of transport current and applied magnetic field.

can be readily inferred by comparing J_c data obtained from tracks patterned in different directions. In this section and the next J_c measurements are presented with the current flowing normal and parallel to the *c*-axis respectively.

The angles ϑ and φ are again defined relative to the film surface and the current direction (Fig. 5.7), which changes their meaning relative to the crystal axes when compared to *c*-axis films (Fig. 4.4).

The basic symmetry of the critical current anisotropy of (110) YBCO films is similar to the one of *c*-axis films. For a given temperature and magnetic field the maximum J_c is observed in the force free configuration ($B \parallel J$), the minimum J_c when $B \parallel c$ and there is substantially less variation of J_c with B rotating in the *ab*-plane than when B is rotated out of the *ab*-plane (intrinsic pinning). J_c in the (110) films is however much smaller than in the *c*-axis films and the J_c-anisotropy less pronounced. Particularly the extremely sharp intrinsic pinning peaks of J_c at low temperatures and high fields could not be observed in the (110) films. These differences are most likely a consequence of the

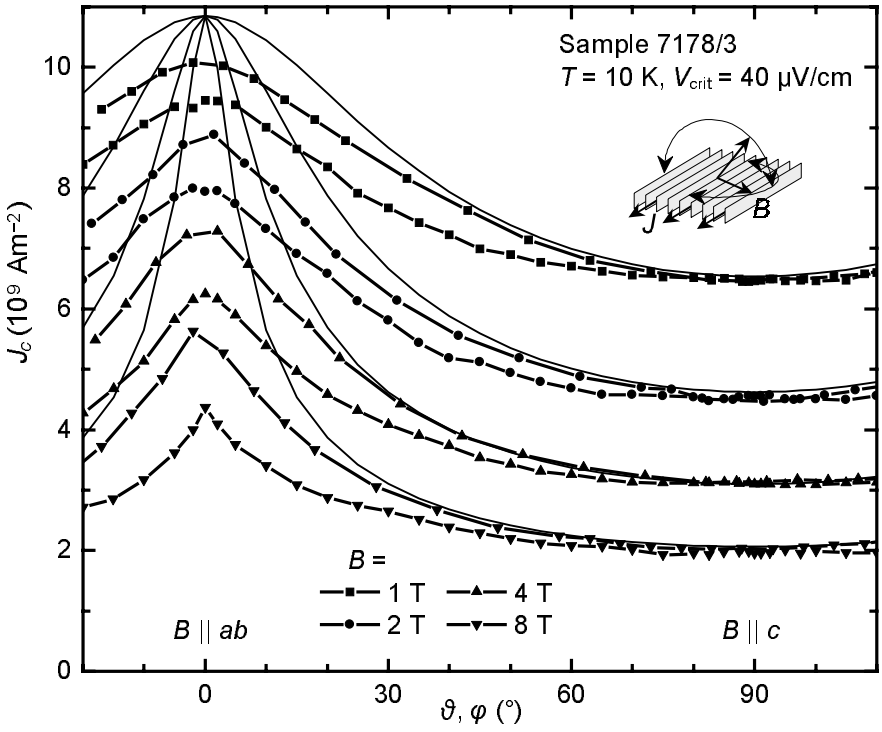

Figure 5.9
J_c of sample 7178/3 at 10 K as a function of magnetic field rotated from parallel to the *ab*-plane ($\vartheta = 0°$, $\varphi = 0°$) to parallel to the *c*-axis ($\vartheta = 90°$, $\varphi = 90°$). The smaller J_c values at each B were measured with ϑ scans at $\varphi = 90°$ (i.e. B always normal to J), whereas the larger values were obtained with φ scans at $\vartheta = 90°$ (i.e. B rotated in the film plane). The insert shows the two scan types.

different microstructure of the two film types (compare Fig. 3.1 and Fig. 5.3). In (110) films the grains are smaller and less well aligned than in *c*-axis films resulting in a much stronger influence of grain boundaries, where in addition the oxygen stoichiometry can be disturbed. This is also reflected in significant zero-temperature intercepts of the $\rho(T)$ curves (see Fig. 5.5; Trajanovic *et al*. (1997)). However, to more clearly see similarities and differences of J_c^{ab} in (110) and *c*-axis films the same tools as in chapter 4 are used to analyse J_c in the following, in particular the 2D model (Equ. (4.2)).

Fig. 5.8 shows J_c as a function of a magnetic field applied in *c*-direction (see insert). The functional dependence can be well described by an inverse power law with an exponent between 0.27 and 0.32 and a cut off at low fields. The absolute value of J_c is substantially smaller than in good *c*-axis films.

J_c measurements on sample 7178/3 at 10 K with B rotated out of the *ab*-plane are plotted in Fig. 5.9. Deviations from the 2D model (thin lines) are large when the field is parallel to the *ab*-plane and no sharp maxima as in *c*-axis films can be observed for these field directions. As stated above, this is probably a result of the different micro-

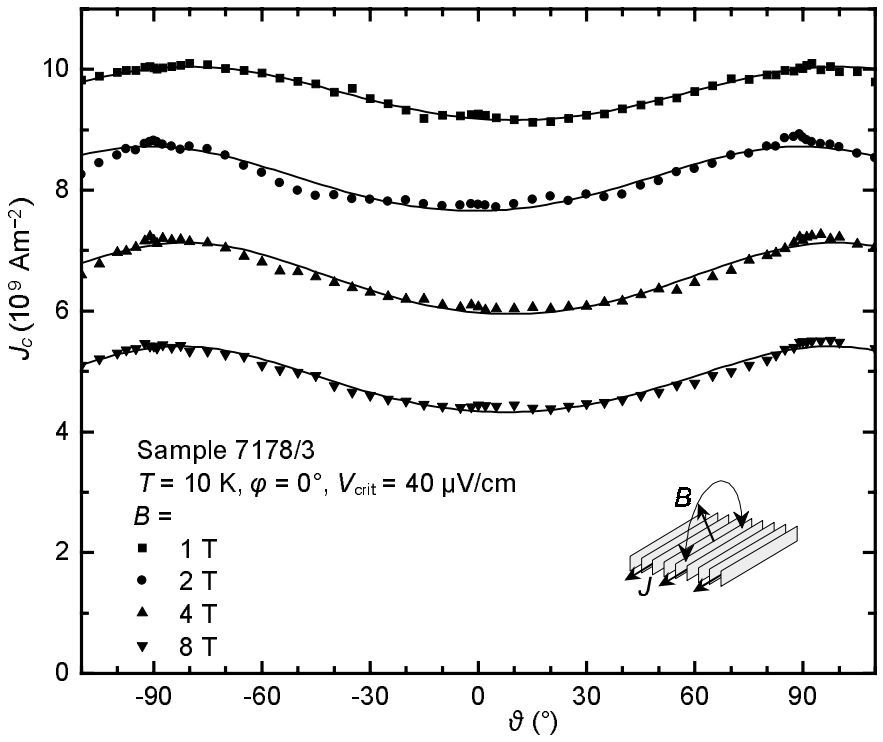

Figure 5.10
J_c of sample 7178/3 as a function of ϑ with $\varphi = 0°$ at 10 K. In this configuration the field remains parallel to the *ab*-plane.

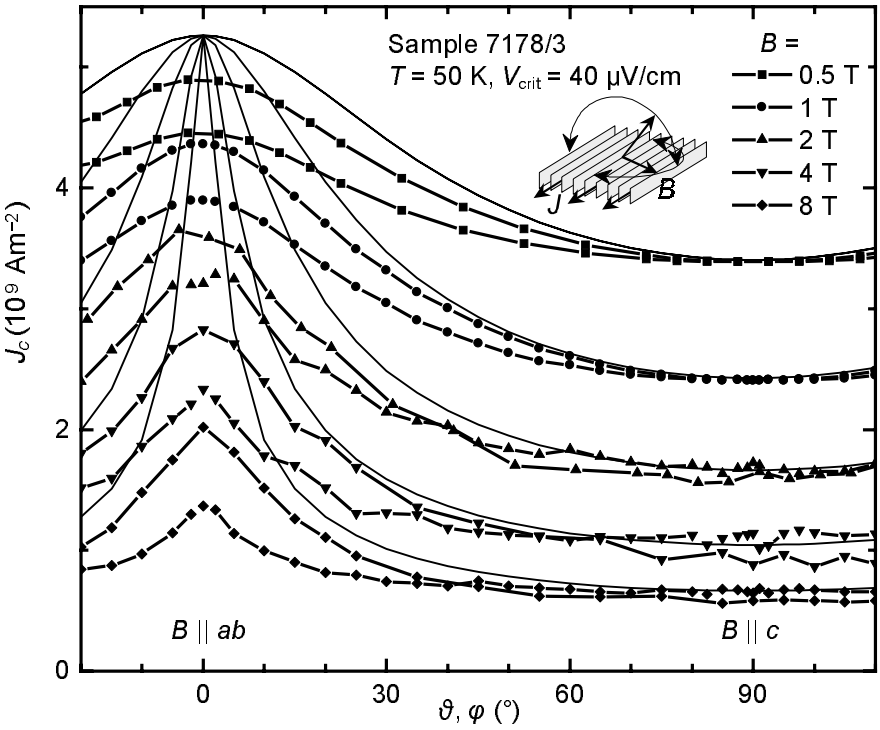

Figure 5.11
J_c of sample 7178/3 at 50 K. The geometry of the plotted scans is the same as the one in Fig. 5.9.

structure. In Fig. 5.10 J_c is plotted for field rotations parallel to the *ab*-plane. The solid lines were calculated with Equ. 4.21 which was found to be widely valid for this con-

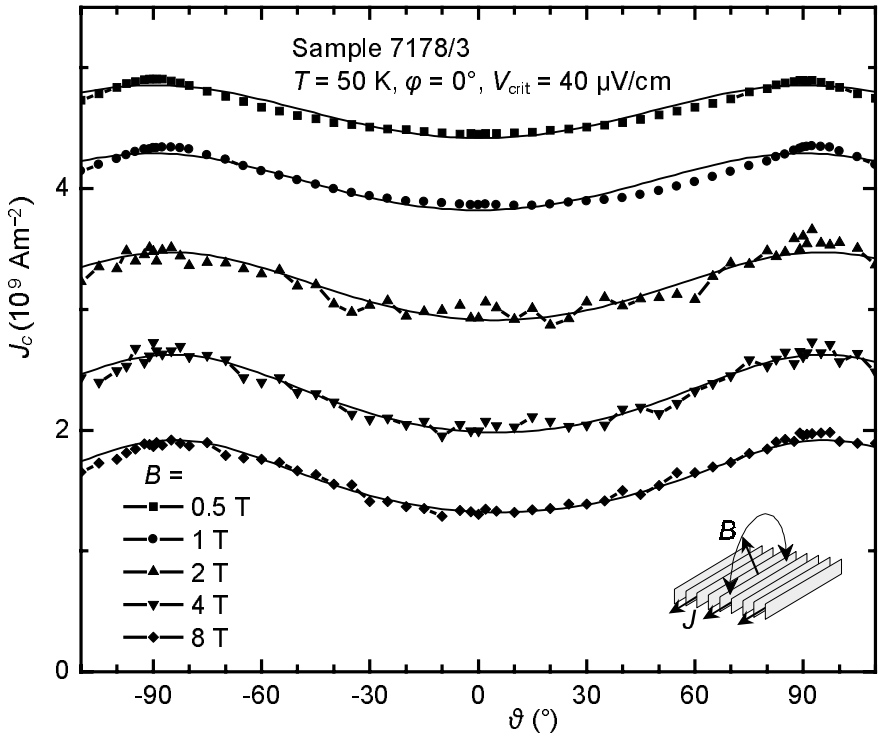

Figure 5.12
J_c of sample 7178/3 as a function of *B* rotated in the *ab*-plane at 50 K (compare Fig. 5.10).

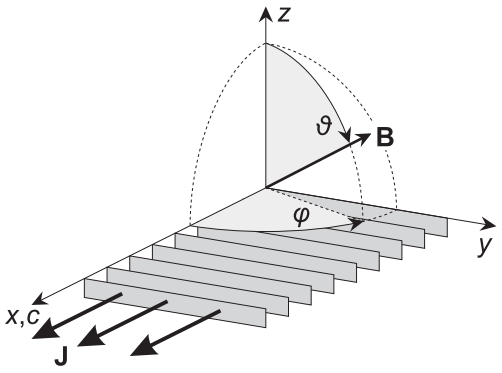

Figure 5.13
Definition of ϑ and φ in (110) films with the current flowing parallel to the *c*-axis.

figuration in *c*-axis films (see section 4.5). Here the agreement between the equation and the data is reasonably good.

At higher temperatures J_c is smaller than at 10 K, but the angular dependence of J_c is similar (see Figs. 5.11 and 5.12). This contrasts the behaviour in *c*-axis films where the sharp intrinsic pinning peaks at low temperatures gradually disappear with rising *T*. Here deviations from the 2D model are already significant at low *T* and thus the behaviour does not change much with *T*.

5.4 Currents in c-direction

A current parallel to the *c*-axis can not flow in the well conducting CuO_2 planes but has to traverse the weaker layers separating them. As a result J_c^c is much smaller than J_c^{ab}. In addition an externally applied magnetic field has a stronger influence on J_c^c.

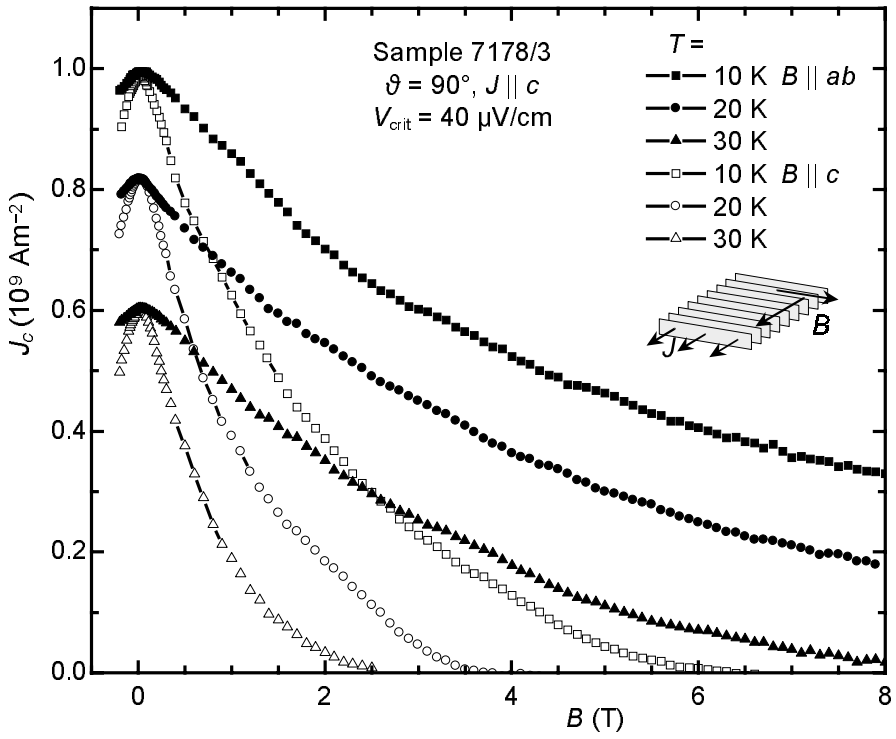

Figure 5.14
J_c^c as a function of *B* applied parallel to the *ab*-plane and the film plane (closed symbols) and parallel to the *c*-axis (open symbols).

Also for experiments with the current parallel to the *c*-axis the angles ϑ and φ are defined by the film plane and the current direction, which again changes their meaning relative to the crystal axes (see Fig. 5.13).

J_c^c as a function of B is shown in Fig. 5.14 where the field is applied parallel to the *c*-axis (open symbols) and parallel to the *ab*-plane (closed symbols). At zero field J_c^c is about an order of magnitude smaller than J_c^{ab}. However, the striking feature is that J_c^c decreases much faster with a field parallel to the *c*-axis than with a field parallel to the *ab*-plane, although the former is the force free configuration and in the latter the macroscopic Lorentz force is maximal. An explanation of this effect in terms of depinning of flux lines by Lorentz forces is therefore not possible.

The unusual behaviour is also reflected in angular J_c measurements when the field is rotated out of the *ab*-plane (Fig. 5.15). Maxima of J_c^c occur when B is parallel to the *ab*-plane ($\vartheta = 0°$) and minima in the force free configuration ($\vartheta = 90°$, $\varphi = 0°$). It appears that even when the current is flowing parallel to the *c*-axis the pancake density, which is determined by the field component parallel to *c*, has the strongest influence on J_c. A partial explanation of this effect could be that the presence of pancake vortices in the

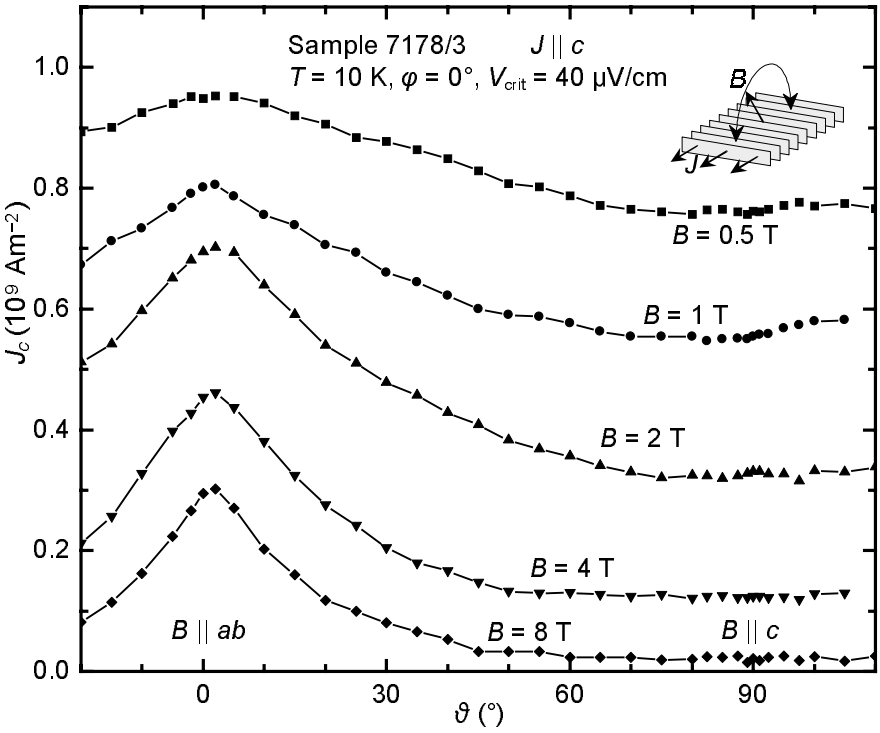

Figure 5.15
J_c^c as a function of ϑ with $\varphi = 0°$ at 10 K. The maximum of J_c^c does not occur at the force free configuration ($J \parallel B \parallel c$) but when the field is parallel to the *ab*-plane ($\vartheta = 0°$).

CuO_2 layers with an associated decrease of the order parameter, reduces the effectively available cross section for the current in *c*-direction. It is rather unlikely that this mechanism can fully account for the effect because ξ_{ab} is smaller than 2 nm below 30 K and the flux line spacing at a field of e.g. 2 T about 35 nm. Thus the order parameter should only be affected at a small fraction of a CuO_2 plane.

J_c^c as a function of *B* rotated within the *ab*-plane is shown in Fig. 5.16. At small fields J_c is independent of ϑ and at high fields a slight maximum occurs for *B* parallel to the film plane ($\vartheta = 90°$), which could be the result of surface pinning effects. The angle independence in this configuration is not unexpected and confirms that the dependencies of J_c on the angle of an applied field presented in this thesis depend on intrinsic properties of YBCO and on the microstructure of the films rather than on geometrical effects associated with the test tracks.

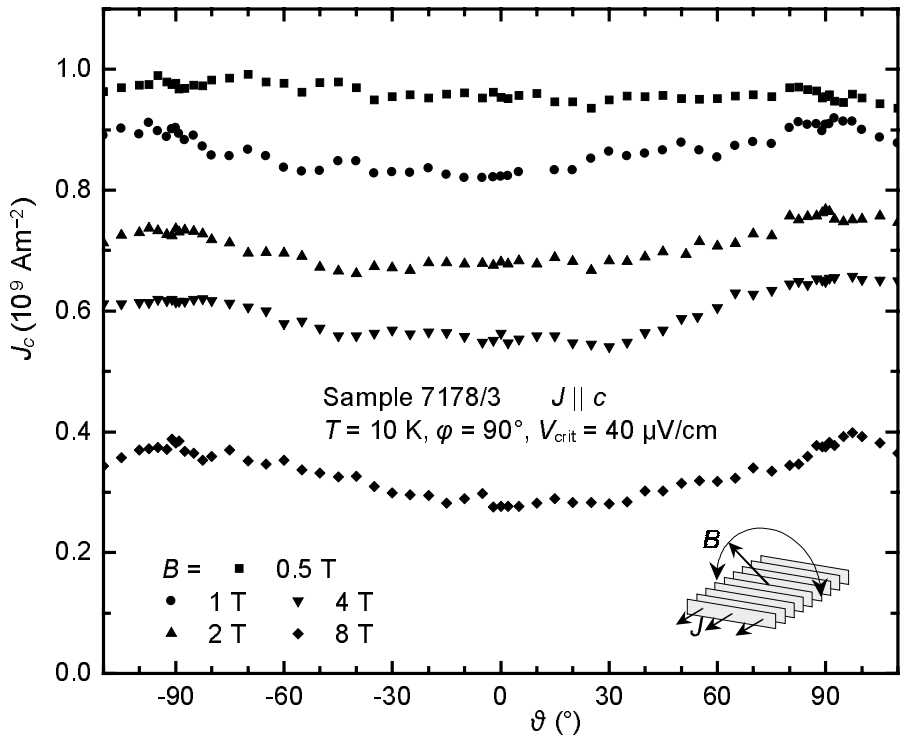

Figure 5.16
J_c^c as a function of ϑ with $\varphi = 90°$ at 10 K. Here the magnetic field is rotated in the *ab*-plane, always normal to *J*.

5.5 Summary

Experiments on (110) films allow the application of a current parallel to the *ab*-plane and parallel to the *c*-axis. In the former case the symmetry of the dependence of J_c on the angle of an applied field is similar to *c*-axis films. The strong intrinsic pinning peaks characteristic of *c*-axis films were however not observed, because the microstructure of the two film types is different. In (110) films the YBCO grains are smaller and not as well aligned as in *c*-axis films. Measurements with the current flowing in *c*-direction revealed the surprising result that J_c^c is smaller in the force free configuration ($B \parallel J \parallel c$) than when the field is normal to *J*. At the moment the mechanism explaining this behaviour is not clear. However, a similar behaviour was recently found by Trajanovic *et al*. (1997) in *a*-axis films deposited on $LaSrGaO_4$.

5.6 References

Dinger, T.R., T.K. Worthington, W.J. Gallagher and R.L. Sandstrom, 1987, Phys. Rev. Lett. **58** (25), 2687-2690.

Inam, A., C. Rogers, R. Ramesh, K. Remschnig, L. Farrow, D. Hart and T. Venkatesan, 1990, Appl. Phys. Let. **57**, 2484.

Senoussi, S., M. Ousséna, G. Collin and I.A. Campbell, 1988, Phys. Rev. B **37** (16), 9792-9795.

Takeuchi, I., Z. Trajanovic, J.L. Peng, Z.Y. Li, P.A. Warburton, C.J. Lobb and T. Venkatesan, 1995, Appl. Phys. Lett. **66**, 1824.

Trajanovic, Z., C.J. Lobb, M. Rajeswari, I. Takeuchi, C. Kwon and T. Venkatesan, 1997, Phys. Rev. B **56** (2), 925-933.

Trajanovic, Z., I. Takeuchi, P.A. Warburton, C.J. Lobb and T. Venkatesan, 1995, Appl. Phys. Lett. **66**, 1536.

Wu, J.Z. and W.K. Chu, 1993, Philosophical Magazine B **67** (4), 587-593.

Wu, J.Z. and W.K. Chu, 1994, Physical Review B **49** (2), 1381-1386.

Chapter 6

Heavy Ion Irradiation of YBCO Films

Several authors have reported on a substantial enhancement of the critical current density due to the introduction of strong pinning centres by heavy ion irradiation of HTS films (Civale *et al*., 1991; Gerhäuser *et al*., 1992; Roas *et al*., 1990; Thompson *et al*., 1992). Fast heavy ions generate strongly oriented, columnar defects along their trajectories. This defect structure is quite different from the one produced by irradiation with lighter particles, like neutrons or protons, which generate smaller, more isotropic point defects or defect cascades (Schindler *et al*., 1992). The flexible possibilities of the two-axis goniometer seemed predestined to investigate the expected complex angular behaviour of these irradiated samples.

6.1 Overview

Many superconductors have been irradiated with a variety of particles, mainly to study the additional pinning by the introduced defects, but also to study their suitability as solenoid wire for magnets in future nuclear reactors (e.g. Herzog *et al*., 1991). Irradiation of type II superconductors can change three basic materials properties: the critical temperature T_c, the upper critical field B_{c2} and the critical current density J_c. T_c is generally reduced as a result of an increase in the normal state resistivity ρ_n, which in turn is inversely proportional to the electron mean free path. When the mean free path is already short prior to irradiation both T_c and ρ_n will not change much. B_{c2} follows a similar decrease as T_c, again depending on a change in ρ_n.

Most experiments investigating the effects of irradiation on superconductors measured the changes to J_c, the parameter not only dependent on the intrinsic material's properties but equally on the microstructure of a given sample. Irradiation is one of several methods to change the microstructure. To achieve very high critical currents the defects, introduced by irradiation or other methods, should ideally have dimensions comparable to the coherence length to maximise the interaction with the flux lines and hence pinning. Substantial enhancements have been observed, particularly in defect free superconducting samples which exhibited a rather small J_c before irradiation.

Unirradiated HTS films are generally able to carry very high supercurrents as grown, indicating a nearly optimal pinning structure. Irradiation with neutrons or protons therefore does not enhance J_c significantly (Schalk *et al.*, 1992). Higher doses destroy a significant volume fraction, eventually reducing J_c. An overview article about radiation effects on superconductors has been written by Weber and Brown (1992).

Irradiation with fast heavy ions has a quite different effect, because of two reasons: Firstly the damage introduced into the films is highly oriented, resulting in an anisotropic change of the pinning behaviour. This artificially introduced anisotropy competes with the intrinsic anisotropy of the layered HTS materials. Secondly the geometry of the defects is similar to the flux lines (long tubes), increasing the defect-flux line coupling, and it is reasonable to expect a much higher increase in J_c compared to the introduction of point defects. The collective pinning theory, explaining pinning of the flux line lattice by a random distribution of point defects is therefore not applicable. In this strong pinning regime critical current densities in the order of the depairing current density J_o ($J_c \approx \alpha J_o$, $\alpha \sim 0.1 - 1$) can be expected (Blatter *et al.*, 1994).

One of the first experiments trying to enhance pinning in HTS materials by heavy ion irradiation was reported by Civale *et al.* (1991). They measured the magnetisation of $YBa_2Cu_3O_{7-\delta}$ single crystals with different doses of 580 MeV ^{116}Sn ions in various temperature, field and field-orientation regimes. Particularly at temperatures close to T_c the critical current densities were increased dramatically, well beyond the increase achieved by proton irradiation in previous experiments. J_c furthermore showed a distinct dependence on the orientation of the applied field. If the field is applied parallel to the irradiation direction, J_c is significantly higher than with the field applied in a symmetrical direction relative to the crystal axes but not aligned with the irradiation direction. The authors conclude that the pinning mechanism is different to pinning by point defects (where the collective pinning theory describes their results well) and that it is most effective at higher fields where thermally activated relaxation is reduced by the larger pinning potential U_p.

Transport current measurements on heavy ion irradiated $YBa_2Cu_3O_{7-\delta}$ films and $YBa_2Cu_3O_{7-\delta}/PrBa_2Cu_3O_{7-\delta}$ superlattices were reported by Holzapfel et al. (1993; 1994). The angular dependence of J_c changes dramatically due to the irradiation of the

YBCO films. The maxima at $\vartheta = \pm 90°$ (intrinsic peaks) are substantially reduced, but even higher maxima appear when the applied field is parallel or antiparallel to the irradiation direction ($T = 79$ K, $B = 1$ T, $\varphi = \varphi_{irr} = 90°$). This change appeared consistently for various irradiation directions ϑ_{irr}. The YBCO/PBCO superlattices on the other hand respond differently to the heavy ion irradiation. There is no change of symmetry of the angular dependence of J_c, merely a change in magnitude. The maxima at $\vartheta = \pm 90°$ are reduced whereas J_c increases for $B \parallel c$ ($\vartheta = 0°$), but there are no particular enhancements for B parallel to the irradiation direction. The authors conclude that the different response to heavy ion irradiation of the YBCO films and the YBCO/PBCO superlattices are a manifestation of their respective dimensionalities. YBCO (at least at temperatures close to T_c) is well characterised by the 3D anisotropic effective mass model, whereas the superconducting layers in the superlattices are only weakly coupled and they essentially behave like 2D superconductors (see section 2.7). In the superlattices the additional pinning is effective for all the directions of the applied field (except B is close to the *ab*-plane).

Apart from the authors mentioned, few other researchers investigated the angular dependence of J_c in heavy ion irradiated HTS films.

6.2 Experiments and Discussion

In a collaboration with the Gesellschaft für Schwerionenforschung in Darmstadt, Germany a small number of samples were irradiated with ^{197}Au ions with an energy of 2.6 GeV. These fast ions have a stopping distance of 50 μm, substantially longer than the thickness of the films. The energy transfer per unit length (≈ 52 keV/nm) exceeds the threshold of 20 keV/nm, beyond which continuous columnar defects are formed along the trajectories (Holzapfel *et al.*, 1993). The ions generate straight amorphous tubes with a diameter of 8 nm. In order to break the symmetry present in the $J_c(B,\vartheta,\varphi)$ data the samples were irradiated from a direction not lying in a major plain of the crystal axes of the patterned film (see Figs. 4.3 and 6.6). The irradiation direction has the spherical coordinates ϑ_{irr} and φ_{irr}. An irradiation time of several minutes resulted in a fluence of 1.5×10^{11} ions·cm^{-2}, corresponding to a dose equivalent field or matching field B_Φ of 3 T (B_Φ is the field where the flux line density is equal to the density of columnar defects.). This dose is high enough to introduce significant additional pinning, but

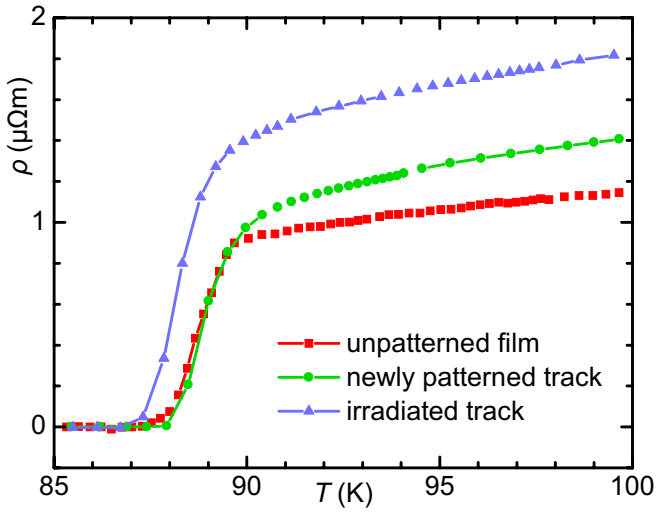

Figure 6.1
Resistive transition of sample 6017/1 before and after irradiation. (The geometry for the measurement of the unpatterned film is estimated)

destroys only about 8 % of the volume of the film and has therefore little effect on T_c. The resistive transition curves for film 6017/1 are shown in Fig. 6.1. T_c dropped only by 1 K due to the irradiation.

Fig. 6.2 shows the critical current density of sample 6017/1 as a function of ϑ for various applied fields at 40 K ($\varphi = 90°$). Fig. 6.3 shows J_c of the same film before irradiation. At low fields J_c is enhanced by a factor of 1.3 − 2.4, most markedly for ϑ close to the irradiation direction ϑ_{irr}. Figure 6.2 very clearly shows how the two dominant pinning mechanisms – intrinsic pinning and strong pinning by the columnar defects – compete at different applied fields. At fields much smaller than the matching

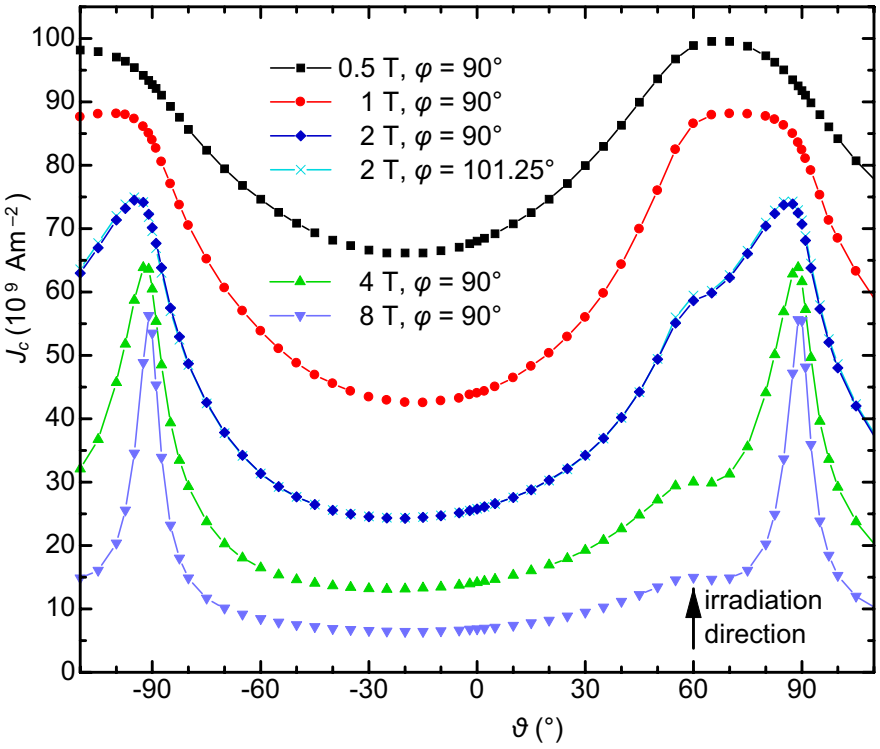

Figure 6.2
$J_c(\vartheta)$ of irradiated sample 6017/1 at 40 K and various applied fields. ϑ_{irr} is marked by an arrow. At 2 T an additional measurement with $\varphi = \varphi_{irr} = 101.25°$ showed virtually no difference to the measurement with $\varphi = 90°$. A voltage criterion of 40 μVcm^{-1} was used.

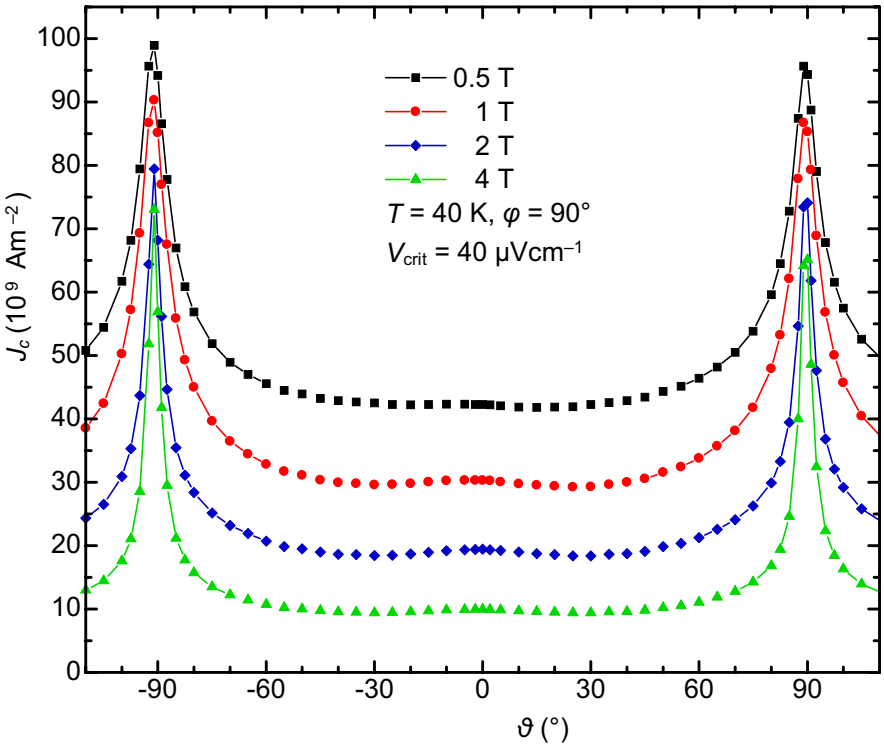

Figure 6.3
$J_c(\vartheta)$ of sample 6017/1 before irradiation at 40 K and various applied fields.

field ($B \ll B_\Phi$) the critical current is maximal when the field is aligned with the irradiation direction. The flux line density is low and virtually all vortices are pinned by the columnar defects along their whole length. The volume pinning force can be obtained by a direct summation of the pinning forces per flux line. There is no local maximum of J_c at $\vartheta = \pm 90°$. At $B \gg B_\Phi$ on the other hand, intrinsic pinning becomes dominant again and there is only a small anisotropic increase of J_c associated with the columnar defects (Figs. 6.2 and 6.3). If $B \approx B_\Phi$, both pinning mechanisms contribute about equally to pinning and J_c and the resulting angular behaviour becomes rather complex (Gerhäuser *et al.*, 1992).

To gain more insight into this situation the applied magnetic field was scanned over the whole unit sphere. Results are shown in Fig. 6.4. For a number of angles ϑ from 40° to 90° J_c was measured as a function of φ (φ-scans, $-180 < \varphi < 180$). It can be seen that the irradiation changed the symmetry of the data considerably. For $\vartheta \leq \vartheta_{irr}$ ($\vartheta_{irr} = 60°$) there is only one maximum of J_c per revolution of φ, but for $\vartheta_{irr} < \vartheta \leq 90°$ gradually two maxima appear from the one at $\varphi = \varphi_{irr}$ ($\varphi_{irr} = 101°$). These maxima shift to $\varphi = 0°$ and $\varphi = 180°$ for $\vartheta = 90°$, where the symmetry is the same as in the unirradiated samples. For

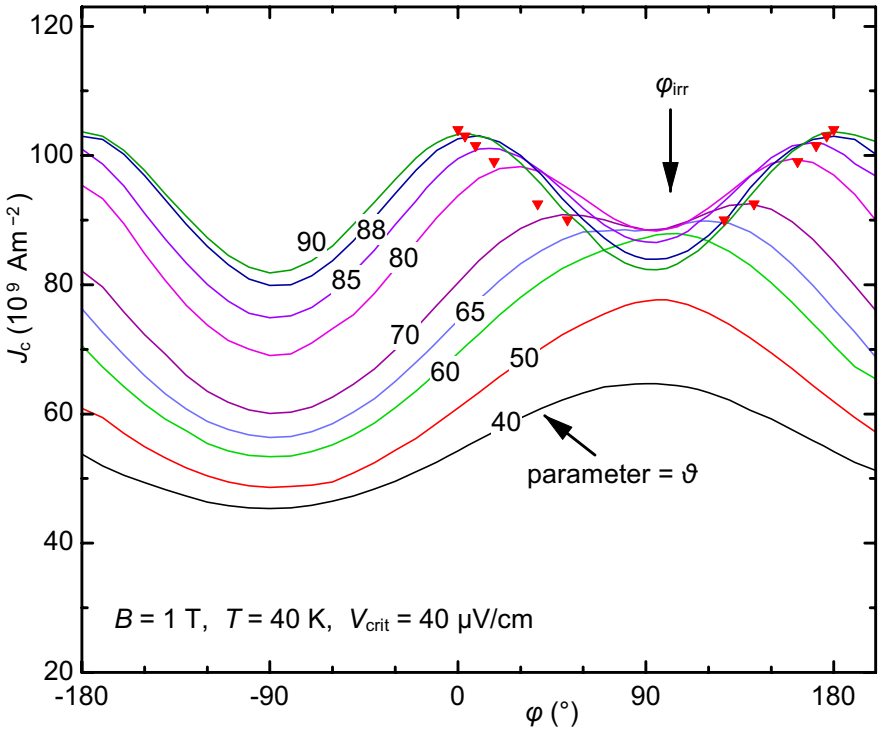

Figure 6.4
J_c as a function of φ of the irradiated film 6017/1. The irradiation angles are $\vartheta_{irr} = 60°$ and $\varphi_{irr} = 101.25°$.

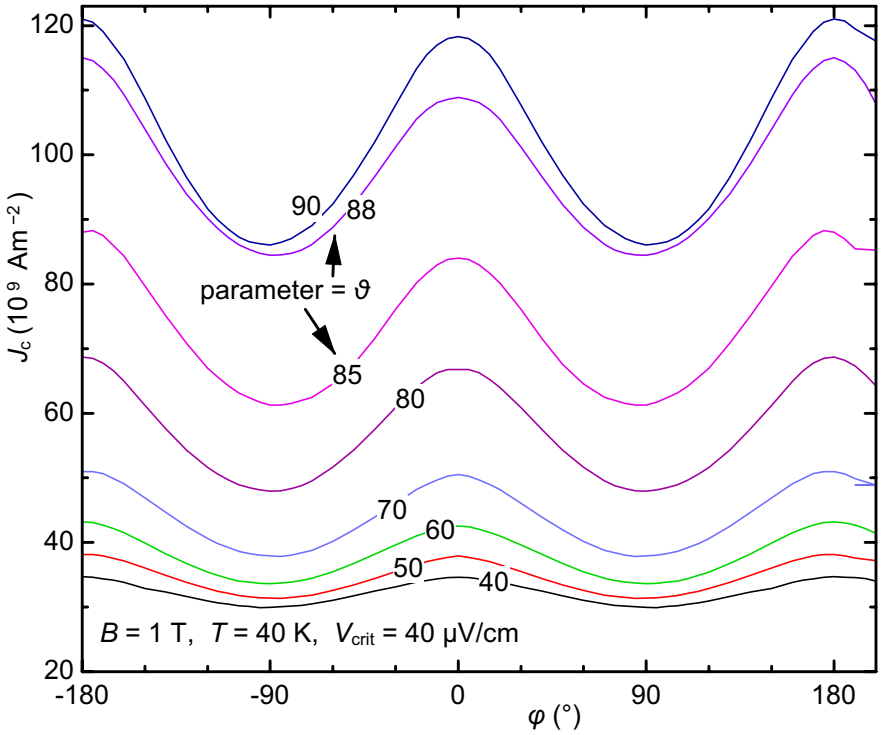

Figure 6.5
J_c as a function of φ of film 6017/1 before irradiation.

comparison results of measurements on the sample previous to irradiation are plotted in Fig. 6.5.

The geometry of this experiment is rather complex. The sketch in Fig. 6.6 illustrates the variables influencing pinning and J_c in the irradiated samples. The incident ions move in direction $\mathbf{e}_{irr}$ when they hit the sample and the orientation of the resulting columnar defects is consequently parallel to $\mathbf{e}_{irr}$ ($\mathbf{e}_{irr}$ and $-\mathbf{e}_{irr}$ are equivalent for the purposes of pinning). $\mathbf{e}_{irr}$ nearly lies in the *yz*-plane for sample 6017/1.

A possible mechanism to explain the complicated symmetry shown in Fig. 6.4 is illustrated in Figs. 6.7 – 6.10. The assumption is that for a given angle ϑ pinning of the penetrating flux lines is strongest if the component of the Lorentz-force along the irradiation direction $\mathbf{e}_{irr}$ is minimal. Each of the Figs. 6.7 – 6.10 depicts a different case. If ϑ is smaller than ϑ_{irr} then the component of the Lorentz force in irradiation direction $F_{Lirr} = |\mathbf{F}_L \cdot \mathbf{e}_{irr}|$ is larger than zero for all angles φ. There is one maximum of F_{Lirr} ($\mathbf{F}_{Lr}$ in Fig. 6.7, $\varphi = 270°$) and one minimum ($\mathbf{F}_{Lp}$ in

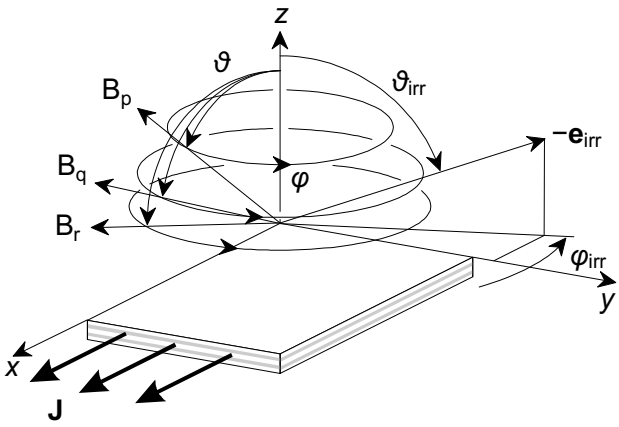

Figure 6.6
Geometry of φ-scan measurements of irradiated samples: $\mathbf{e}_{irr}$, irradiation direction; **J**, current density. The external field **B** is scanned along the sketched circles for various polar angles ϑ.

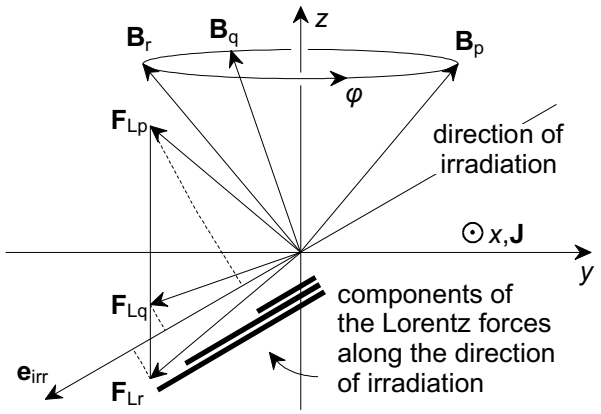

Figure 6.7
Applied magnetic fields and Lorentz forces. The Lorentz force $\mathbf{F}_L$ always lies in the *yz*-plane because the current flows in *x*-direction and $\mathbf{F}_L \perp \mathbf{J}$. $\vartheta = 40° < \vartheta_{irr}$; $|\mathbf{F}_L \cdot \mathbf{e}_{irr}| > 0$ for all angles φ.

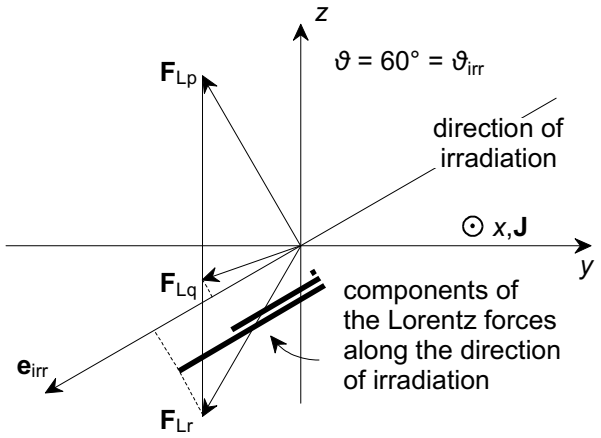

Figure 6.8
Like Fig. 6.7, but $\vartheta = 60° = \vartheta_{irr}$. When $\mathbf{B} \parallel \mathbf{e}_{irr}$, $\mathbf{F}_L$ is normal to $\mathbf{e}_{irr}$ (case $\mathbf{F}_{Lp}$) and there is no component of $\mathbf{F}_L$ along $\mathbf{e}_{irr}$.

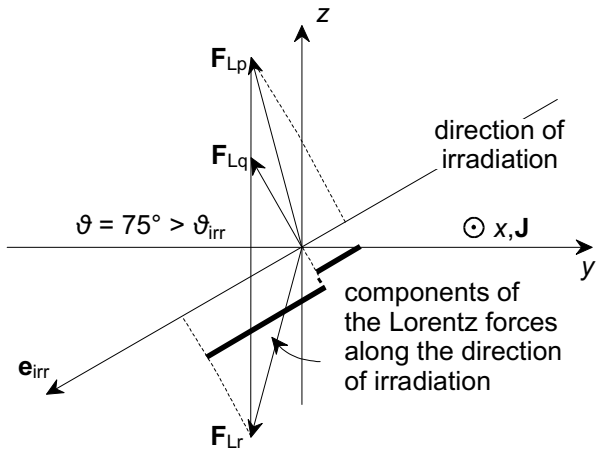

Figure 6.9
Like Fig. 6.7, but $\vartheta = 75° > \vartheta_{irr}$. There are two angles φ for which $\mathbf{F}_L$ is normal to $\mathbf{e}_{irr}$ (case $\mathbf{F}_{Lq}$).

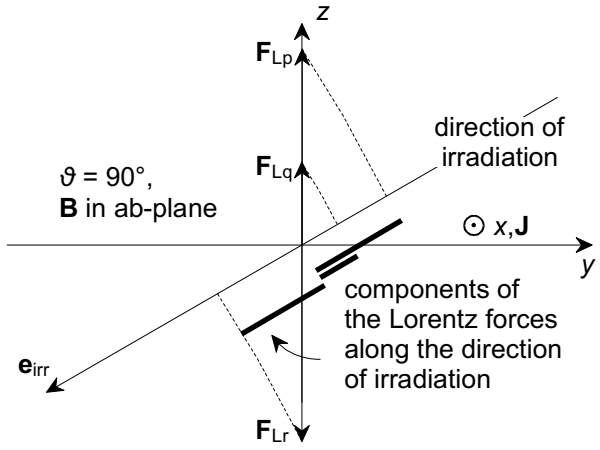

Figure 6.10
Like Fig. 6.7, but $\vartheta = 90°$, **B** lies in the *ab*-plane. When $\mathbf{B} \parallel \mathbf{J}$ $\mathbf{F}_L$ and therefore the projection of $\mathbf{F}_L$ onto $\mathbf{e}_{irr}$ is 0.

Fig. 6.7, $\varphi = 90°$), corresponding to a minimum and a maximum in J_c respectively. In Fig. 6.8 the case with $\vartheta = \vartheta_{irr}$ is drawn. There is still only one minimum and one maximum but for $\varphi = \varphi_{irr}$ the flux lines are exactly aligned with the defects and the strong effective pinning can be seen by a pronounced maximum in J_c. For $\vartheta_{irr} < \vartheta \leq 90°$ there always exist *two* angles φ_o for which $F_{Lirr} = 0$. At these angles φ_o maxima appear in $J_c(\varphi)$ and in between, where F_{Lirr} is maximal, there are two local minima. When **B** is finally rotated in the *ab*-plane ($\vartheta = 90°$, Fig. 6.10) a more symmetric configuration emerges again. This is because a rotation in φ of 180° is equal to an inversion of **B**, which is always a symmetry operation.

More formally the situation is described by the following equations. Local maxima or minama in $J_c(\varphi)$ appear where F_{Lirr} has extrema.

$$F_{Lirr} = \left|\mathbf{e}_{irr} \cdot \mathbf{F}_L\right| = JB \left| \sin\vartheta \sin\varphi \cos\vartheta_{irr} - \cos\vartheta \sin\vartheta_{irr} \sin\varphi_{irr} \right| \qquad (6.1)$$

To obtain all extrema of F_{Lirr}, an absolute of a function, it is easiest to evaluate

$$\frac{\partial F_{Lirr}^2}{\partial \varphi} = 2(\sin\vartheta \sin\varphi \cos\vartheta_{irr} - \cos\vartheta \sin\vartheta_{irr} \sin\varphi_{irr}) \sin\vartheta \cos\vartheta \cos\varphi = 0 . \qquad (6.2)$$

There are two solutions for φ to this equation if $\vartheta < \vartheta_{irr}$ and 4 if $\vartheta > \vartheta_{irr}$. They are $\varphi_{1/2} = \pm 90°$ and, if the solutions exist, $\varphi_{3/4} = \arcsin(\tan\vartheta \sin\varphi_{irr} / \tan\vartheta)$. For $\vartheta < \vartheta_{irr}$ the

two solutions are the maximum at +90° and the minimum at –90°. For $\vartheta > \vartheta_{irr}$ the local maximum at +90° becomes a second minimum and the two new solutions $\varphi_{3/4}$ are both maxima. Their location depends on the angle ϑ and the direction of irradiation (ϑ_{irr}, φ_{irr}). For sample 6017/1 the calculated values of $\varphi_{3/4}$ are marked by downwards pointing triangles in Fig. 6.4 close to the maxima of the curves with $\vartheta > \vartheta_{irr} = 60°$. The agreement is good for ϑ close to 90°. For $\vartheta \approx \vartheta_{irr}$ and $\varphi \approx \varphi_{irr}$ the flux lines are nearly parallel to the columnar defects and the extremum at $\varphi = 90°$ shifts towards $\varphi = \varphi_{irr}$.

The macroscopic model described in the previous paragraphs is able to explain the symmetry of the observed $J_c(\varphi)$. It is however clear that the detailed microscopic interplay between intrinsic pinning by the layered structure of the material, pinning by microstructural defects of the samples and pinning by the artificially introduces columnar defects is complex. An attempt to shed some light on possible microscopic mechanisms is presented in the following.

Fig. 6.11 shows a cross section of a sample parallel to the *zy*-plane with flux lines (or better flux line cores) for various directions of applied magnetic field. If the field is applied in a direction roughly normal to $\mathbf{e}_{irr}$ (I), the elongated shape of the irradiation defects is not relevant. Pinning of the flux lines is nevertheless enhanced by nearly a factor of two (see Figs. 6.4 and 6.5). In this configuration the columnar defects have a similar effect to other point defects of comparable lateral dimensions (Holzapfel *et al.*, 1993). In configuration II, which is symmetric to I in an unirradiated sample, a substantial part of the flux line core passes through the columnar defect. This part is strongly pinned and J_c therefore larger than in I. When J is ramped up in an experiment and

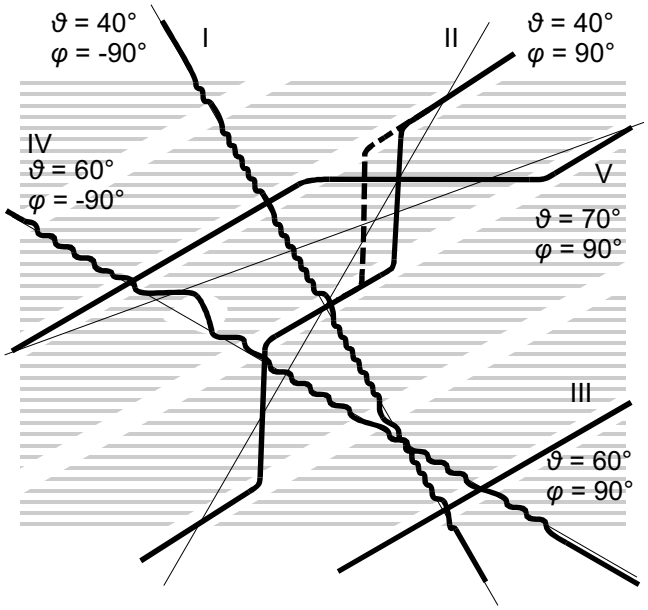

Figure 6.11
Flux lines penetrating a heavy ion irradiated sample at different angles. Gray horizontal lines are CuO layers; columnar defects are drawn white, the flux line cores black. See text for details.

approaches J_c the parts of the flux lines penetrating not damaged material very likely start to move first, in the way indicated by the dashed line for flux line II in Fig. 6.11. For $\vartheta = \vartheta_{irr}$ flux lines III and IV show the two extrema $\varphi = \varphi_{irr}$ and $\varphi = \varphi_{irr} + 180°$. In the first case (III) all the flux lines are entirely pinned by the columnar defects if the applied field is smaller than the matching field. The effect of the columnar defects is visible in Fig. 6.4 with the $\vartheta = 60°$ scan having it's maximum not at $\varphi = 90°$ but at $\varphi = \varphi_{irr}$, but the broadness of the peak suggests that the activation energy needed to depin a flux line is not very different from the one of a slightly misaligned flux line. Several authors (Blatter *et al*., 1994; Gerhäuser *et al*., 1992) suggest a mechanism of flux line movement in this situation where a part of a flux line moves to a neighbouring columnar defect, forming a loop. Subsequently the loop expands in a manner similar to the movement of a misaligned flux line as described earlier. Flux line IV on the other hand is pinned in a similar way to flux line I, the main difference being a smaller B_z component, requiring less pancake vortices to be pinned. This relationship between I and IV is similar in the unirradiated case. Like for flux line I pinning is enhanced by the columnar defects introduced by irradiation. It is important to consider other defects working as pinning centres as well. Flux line IV is drawn crossing a small void in the left half of the picture.

Flux line V is an example of a flux line with $\vartheta > \vartheta_{irr}$. The main difference to flux lines with $\vartheta < \vartheta_{irr}$ is the absence of flux line segments threading the superconducting layers. Flux lines only consist of Josephson vortices between CuO layers and segments embedded in the columnar defects. The B_z component of the flux line is entirely provided by the latter. Again the flux lines move by the nucleation of small loops or kinks and their subsequent expansion. It is interesting that heavy ion irradiation reduced the critical current for fields applied parallel to the *ab*-plane, particularly in the force free configuration. This effect could also be observed by others (Holzapfel *et al*., 1993). It has been suggested that the columnar defects facilitate the formation of loops and kinks for the flux lines pinned by the intrinsically layered structure of the material. The sharp peaks of the $B \parallel ab$-plane configurations have all been reduced by heavy ion irradiation so far.

Heavy ion irradiation of High-T_c thin films has proven to be an effective method to enhance pinning and therefore the current carrying capacity of these materials. In

particular it is possible to enhance J_c for the $B \parallel c$-axis configuration where the J_c minimum in unirradiated films occurs. This effectively reduces the strong intrinsic anisotropy.

Detailed angular measurements revealed a complex structure of $J_c(\vartheta,\varphi)$ which could be explained by a simple model. It is however clear that the behaviour of the flux lines at a microscopic level is very complex and influenced by at least three different types of pinning mechanisms: Intrinsic pinning by the layered structure of the crystal lattice, the microstructure of a particular sample and the artificially introduced columnar defects.

6.3 References

Blatter, G., M.V. Feigel'man, V.B. Geshkenbein, A.I. Larkin and V.M. Vinokur, 1994, Reviews of Modern Physics **66** (4), 1125-1388.

Civale, L., A.D. Marwick, T.K. Worthington, M.A. Kirk, J.R. Thompson, L. Krusin-Elbaum, Y. Sun, J.R. Clem and F. Holtzberg, 1991, Phys. Rev. Lett. **67** (5), 648-651.

Gerhäuser, W., G. Ries, H.W. Neumüller, W. Schmidt, O. Eibl, G. Saemann-Ischenko and S. Klaumünzer, 1992, Phys. Rev. Lett. **68** (6), 879-882.

Herzog, R., H.W. Weber, R.T. Kampwirth, K.E. Gray and H. Gerstenberg, 1991, Journal of Applied Physics **69**, 3172.

Holzapfel, B., G. Kreiselmeyer, M. Kraus, G. Saemann-Ischenko, S. Bouffard, S. Klaumünzer and L. Schultz, 1993, Physical Review B **48** (1), 600-603.

Holzapfel, B., M. Leghissa, P. Bauer, G. Kreiselmeyer, M. Kraus, S. Bouffard, L. Schultz and G. Saemann-Ischenko, 1994, Journal of Superconductivity **7** (1), 205-207.

Roas, B., B. Hensel, S. Henke, S. Klaumünzer, B. Kabius, W. Watanabe, G. Saemann-Ischenko, L. Schultz and K. Urban, 1990, Europhys. Lett. **11** (7), 669-674.

Schalk, R.M., H.W. Weber, Z.H. Barber, C.E. Davies, J.E. Evetts, R.E. Somekh and D.H. Kim, 1992, Supercond. Sci. Technol. **5** (S1), S224-S227.

Schindler, W., P. van Haßelt, G. Saemann-Ischenko, G. Kumm, K. Winzer, B. Holzapfel, B. Roas, W. Gieres and H. Gerstenberg, 1992, Supercond. Sci Technol. **5**, S129-132.

Thompson, J.R., Y.R. Sun, H.R. Kerchner, D.K. Christen, B.C. Sales, B.C. Chakoumakos, A.D. Marwick, L. Civale and J.O. Thompson, 1992, Appl. Phys. Lett. **60** (18), 2306-2308.

Weber, H.W. and B.S. Brown, 1992, Radiation Effects on Superconducting Materials. *Concise Encyclopedia of Magnetic & Superconducting Materials (Advances in Materials Science and Engineering)*. J. E. Evetts, Ed., Pergamon Press, 453-457.

Chapter 7

Conclusions and Future Directions

The understanding of the dependence of J_c on the direction of an applied magnetic field in YBCO was the aim of the work presented in this thesis. To enable experiments to be conducted with all possible combinations of field and current directions, both relative to each other and to the crystal axes, J_c was determined by transport measurements on YBCO thin films. A purpose-built two axis goniometer allowed the application of a field up to 8 T in any direction to the sample.

7.1 Conclusions

The field dependence of J_c in YBCO films exhibits a rich structure, which can only be understood if the layered structure of this HTS ceramic compound is explicitly taken into account, as a comparison of J_c data from *c*-axis films and several models for the J_c behaviour showed. The experimental data is best described by the 2D model proposed by Kes *et al*. (1990), which is based on the Lawrence-Doniach (1970) model of layered superconductors. A description in terms of the anisotropic Ginzburg-Landau theory is not sufficient. The 2D character is particularly visible at low temperatures where the CuO_2 layers are only weakly coupled, because the coherence length in *c*-direction is smaller than the layer spacing.

In the 2D model J_c is only determined by the density of pancake vortices, which is directly related to the field component parallel to the *c*-axis. At low temperatures the coupling between adjacent pancake vortices is weak and strings connecting them are well pinned by the intrinsic pinning potential. In this regime the agreement between the data and the 2D model is accurate and hence the pinning characteristics are governed by the pinning of pancake vortices. At high temperatures the experimental critical current values fall below the expectation of the 2D model. Two mechanisms contributing to this reduction of J_c have been identified. The first is observable when no Lorentz force is acting on the flux line strings parallel to the *ab*-plane ($\varphi = 0°$) and is related to the different coupling of pancakes for flux lines parallel to the *c*-axis ($\vartheta = 0°$) and tilted ones ($\vartheta > 0°$). The second mechanism relates to the presence of a Lorentz force on

vortex string segments adjacent to a pancake vortex ($\varphi > 0°$). The force on these string segments causes a reduction of the effective pinning force available for the pancake vortices. Characteristic parameters of the two effects are the displacement of two neighbouring pancakes w and the Lorentz force component in c-direction F_L^z respectively. The influence of F_L^z can be deduced with J_c measurements as a function of φ at constant ϑ. A model of a single pancake vortex, which was explained in section 4.4, is in good agreement with $J_c(\varphi)$ data obtained within a large range of parameter values. In deoxygenated YBCO films, where the coupling between layers is further reduced, deviations from the 2D model appear at higher temperatures (~20 K) than in fully oxygenated films.

Experiments on (110) YBCO films confirmed that the basic symmetry of the J_c^{ab} dependence on the direction of an applied field is firmly related to the orientation relative to the crystal axes and not merely a result of the particular geometry of current tracks in c-axis films. However, because of the different microstructure of the two sample types, the J_c dependence deviates in some details. Specifically the sharp peaks of J_c, which are related to intrinsic pinning and the 2D behaviour in c-axis films, could not be observed in (110) films. J_c measurements with the current parallel to the c-axis surprisingly showed that the J_c minimum again occurs if the field is applied parallel to the c-axis, which is the force-free configuration in this geometry. A similar observation has been recently made on a-axis films with the c-axis of all grains aligned in one direction within the ab-plane (Trajanovic *et al.*, 1997). A possible partial explanation of this behaviour is the reduction of the effective superconducting cross section of the current track by the presence of pancake vortices.

The angular dependence of J_c in c-axis films irradiated with heavy ions is strongly affected by the introduced columnar defects. If the field lines up with the direction of the defects the additional correlated pinning leads to an enhancement of J_c. The change of pinning resulting from the irradiation is significantly more pronounced below the matching field B_Φ, where the defect density equals the flux line density, than above B_Φ.

7.2 Future directions

The full range of phenomena of flux lines and their pinning in the HTS is extremely large and complex (Brandt, 1995; Blatter *et al.*, 1994). It is clear that the work presented

in this thesis can only contribute a very small increment to the already remarkably large body of knowledge, which is nevertheless far from complete. To further the understanding of critical currents in YBCO films, a future investigation could address a number of concrete questions which emerged from the experimental evidence presented in the previous chapters.

Measurements of J_c^c (J_c with J parallel to the c-axis) in (110) films and in a-axis films on $LaSrGaO_4$ (Trajanovic *et al.*, 1997) surprisingly revealed that a minimum of J_c^c occurs when an applied field is parallel to the c-axis. This result is difficult to understand in terms of conventional flux-pinning mechanisms. A study systematically relating the microstructure of (110) films (with possibly larger and better aligned grains) and c-axis films to $J_c(\vartheta,\varphi)$ could clarify the origin of this effect. Such an investigation would also shed some light on the reasons for the differences of J_c^{ab} in c-axis and (110) films.

A result of this thesis with a wide range of validity is the relation for the φ-dependence of J_c in c-axis films (Equ. (4.21)), which was obtained by making full use of the 2-axis goniometer. A model of a single pancake shows how a Lorentz force acting on a flux line in c-direction can reduce J_c and explain the functional dependence of $J_c(\varphi)$. In the derivation of the model a number of simplifications were used, which, although they seem reasonable, could be avoided by additional calculations and numerical simulations. An extension of the model considering the interaction of several pancakes would be desirable.

A large area only mentioned at the periphery of this thesis are all effects of thermal activation (flux creep, thermally activated flux flow etc.) and the related phases of the flux line lattice (vortex glass, vortex liquid etc.). These questions are of considerable theoretical interest as well as being of practical importance for applications of YBCO at 77 K. They could be explored by systematic and accurate current-voltage measurements (*IV*-curves), as Berghuis *et al*. (1996) have shown for fields applied parallel to the c-axis. Measurements close to T_c, where ξ_c exceeds the spacing of the CuO_2 planes, should show if the explicit influence of the layering of the crystal structure disappears and the anisotropic Ginzburg-Landau theory is sufficient to describe the superconducting behaviour of YBCO.

7.3 References

Berghuis, P., R. Herzog, R.E. Somekh, J.E. Evetts, R.A. Doyle, F. Baudenbacher and A.M. Campbell, 1996, Physica C **256**, 13-32.

Blatter, G., M.V. Feigel'man, V.B. Geshkenbein, A.I. Larkin and V.M. Vinokur, 1994, Reviews of Modern Physics **66** (4), 1125-1388.

Brandt, E.H., 1995, Reports On Progress In Physics **58** (11), 1465-1594.

Kes, P.H., J. Aarts, V.M. Vinokur and C.J. van der Beek, 1990, Phys. Rev. Lett. **64** (9), 1063-1066.

Lawrence, W.E. and S. Doniach, 1970, 12th Int. Conf. on Low Temperature Physics, Kyoto, Keigaku, Tokyo 1970.

Trajanovic, Z., C.J. Lobb, M. Rajeswari, I. Takeuchi, C. Kwon and T. Venkatesan, 1997, Phys. Rev. B **56** (2), 925-933.

List of publications

Berghuis, P., F. Baudenbacher, R. Herzog, R.E. Somekh, A.M. Campbell, J.E. Evetts and G. Wirth, 1996a, 8th IWCC in Superconductors, Kitakyushu, Japan, World Scientific, Singapore, 1996.

Berghuis, P., R. Herzog, R.E. Somekh, J.E. Evetts, R.A. Doyle, F. Baudenbacher and A.M. Campbell, 1996b, Physica C **256**, 13-32.

Herzog, R., P. Berghuis, G.A. Wagner, J.E. Evetts and G. Wirth, 1995, Applied Superconductivity, Edinburgh, 3-6 July 1995, Institute of Physics.

Herzog, R. and J.E. Evetts, 1994, Review of Scientific Instruments **65**, 3574.

Herzog, R., J.E. Evetts, R.E. Somekh and P.A. Pullan, 1994, 7th IWCC in Superconductors, Alpbach, Tyrol, Austria, World Scientific, Singapore, 1994

Przyslupski, P., R. Herzog, A.J. Pauza, R.E. Somekh and J.E. Evetts, 1993, IEEE Trans. Appl. Supercon. **3**, 1283.